國立台灣大學工學院機械工程研究所

碩士論文

Department of Mechanical Engineering
College of Engineering
National Taiwan University
Master Thesis

具抗逆激磁機構之磁通分流式直流馬達設計與製作

Design and Fabrication of a Flux Shunt DC Motor with an Anti-Demagnetization Mechanism

巫承儒

Cheng-Ju Wu

指導教授：陽毅平 博士

Advisor: Yee-Pien Yang, Ph.D.

中華民國 98 年 7 月

July, 2009


國立臺灣大學
敦品勵學
愛國愛人

致謝

本論文承蒙恩師　陽毅平博士在研究期間殷切指導與鞭策，並於寫作時逐字斧正乃得以順利完成。為學期間，恩師在研究精神上的啟發與為人處事的薰陶，使我獲益匪淺，師恩浩瀚，永銘於心，特於論文卷首致上最真摯的敬意與謝忱。同時也感謝口試委員　王順源教授與　楊勝明教授，對於本論文提出的建議與指正，使得本論文更加完善。

感謝巨獅創意科技公司對於本研究計畫的支持，讓我有充分的資源完成本研究。特別感謝楊泰和經理對於馬達設計理念之獨到見解與看法的分享，以及胡樹明與吳承章工程師在馬達製造上的大力協助，使得本文更臻圓滿。

感謝實驗室學長勳豪、嘉鴻、富偉、佳隆、茂恩、玉銘、政杭、建章，在我碩一期間與我討論研究上的問題，並提供許多解決問題的方法，使我能夠迅速的適應這個環境。也感謝同學星鋒、豐州、戴正、烜睿、凱翔、瑞明，在這兩年中愉快的相處，彼此之間共同歡笑、共同努力，以及互相扶持的日子，是我生命中珍貴的一部分。另外感謝學弟奕元、忠翰、珺田、澤超、奕睿、大豪、彥銘、信志的幫助，替我分擔研究工作，加快我的研究進度。

最後，謹以此文獻給我親愛的父母與家人，感謝父母的培育之恩，以及家人多年來的支持、照顧與鼓勵，你們的支持與陪伴給予我無後顧之憂的環境，使我得以全心全意的完成研究與學業。

Acknowledgements

I would like to express my greatest gratitude to my advisor, Dr. Yee-Pien Yang, for his stimulating discussions and invaluable guidance. Without his influence, this thesis could never have been accomplished. I thank Dr. Shun-Yuan Wang and Dr. Sheng-Ming Yang, the committee members of the oral exam, I am very grateful for their guidance and assistance.

I thank GIANT LION KNOW-HOW Corporation for sponsoring enough financial funding and affording me an opportunity in this research. My special thanks to Tai-Her Yang, director of C&I department, for insightful discussion of electric machine. I would also like to thank Mr. Shu-Ming Hu and Mr. Cheng-Chang Wu, engineers of C&I department, for their enthusiasm about fabricating the prototype machine.

I am grateful to my seniors of laboratory, Hsun-Hao, Jia-Hong, Fu-Wei, Chia-Lung, Mao-En, Yu-Ming, Cheng-Hang, and Jian-Jhang, who taught me a lot in my first grade. Many thanks also go to my classmates, Hsing-Feng, Feng-Chou, Dai-Cheng, Syuan-Ruei, Kai- Siang, and Ruei-Ming, who accompanied me to spend two years time with laughing and striving. Besides, I am indebted to my juniors, Yi-Yuan, Jhong-Han, Jyun-Tian, Ze-Chao, Yi-Ruei, Da-Hao, and Sin-Jhih. Without your help, the completion of the research would not be so successful.

Finally, I would like to express my gratitude toward my sincere families, for their support, understanding and encouragement. Your tender solicitude equips me with power and confidence to face all the difficulties. This work is dedicated to you all.

具抗逆激磁機構之磁通分流式直流馬達設計與製作

巫承儒[1]　　陽毅平[2]

國立台灣大學機械工程研究所

中文摘要

高性能永磁式電機使用具有強大磁能積的稀土元素釹鐵硼永久磁鐵，可以提供強大的磁場，用來取代電流激磁，達成省電效益。然而，永久磁鐵所提供的磁場無法調控，而且成本高昂，若折衷採用次階永久磁鐵，則於受到逆激磁可能產生不可逆的退磁，導致馬達輸出效能變差。為解決上述問題，本研究採用次階永久磁鐵與線圈激磁之混合磁動勢，做為可控磁場，並且結合磁通分流之概念，設計出創新的電機結構，稱為具抗逆激磁機構之磁通分流式直流馬達，能克服傳統永磁電機性能上的先天限制。研究中提出一套完整的馬達設計流程，首先由磁路觀點與馬達設計方程式建立本馬達的二維磁路模型，結合多目標函數最佳化設計軟體，同時對馬達輸出力矩、轉速、效率以及重量進行最佳化設計，並且經由有限元素分析軟體加以驗證，最後製作出馬達原型，並實測出馬達性能。根據馬達測試結果顯示，增加線圈激磁電流能使馬達在定電樞電壓下的效率與力矩提高，且控制線圈激磁電流能改變馬達定電樞電壓下的轉速，此優異電機特性可應用於無段變速伺服驅動系統。

---

[1] 研究生

[2] 指導教授

Design and Fabrication of a Flux Shunt DC Motor with an Anti-Demagnetization Mechanism

Cheng-Ju Wu[1]　　Yee-Pien Yang[2]
Department of Mechanical Engineering
National Taiwan University, Taipei, Taiwan, ROC

Abstract

High energy product rare earth magnets are widely used in high performance permanent magnet machines to replace the current excitation methods and to improve machine efficiency. However, the magnetic field provided by a permanent magnet cannot be adjusted and the price of rare earth magnets is high. If the machine adopts low grade permanent magnet, there is a high risk of irreversible demagnetization. To address this problem, a novel DC commutator machine that incorporates the concepts of hybrid magnetomotive force and flux shunt is proposed in this research. The hybrid magnetomotive force is provided by a low grade permanent magnet and an additional field winding to form an adjustable magnetic field, which is connected in the flux shunt magnetic circuit. The design procedures of this machine are presented in the following order: magnetic circuit model construction, optimization, and finite element analysis verification. Finally, a conceptual prototype is fabricated. The experimental results show that increases in the field winding current can increase the machine efficiency and torque, while the armature voltage is kept constant. Moreover, the machine speed can also be changed by controlling the field winding current at constant armature voltage. This excellent machine characteristic could be applied to a continuous speed variation servo drive system.

---

[1] Graduate Student

[2] Advisor

Contents

List of Figures

List of Tables

List of Symbols

Symbol	Explanation	Unit
A	Cross-sectional area	m^2
A_a	Armature conductor area	m^2
A_c	Cross-sectional area of core	m^2
A_g	Cross-sectional area of air gap	m^2
A_m	Cross-sectional area of magnet	m^2
A_s	Stator conductor area	m^2
A_w	Cross-sectional area of wire	m^2
B	Magnetic flux density	T
B_c	Magnetic flux density of cores	T
B_g	Magnetic flux density of air gap	T
B_m	Magnetic flux density of magnet	T
B_r	Remanence flux density	T
C_b	Bearing coefficient	
C_f	Windage friction coefficient	
d_1	Tooth shoe depth	m
d_2	Conductor slot depth	m
d_3	Armature tooth depth	m
d_a	Armature back iron width	m
d_s	Stator back iron width	m

d_{wa}	Armature winding diameter	m
d_{ws}	Stator winding diameter	m
D	Density of material	kg/m^3
D_a	Armature diameter	m
D_b	Bearing diameter	m
E	Induced voltage	V
E_b	Back-EMF	V
E_t	Transformer voltage	V
f	Frequency	Hz
F	Magnetomotive force	A-turns
F_m	Magnetomotive force of magnet	A-turns
g	Air gap length	m
g_{eff}	Effective air gap length	m
g_s	Air gap length on the stator side	m
h	Silicon steel thickness	m
h_c	Average convection heat transfer coefficient	W/m^{2}K
H	Magnetic field intensity	A-turns/m
H_c	Coercive force	A-turns/m
H_g	Magnetic field intensity in the air gap	A-turns/m
H_m	Magnetic field intensity of magnet	A-turns/m
H_r	Magnetic field intensity in the core	A-turns/m
i	Current	A

i_a	Armature winding current	A
i_c	Coil current	A
i_f	Field winding current	A
i_{net}	Net current	A
I_{rms}	RMS phase current	A
k_e	Constant of eddy current loss	
k_h	Constant of hysteresis loss	
l	Motor axial length	m
l_a	Average length of the core	m
l_b	Front permeable material length	m
l_m	Magnet length	m
l_w	Coil length	m
L	Inductance	H
L_{aa}	Armature winding self inductance	H
$\overline{L}_{aa}$	Average armature winding self inductance	H
L_{af}	Mutual inductance of armature winding and field winding	H
$\overline{L}_{af}$	Average mutual inductance of armature winding and field winding	H
L_{ff}	Field winding self inductance	H
$\overline{L}_{ff}$	Average fField winding self inductance	H
N	Number of coil turns	turns

N_a	Number of turns per armature slot	turns
N_f	Number of turns per stator slot	turns
N_p	Number of poles	
N_s	Number of slots	
o	Slot opening width	m
o'	Effective armature slot opening width	m
P_{b1}	Front permeable material permeance	A-turns/Wb
P_{b2}	Lateral permeable material permeance	A-turns/Wb
P_c	Permeance of core	A-turns/Wb
P_{copper}	Copper loss	W
P_e	Eddy current loss	W
P_{eq}	Equivalent permeance	A-turns/Wb
P_{fw}	Field winding excitation loss	W
P_g	Permeance of air gap	A-turns/Wb
P_h	Hysteresis loss	W
P_{in}	Input power	W
P_m	Permeance of magnet	A-turns/Wb
P_{in}	Input electrical power	W
P_{iron}	Iron loss	W
P_{mm}	Leakage permeance between magnet	A-turns/Wb
P_{mech}	Mechanical loss	W

P_{PM}	Magnet loss	W
P_{shaft}	Output apparent motor shaft power	W
$P_{winding,DC}$	DC resistance loss	W
$P_{winding,eddy}$	Eddy current loss	W
$P_{windage}$	Windage loss	W
r_a	Armature winding resistance	Ω
r_f	Field winding resistance	Ω
R	Electric resistance	Ω
R_a	Armature outer radius	m
R_{b1}	Front permeable material reluctance	Wb/A-turns
R_{b2}	Lateral permeable material reluctance	Wb/A-turns
R_c	Coil resistance	Ω
R_{DC}	DC resistance	Ω
R_s	Stator inner radius	m
R_{eff}	Effective reluctance	Wb/A-turns
R_e	Core reluctance	Wb/A-turns
R_g	Air gap reluctance	Wb/A-turns
R_m	Magnet reluctance	Wb/A-turns
R_{mm}	Leakage reluctance of magnet	Wb/A-turns
R_r	Back iron reluctance	Wb/A-turns
R_{ro}	Rotor outer radius	m

R_s	Stator reluctance	Wb/A-turns
R_{si}	Stator inner radius	m
s	Rotor shift	rad
t_m	Magnet thickness	m
T	Motor output torque	N-m
T_c	Coil temperature	$°C$
v_a	Armature winding voltage	V
v_f	Field winding voltage	V
V	Voltage	V
V_i	Volume	m^3
w_{b1}	Front permeable material width	m
w_{b2}	Lateral permeable material width	m
w_{aa}	Half of the armature slot width	m
w_{ss}	Half of the stator slot width	m
w_t	Tooth top width	m
w_{tb}	Tooth bottom width	m
W_c	Coenergy	J
W_m	Motor weight	kg
α	Induced phase angle of Back-EMF	degree
δ	Total air gap length	m
θ	Angular position	degree
λ	Flux linkage	Wb-turns

λ_m	Magnet flux linkage	Wb-turns
μ	Permeability of magnetic flux media	H/m
μ_0	Permeability coefficient of air gap ($4\pi\times10^{-7}$)	H/m
μ_c	Permeability of the core material	H/m
μ_r	Relative permeability	
μ_R	Relative recoil permeability	
π	Circumference ratio	
ρ	Resistivity	Ω-m
ρ_a	Air mass density	kg/m^3
ρ_{cu}	Copper resistivity	Ω-m
ρ_i	Density	kg/m^3
σ	Conductivity	1/Ω-m
τ_m	Magnet width	m
τ_p	Pole pitch	
τ_s	Slot pitch	
ϕ	Magnetic flux	Wb
ϕ_f	Field flux	Wb
ϕ_g	Air gap magnetic flux	Wb
ϕ_r	Remanence flux	Wb
ϕ_s	Flux distributions of each slot	Wb
γ	Constant power speed ratio	
η	Efficiency	

η_{dyno}	Dynamometer efficiency	
ω_b	Base speed	rad/s
ω_e	Electrical rotational speed	rad/s
ω_{eddy}	Eddy current angular frequency	rad/s
ω_m	Mechanical angular speed	rad/s

Chapter 1

Introduction

1.1 Background

With the development of advanced permanent magnet materials, traditional electric machines with wound field windings can now be fitted instead with permanent magnets. During the process of electrical and mechanical energy transformation, the traditional wound field winding is excited by currents to provide a constant magnetic flux density. The main disadvantage of an excited field current is the increased copper losses by the machine, which prevents the machine from achieving high efficiency. In contrast, permanent magnet materials are light, easy to shape, high energy products with high remanence. Therefore, these can be used in electric machines to provide a constant magnetic flux density without extra current excitation. In the design aspect of electric machines, permanent magnet electric machines are characterized by high efficiency, high torque density, and high power density.

One significant advance in commercial permanent magnet materials for practical applications has been the development of rare earth permanent magnets. Rare earth permanent magnets are of two basic classes of materials: samarium-cobalt (SmCo) or neodymium-iron-boron (NdFeB). The grade of rare earth permanent magnets is usually evaluated by the maximum energy product. The energy product range among different commercial permanent magnets is illustrated in Fig. 1.1. As indicated, NdFeB magnets have the highest energy product compared to what ferrites can achieve.

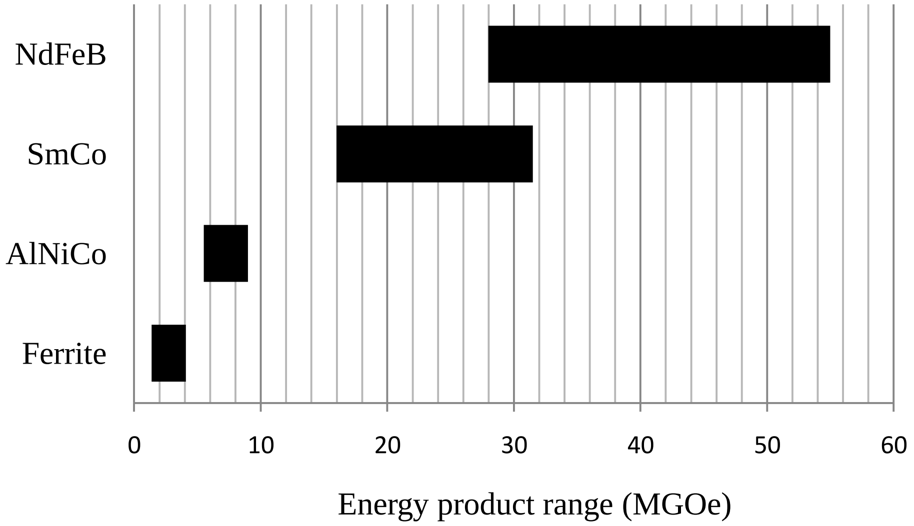

Fig. 1.1 Energy product range among different commercial permanent magnets

However, the utilization of permanent magnet materials in electric machines has its limitation and drawbacks.

The first problem is irreversible demagnetization. Rare earth permanent magnets are very sensitive to temperature. If the operation temperature exceeds the Curie temperature, a partial or total demagnetization will occur, which may reduce the machine performance or damage the machine. For example, NdFeB magnets may not have the best performance in some operating conditions due to its lower Curie temperature, which causes thermal irreversible demagnetization, and due to its reactivity, which leads to corrosion problems. Moreover, if a rare earth permanent magnet is operated in a high frequency magnetic field, this too will cause a considerable loss of magnetism in the magnet.

Second, the flux provided by the permanent magnet is fixed. Although the field excitation of a permanent magnet machine is provided by permanent magnets, and traditional commutator units or slip rings can be eliminated, the field excitation flux cannot vary with the operating condition. Because the induced voltage is proportional to the speed of the machine and the field flux, a base speed of the machine is reached when the induced voltage is equal to the maximum drive voltage. The base speed is also referred to as the rated speed. In order to extend the base speed, the flux provided by field excitation must be decreased while the drive voltage is kept constant at its maximum value. This technique of extending the base speed is called flux-weakening control, which is often employed in permanent magnet synchronous machines. Compared to separately excited DC motors, more complex algorithms are required to realize the flux-weakening technique. In short, the fixed field excitation limits the operational range of the machine.

The third problem involves the production of permanent magnets. Rare-earth elements are not easily obtained, as 80% of the rare-earth elements are found in China. In other words, China dominates the resources of rare-earth elements. Neodymium, one type of rare-earth element, is the main component of the NdFeB magnet. The stores of Neodymium are limited; therefore, it is a fact that the existing Neodymium element will be used up in the future.

In conclusion, the disadvantages of permanent magnets need to be addressed. A novel design of a permanent magnet machine, called the flux shunt DC motor with an anti-demagnetization mechanism, is proposed in the study.

1.2 Literature Review

Permanent magnet machine technology keeps improving due to progress in the permanent magnets themselves, in the power of electronic devices, and in motor control technology. Much literature now exists on research involving permanent magnet machines. The following literature review focuses on the topology of permanent magnet machines and on the study of the demagnetization phenomenon of permanent magnets.

1.2.1 Topology of Permanent Magnetic Machine

The application of permanent magnets in electric machines has gradually become a trend due to the advances in rare-earth material technology. The topology of electric machines using permanent magnets is reviewed in this section.

DC motors

Direct current (DC) motors are composed of an armature, a commutator, brushes, and field poles. The armature is equipped with a commutator that changes the direct current provided by the external power source into alternating current, through the interaction between the commutator and brushes. The field poles are used to provide magnetic flux and can be classified into wound type and permanent magnet type, which are shown in Fig. 1.2.

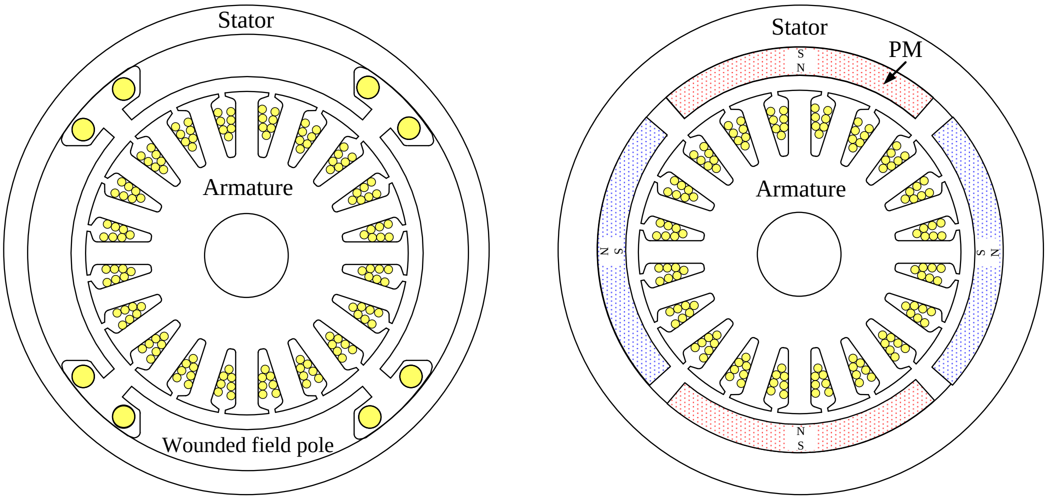

(a) (b)

Fig. 1.2 The field pole configuration of (a) wound type and (b) permanent magnet type

According to the connection configuration of the armature winding and field pole winding, the DC motors with wound field poles can be classified as shunt excitation types, series excitation types, or compound excitation types. Each type of wound field dc motor can be employed in many industrial applications, according to its electrical characteristic. Due to the advances in permanent magnet technology, the wound field poles can now be replaced by permanent magnet field poles to reduce the utilization of copper volume and to decrease the weight of the machine. However, if the machine uses permanent magnets as field poles, the risk of irreversible demagnetization accordingly exists.

Some studies have investigated the design of field poles, taking into consideration this irreversible demagnetization problem in permanent magnet DC motors.

For example, Odor and Mohr [1] presented a design concept for two-component magnets for DC motors that could resist the partial irreversible demagnetization caused by the armature reaction field. As shown in Fig. 1.3, the field poles consisted of two different types of magnet pieces, one is a high quality magnet and the other is a low quality magnet. This research suggested that the flux remained unchanged and that the resistance to demagnetization increased by 30% in the design condition where the motor outer diameter and the armature diameter were held constant.

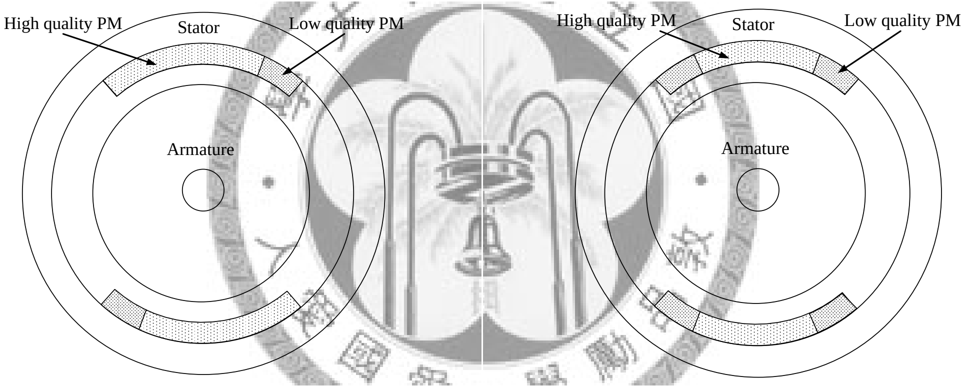

(a) (b)

Fig. 1.3 The configuration of (a) two-component type and (b) modular type of field pole

Isfahani *et al*. [2] proposed a design concept for a modular permanent magnet pole (MPMP) for permanent magnet machines, which shaped the air gap flux density distribution produced by the pole. As shown in Fig. 1.3, the pole is composed of three or more permanent magnet pieces attached together with an alternative magnet quality. Each magnet piece has identical height but the widths can be different. In this study, a linear permanent magnet synchronous motor was chosen as a design example to implement the MPMP design concept. Finite element analysis showed that the total harmonics distortion of back-electromotive force could be reduced by 40%.

Permanent magnet synchronous motor

Due to the advances in power electronic elements, traditional mechanical commutation can now be replaced by electronic commutation, with the advantages of no sparking and easy maintenance. Compared to DC motors, permanent magnet synchronous motors have no commutators or brush units because the commutation processes are realized by the driving circuit, in a process referred to as electronic commutation. Based on the orientation of the magnet flux, permanent magnet synchronous motors can be categorized into radial-flux permanent magnet motors and axial-flux permanent magnet motors.

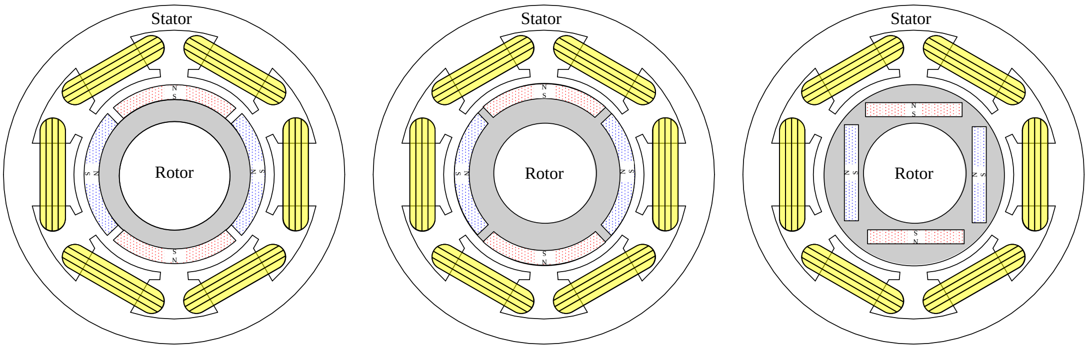

(a) (b) (c)

Fig. 1.4 The constructions of radial-flux permanent magnet motors (a) SPM, (b) inset PM and (c) IPM

According to the arrangement of the permanent magnets, radial-flux permanent magnet motors can be classified into surface-mounted permanent magnet (SPM) motors, inset permanent magnet motors, and interior permanent magnet (IPM) motors. The different constructions of radial-flux permanent magnet motors are shown in Fig. 1.4.

Axial-flux permanent magnet motors can be divided into Torus and Kaman types. If a stator is sandwiched between two rotors, the motor is called the Torus type. On the contrary, if a rotor is sandwiched between two stators, the motor is called the Kaman type [3]. The features of axial-flux permanent magnet motors are that they are smaller in size compared to radial-flux permanent magnet motors and that they have an adjustable air gap. The constructions of axial-flux permanent magnet motors are shown in Fig. 1.5. Because of their unique features and suitable sizes, axial-flux permanent magnet motors have been applied to traction applications in the last decade. A successful example of the usage of axial-flux permanent magnet motors in electric scooters has been developed by Yang [4] [5]. In this research, the axial-flux permanent magnet motor is adopted in direct-driven wheel motors, which do not need mechanical speed reduction mechanisms. Therefore, mechanical transmission losses can be avoided and the efficiency is increased.

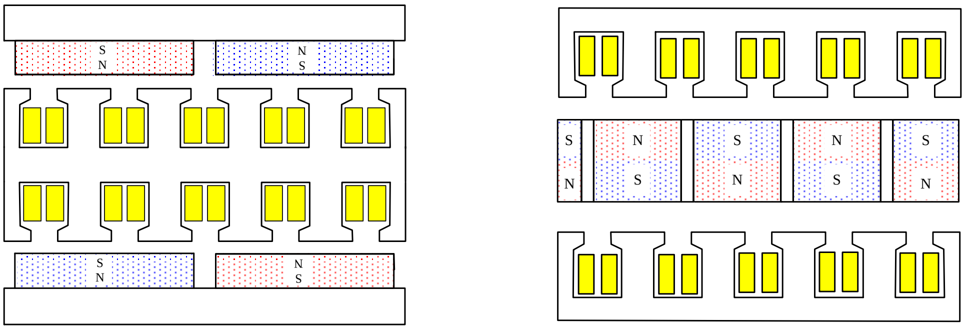

(a) (b)

Fig. 1.5 The constructions of (a) Torus type and (b) Kaman type

Doubly salient permanent magnet motor (DSPM)

Liao *et al*. [6] first introduced the concept of a permanent magnet motor with a doubly salient structure, which is shown in Fig. 1.6. This doubly-salient structure is based on the variable reluctance motor (VRM), and the permanent magnets are arranged in its stator to provide extra field excitation. Therefore, this topology combines features of a reluctance motor and a brushless DC motor. The design result suggested that the performance of doubly salient permanent magnet motor, such as torque density, efficiency, and torque to current ratio, would be superior to variable reluctance and induction motors. The doubly salient structure has recently been the focus of intensive research.

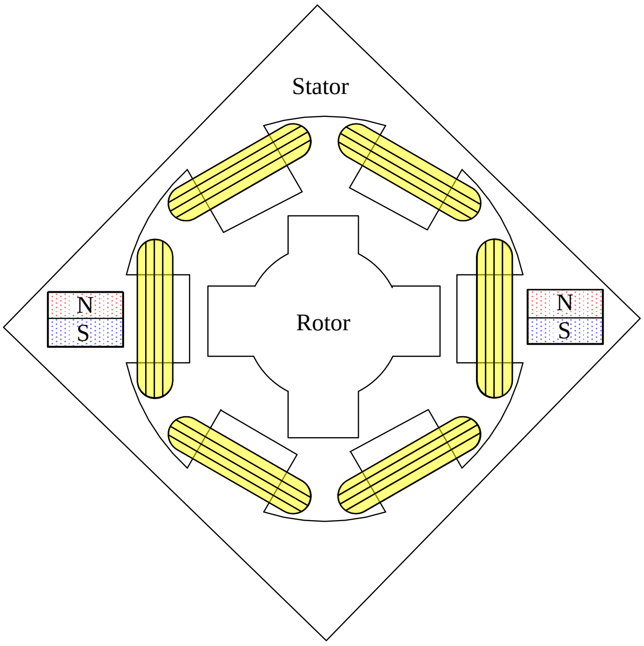

Fig. 1.6 Doubly salient permanent magnet motor (DSPM)

Based on the doubly salient structure, Wei *et al*. [7] presented another topology of a flux-switching permanent magnet (FSPM) motor, which is shown in Fig. 1.7. In Wei's design, radial magnetized permanent magnets are arranged in the stator teeth of the surface-mounted permanent magnet (SPM) motor, to become a flux-switching permanent magnet motor. In this study, finite element analysis showed that the FSPM motor had a higher air gap flux density and a higher torque density than did the surface-mounted permanent magnet motor within the conditions of identical unit copper loss, but it had a higher torque ripple due to cogging torque.

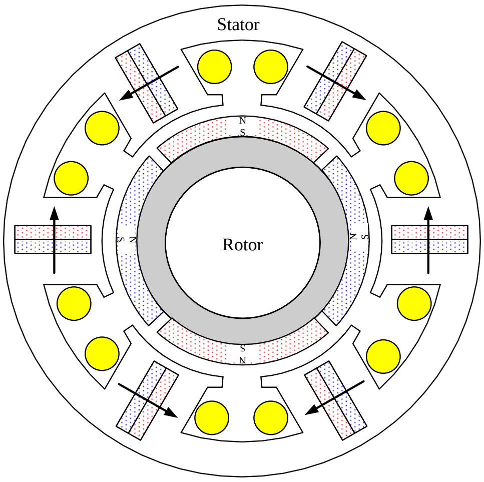

Fig. 1.7 Flux-switching permanent magnet motor

Yu *et al*. [8] incorporated the concept of memory motors [9] into the doubly salient structure and presented a flux-mnemonic permanent magnet brushless motor for electric vehicles, which is shown in Fig. 1.8. In this proposed configuration, the air gap flux density can be controlled by the field windings. Moreover, the field flux weakening capability can be implemented in this topology without a complex control algorithm. A memory motor can be built either as a pole-changing, or as a variable flux machine. In both machine types, the magnetization of permanent magnets can be simply varied by a short current pulse, without any need for the permanent demagnetizing current that is required in internal permanent magnet machines at flux weakening mode. The demagnetizing current flows through the stator windings, supplied from the same source as the stator current. Memory motors combine the advantages of a wound rotor machine (variable rotor flux) with those of a permanent magnet machine (no excitation losses), resulting in a unique machine concept that has the potential to find numerous applications in electric drives.

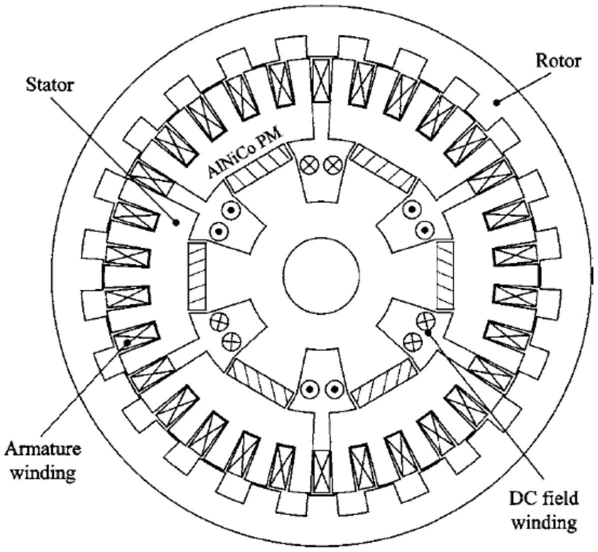

Fig. 1.8 Flux-mnemonic permanent magnet brushless motor

Flux reversal permanent magnet machine

The flux reversal machine is a new brushless doubly salient permanent magnet machine that combines the advantages of the switch reluctance machien and the permanent magnet machine into one machine. Because two magnets of opposite polarity are placed on each stator pole face, it has a bipolar flux and MMF variation with rotor position. Therefore, it has a naturally low inductance and a low electrical time constant. Deodhar *et al.* [10] presented a radial flux reversal permanent magnet machine, which is shown in Fig. 1.9 (a). In this study, the operation principle of this machine is demonstrated. Subsequently, Topor *et al.* [11] presented an axial flux reversal permanent magnet machine, which is shown in Fig. 1.9 (b).

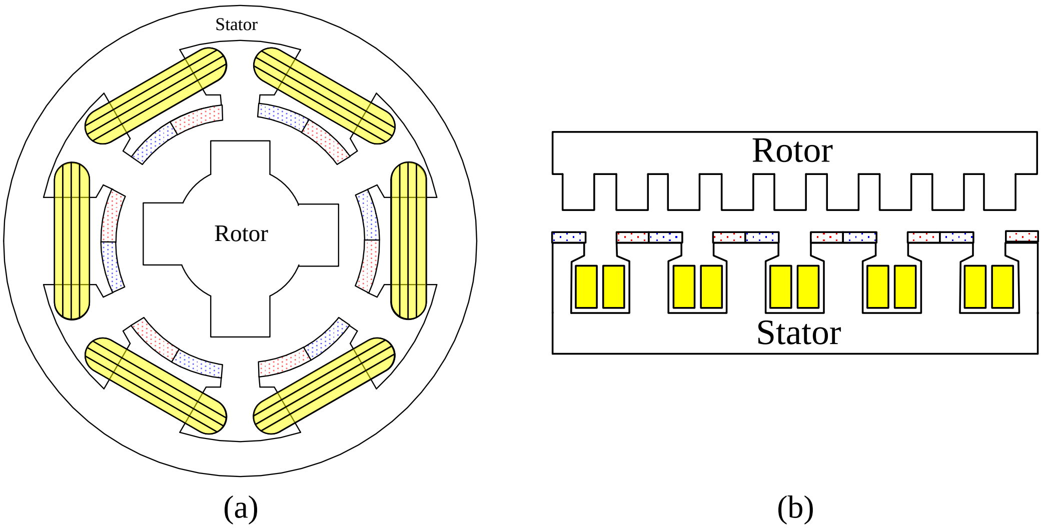

(a) (b)

Fig. 1.9 Flux reversal permanent magnet machine (a) radial type and (b) axial type

Hybrid excited machine

The definition of a hybrid excited machine can be stated as follows: a motor or generator contains both a main excitation source and a secondary field source, which are employed to provide a hybrid magnetic field. In this topology, the common construction of a main excitation source and a secondary field source has the capability to control the field flux. The main excitation source can be a permanent magnet, while the secondary field source is usually an excitation winding or also a permanent magnet. Based on the utilization of field flux control capability, the speed, torque and back electromotive force (EMF) of the machine can be manipulated. Therefore, a hybrid excited machine can be selected as an actuator in conditions that demand high speed variation. Because the characteristic of back electromotive force (EMF) can be controlled by the secondary field source, this machine is suitable for power generation applications.

Several hybrid excited machines topologies are reviewed as follows. Luo and Lipo [12] presented the synchronous/permanent magnet hybrid (SynPM) machine shown in Fig. 1.10. The major part of the air gap flux is provided by the permanent magnets. The excitation poles act as a flux regulator to adjust the air gap flux distribution. This research suggested that this machine had good efficiency, and its field regulation capability was verified.

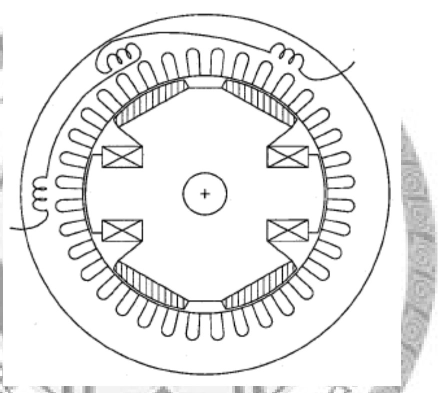

Fig. 1.10 Synchronous/permanent magnet hybrid machine

Fodorean *et al.* [13] introduced a double excited synchronous machine (DESM) prototype that was designed and constructed for an electric vehicle traction system, and is shown in Fig. 1.11. This study suggested that although the speed of machine could be extended by employing the flux-weakening technique, this speed extension was limited by the frequency response of the power converter capability and the increase in iron losses. This problem could be solved by controlling the secondary field source of the hybrid excited machine. Therefore, the speed range can be increased without increasing iron losses and consequently the efficiency can also be increased.

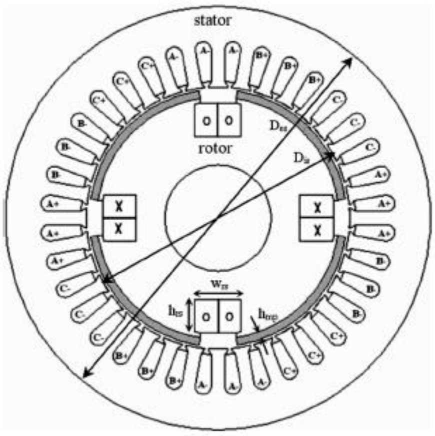

Fig. 1.11 Double excited synchronous machine

Finken and Hameyer [14] presented another rotor structure for a hybrid excited machine, which is depicted in Fig. 1.12. The proposed machine in this paper is based on a hybrid rotor with both permanent magnet and winding excitation. The application of this machine is aimed at automotive power supply systems. Simulation results indicate that winding excitation provides an easier control of the magnetic field by controlling the excitation current, but yields a more complicated rotor construction and increased copper expenses.

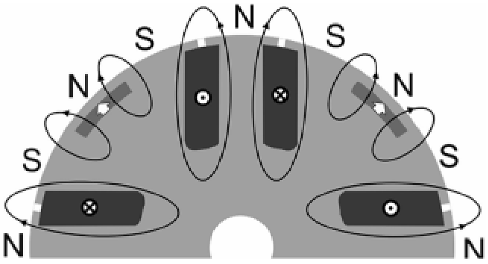

Fig. 1.12 Rotor structure of hybrid excited machine

1.2.2 Studies on the Demagnetization Phenomenon

Due to the advances in rare-earth material studies, the use of permanent magnets has been receiving increased attention in a wide variety of industrial applications. In the motor design field, permanent magnet (PM) machines have gradually become the trend. Permanent magnets can offer high flux density without copper loss and therefore may replace the current excitation field source in electric machines. Moreover, the current-free excitation provided by permanent magnets gives permanent magnet (PM) machines more efficiency and higher power density. Although equipment containing permanent magnets in electric machines has many advantages, the irreversible demagnetization phenomenon occurs in some operating conditions. Irreversible demagnetization will reduce the performance of a permanent magnet machine; therefore, this should be considered in the permanent magnet machine design process.

At present, several studies have been devoted to understanding the demagnetization phenomenon and how to solve it. For instance, Farooq [15] presented a permeance network method to model the demagnetization phenomenon. In this study, an outer rotor permanent magnet machine was selected as a design example and the design result given by the permeance network method was compared to finite element method (FEM) analysis. The author concluded that the permeance network method can solve the electric machine design problem regarding the demagnetization phenomenon much more quickly than would finite element method analysis, but it would also introduce slight computational errors.

Zhilichev [16] presented a method to predict the partial demagnetization behavior of isotropic permanent magnets as the operation temperatures and maximum loads increased in an application. This method was implemented by combining two finite element models, namely, the magnetization model and application model. A DC motor and brushless DC motor were selected as finite element analysis examples, and the analysis result suggested that the model can be used for magnet optimization in the magnetically biased transformer, brush, and brushless motors, when the maximum temperature and current were specified.

Ruoho *et al.* [17] summarized several demagnetization mathematical models, such as the limit model, linear models, the exponent function model, and the hysteresis model. These models are used to predict the performance of a surface magnet synchronous machine, after irreversible demagnetization due to the overloaded condition. After this theoretical study, Ruoho *et al.* [18] conducted an experiment of pulsed field demagnetization. An axially pressed, sintered Nd-Fe-B magnet was selected as the experimental sample magnet and the sample had been demagnetized by an inclined field. The purpose of the experiment was to model the demagnetization behavior of permanent magnets in electrical machines. Based on this experiment, a simple model was presented to consider the angular dependence of demagnetization resistance. The researcher also presented an empirical model for modeling of demagnetization behavior caused by an inclined field. This empirical model was incorporated by finite element method analysis and the result suggested that the inclined demagnetization field must be considered while modeling the demagnetization behavior.

In order to extend the maximum speed range of a motor, the flux weakening control technique is usually adopted. However, flux weakening control is usually achieved by applying a large demagnetizing current in the *d*-axis of the permanent magnets to suppress the magnet flux. Therefore, flux weakening control may bring the risk of irreversible demagnetizing. Xu *et al.* [19] proposed a new design concept of a permanent magnet machine for flux weakening operation. This new design introduced a permeable material, which has an altering flux path, into the magnet circuit of the motor. Finite element analysis was employed to evaluate the design result and it was concluded that flux weakening is achieved without applying an excessive *d*-axis current to reduce the flux of the magnets.

Aydin et al. [20] [21] proposed a new axial flux permanent magnet machine concept with air gap flux control, which is shown in Fig. 1.13. This design has two slotted stator rings realized by tape wound cores with polyphase AC windings, two disc rotors, and a DC field winding. The circumferentially wound DC field winding is placed in between the inner and outer stator rings. There is no need for a stator yoke, since the main flux travels from one rotor to the other. However, there has to be sufficient stator yoke to hold the field winding. The axial thickness of the stator depends on the DC field winding. This novel concept is proposed not only to overcome the drawback associated with current injection but also to improve the features of the conventional permanent magnet machines, by introducing a new axial flux machine concept with flux weakening capability.

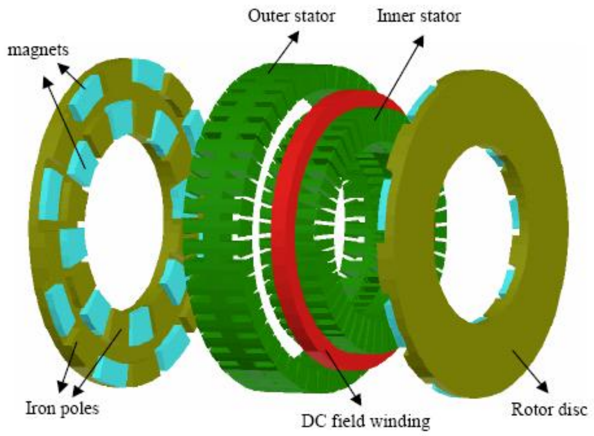

Fig. 1.13 Field controlled axial flux surface magnet PM machine structure

In summary, most permanent magnet machines tend to adopt the surface mounted magnet topology. This topology has some disadvantages such as that the permanent magnet may fall off due to vibration or eccentric forces. Moreover, the permanent magnet directly exposed to the air gap can be easily deteriorated by inverse excitation when the electric machinery is running. The inverse excitation may cause demagnetization risk in a permanent magnet machine, which may deteriorate the performance of the machine.

The permanent magnet DC commutator motor is the most widely used motor, and it also has the problem of demagnetization. However, although much research has focused on the design issues of permanent magnet synchronous machines, there are only few studies on the design of DC commutator machines. Although the research on the demagnetization problem of permanent magnets has gradually received much attention in motor design processes, few innovative electric machine structures have yet been proposed to deal with demagnetization issue. Therefore, a novel structure of DC commutator machine must be proposed to address this problem.

1.3 The Motivation and Objective of the Research

According to the literature just reviewed, the disadvantages of permanent magnet machine topology can be concluded as follows:

1. A demagnetization risk exists in a permanent magnet machine, which may deteriorate the performance of the machine.

2. The constant field flux provided by a permanent magnet machine is difficult to control. This may also constrain the machine performance.

3. The field flux provided by a permanent magnet is generally less than the current excitation, unless a rare-earth permanent magnet is adopted. However, the employment of a rare-earth permanent magnet could bring about cost issues.

The purpose of this study is to propose a novel permanent magnet DC motor with a flux shunt magnetic circuit that would address these problems. Based on the structure of the flux shunt magnetic circuit, the risk of irreversible demagnetization could be reduced and the field flux of the permanent magnet machine could be controlled without complex control techniques. The cost issue resulting from the employment of rare-earth permanent magnets could be also resolved.

1.4 Thesis Organization

The organization of this thesis is illustrated in Fig. 1.14. The thesis is composed of seven chapters. The abstract of each chapter is described as follows.

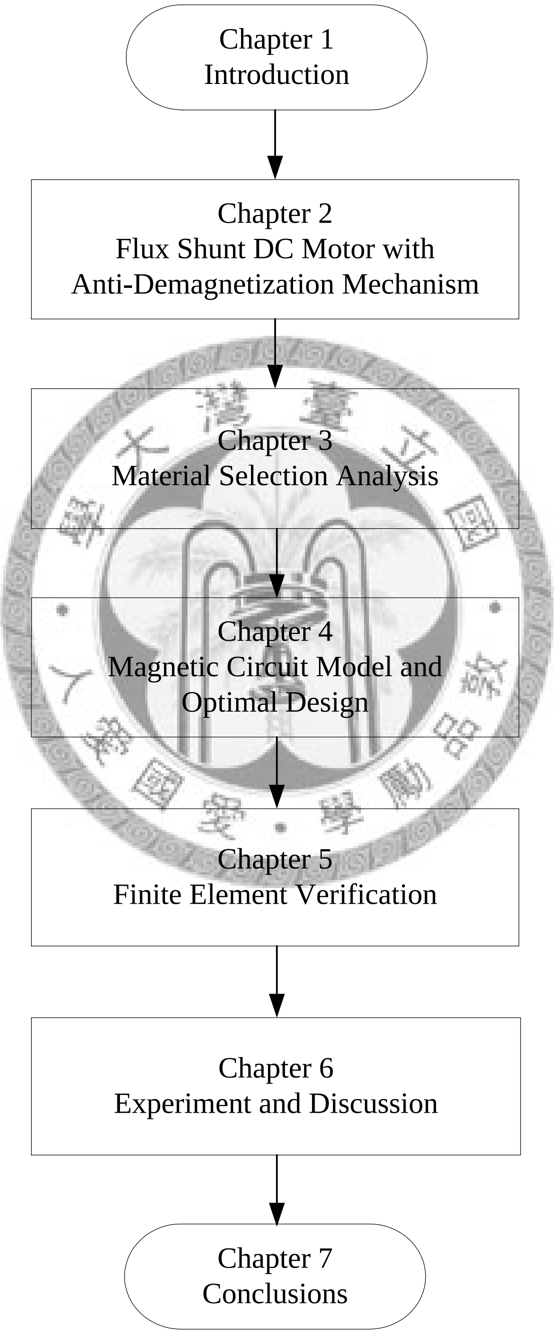

Fig. 1.14 Thesis organization

Chapter 1 presents research background, literature review, and briefly describes the motivation and objectives of this research. The literature review is focused on the topology of permanent magnet machines and the investigation of the demagnetization phenomenon.

Chapter 2 presents a conceptual design of a flux shunt DC motor with an anti-demagnetization mechanism, whose configuration is introduced. The features of this novel design are summarized. Finally, the demagnetization phenomenon in electric machine is discussed.

Chapter 3 presents the material selection analysis for the flux shunt DC motor. The materials used in electric machine design are discussed in this chapter. According to the material characteristics, a designer can select suitable material to satisfy the required specifications.

Chapter 4 presents an equivalent magnetic circuit model of the flux shunt DC motor. Sensitivity analysis is employed to evaluate how the objective functions are influenced by single design variables, while other design variables are kept constant. Based on the sensitivity indices, the design variables that critically affect the objective functions are chosen as the optimal design variables. Therefore, the optimization process can be executed.

Chapter 5 presents the finite element analysis result of the design. ANSOFT

Maxwell 3D and COSMOS Works are employed for electromagnetic and thermal finite element analysis, respectively.

Chapter 6 presents the fabrication of the flux shunt motor. Experimental methods and results are also demonstrated in this chapter. Experiments include the motor performance test, which provides the information regarding current versus torque, speed versus torque, and speed versus efficiency.

Chapter 7 summarizes the performance and specifications of the designed motor. According to the experimental results, future research and development are suggested.

Chapter 2

A Flux Shunt DC Motor with an Anti-Demagnetization Mechanism

2.1 Design Concept of the Flux Shunt DC Motor

Traditional permanent DC motors use magnets to provide field fluxes as an excitation source. The main advantage of permanent DC motors compared to wound field DC motors is that permanent DC motors do not require an external field winding; therefore, copper losses resulting from field winding current excitation can be eliminated. In addition, the lack of field windings also greatly reduces the weight of permanent DC motors.

However, magnet excitation has its disadvantages, which can be summarized as follows:

First, permanent magnets cannot produce high flux density in comparison to externally supplied field circuits. Therefore, a permanent DC motor may have a lower torque in the identical armature current.

Second, the armature current in permanent DC motors produces an armature magnetic field of its own. The armature magneto-motive force is against that from the field pole flux under some positions of the pole faces, reducing the overall field pole flux. This is the so called armature reaction effect. While the armature current becomes very large, the magneto-motive force of the armature may demagnetize the permanent magnets. In some severe conditions, irreversible demagnetization happens and reduces the machine performance. Details of demagnetization phenomenon will be discussed in section 2.4 to section 2.6.

Third, although using high quality permanent magnets, such as rare earth class magnets, can produce large field fluxes, the field flux cannot be adjusted. The machine performance in terms of speed and torque will therefore be limited by the fixed field flux.

In order to control the flux in the field pole and to address the irreversible demagnetization risk, a flux shunt DC motor is proposed. The topology of the novel flux shunt DC motor is shown in Fig. 2.1. Although a related patent has been published that disclose a similar topology [22] [23], this type of motor has not yet been reported in the literature.

The flux shunt DC motor is related to electric machinery where the field poles provide controllable magnetic flux. These are composed of a permanent magnet shielded with a layer of ferromagnetic material, the outsides of which are wound with field windings.

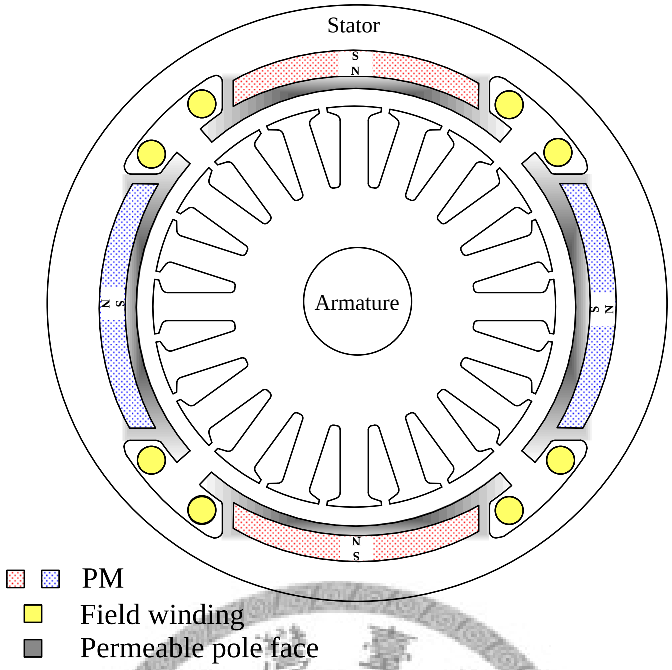

Fig. 2.1 Flux shunt DC motor

The stator pole is made of ferromagnetic material with high permeability, which offers a flux shunt magnetic circuit for field windings and permanent magnet poles. The permanent magnet is peripherally covered by permeable ferromagnetic material, to prevent the permanent magnet from direct exposure to the air gap; therefore, the demagnetization field resulting from armature magneto-motive force can be decreased. Moreover, the permeable pole face can concentrate the flux provided by the permanent magnet and thus avoid flux leakage. The field winding coil is composed of copper wires that are excited to supply additional magnetic flux through the air gap to armature. A flux shunt magnetic circuit is provided by the permeable ferromagnetic material between the permanent magnets and field windings on the field poles.

Therefore, the flux of the field windings and the permanent magnet can be combined in the permeable ferromagnetic material. Because the compound flux in the permeable ferromagnetic material is proportional to the supplied excitation current of the field windings, the flux of the field poles can be controlled by supplying various current from the field windings.

Due to the construction of the flux shunt magnetic circuit, a demagnetization of the flux from the armature does not impact the permanent magnet directly, but passes through the permeable ferromagnetic material to partially shunt the flux and to reduce the risk of demagnetization. A schematic view of the flux shunt principle is illustrated in Fig. 2.2. In the magnetic circuit aspect, the design concept of the permeable pole face is very effective and the magnets are well protected against demagnetization.

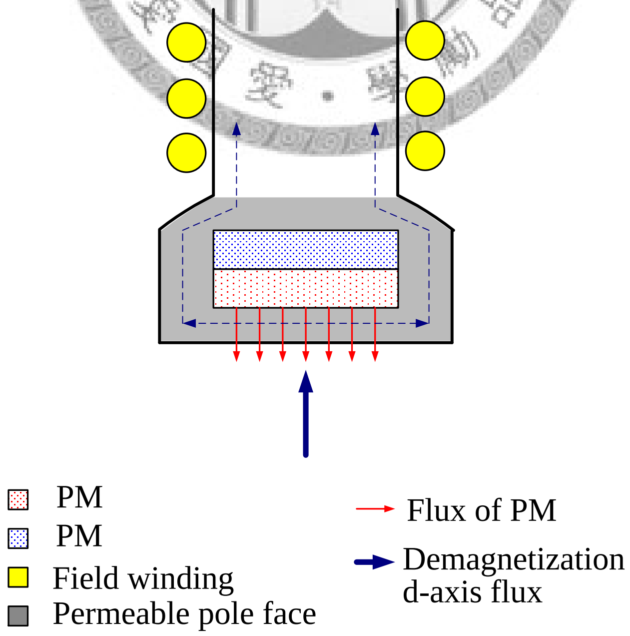

Fig. 2.2 The schematic view of flux shunt principle

Because of the construction of the flux shunt magnetic circuit, the concept of hybrid magneto-motive force is realized in the motor. The hybrid magneto-motive force is composed of the permanent magnet and electromagnet. The electromagnet is excited by the field winding. Because the field windings are excited to increase or decrease the flux from the field poles, the operation mode of the flux shunt DC motor can be divided into accumulative excitation mode or subtractive excitation mode.

In accumulative excitation mode, the polarity of the field winding excitation and the polarity of the permanent magnet are the same, following the property of an accumulative excitation motor. The magnetic flux of the field winding is induced to increase the flux of permanent magnets in accumulative excitation mode. Because of the increased flux in the field pole, the armature reaction effect can be reduced. Moreover, the torque production can be also increased in the identical armature current. The schematic view of a flux shunt DC motor in accumulative excitation mode is shown in Fig. 2.3.

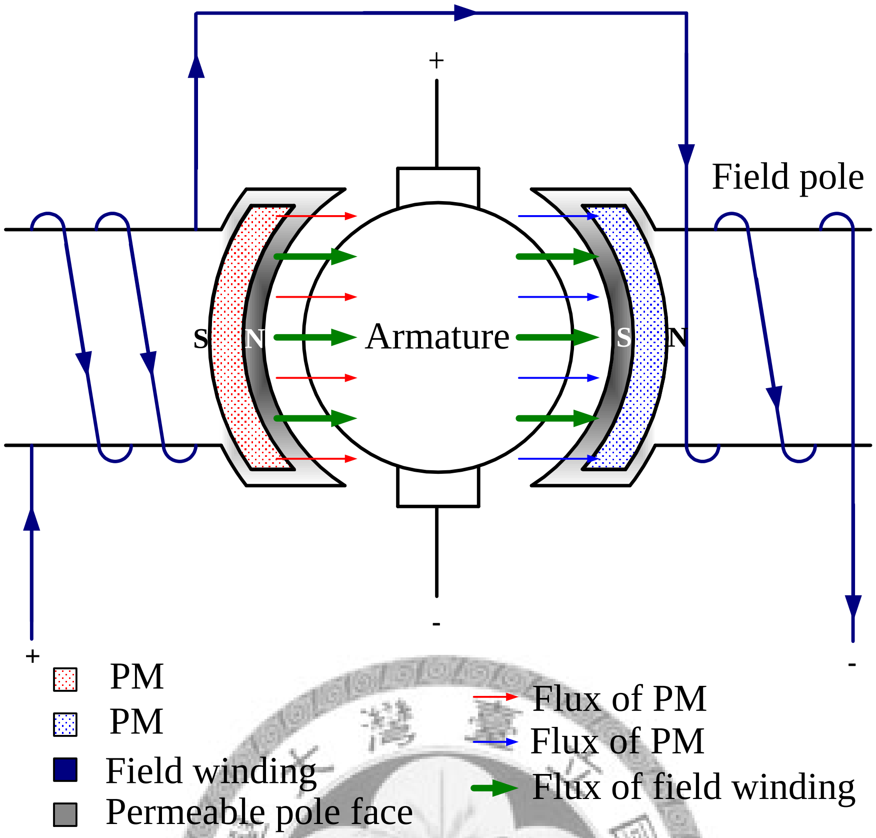

Fig. 2.3 The schematic view of a flux shunt DC motor in accumulative excitation mode

In the subtractive excitation mode, the polarity of the field winding excitation and the polarity of the permanent magnet are different, following the property of a subtractive excitation motor. The magnetic flux of the field winding is induced to weaken the flux of permanent magnets in subtractive excitation mode. Because the flux of permanent magnets is weakened, the machine speed can be extended without increasing the armature voltage. The schematic view of a flux shunt DC motor in the subtractive excitation mode is shown in Fig. 2.4.

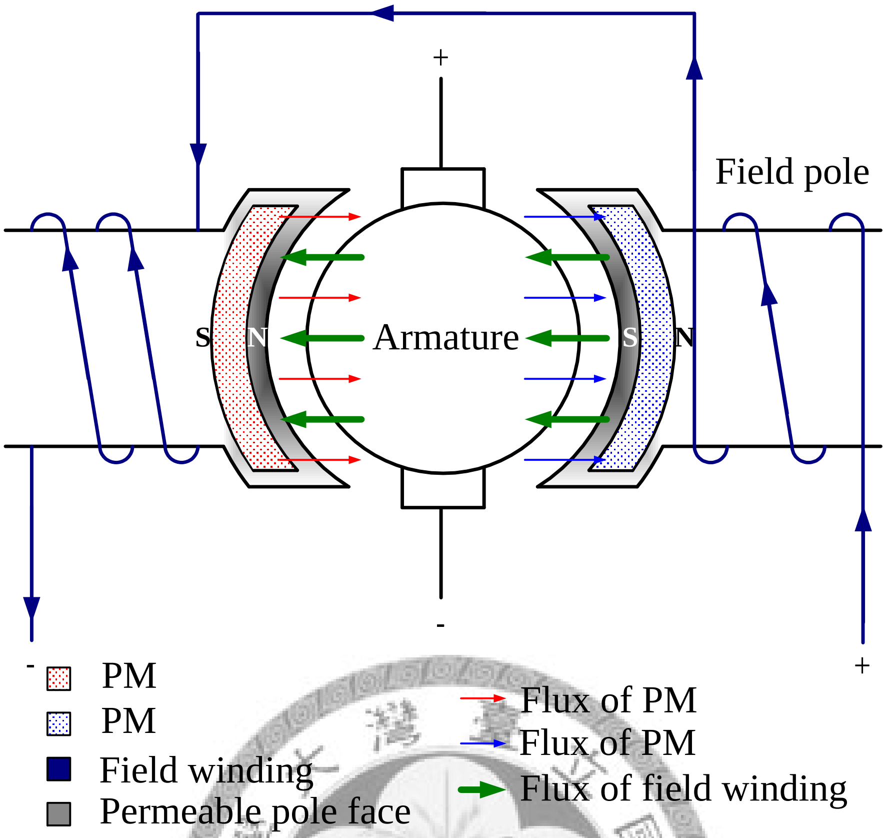

Fig. 2.4 The schematic view of flux shunt DC motor in subtractive excitation mode

In conclusion, the structure of the flux shunt DC motor contains both a main excitation source and a secondary field source, which are employed to provide a hybrid magnetic field in the flux shunt magnetic circuit. The main excitation source is the permanent magnet, while the secondary field source comes from additional field windings. By controlling the polarity of current in the field winding, a wide operating range can be obtained. In the accumulative excitation mode, the field current acts to increase the field flux; therefore, the output torque of the machine will increase and the speed of the machine will slow down without changing the armature current. In subtractive excitation mode, the field current acts to decrease the field flux; therefore, the speed of the machine can be extended without increasing the armature voltage. This characteristic can be applied upon the demand for high speed operation.

2.2 Specifications of a Flux Shunt DC Motor Prototype

Based on the conceptual design of the flux shunt DC motor discussed in section 2.1, the features of the flux shunt DC motor are summarized as follows:

1. Flux shunt magnetic circuit structure
2. Reduced risk of irreversible demagnetization
3. High overload capability
4. Controllable field flux
5. Little armature reaction
6. Small cogging torque
7. Low material cost (with ferrite magnets)

In order to verify that the conceptual design of flux shunt DC motor is realizable, the specifications of the flux shunt DC motor prototype is defined in Table 2.1.

Table 2.1 Specification of flux shunt DC motor

Specification of flux shunt DC motor	
Driving voltage	48V
Max. output power	1000W
Max. speed	3000 rpm
Number of armature slots	20
Number of poles	4
Magnet	Ferrite magnet
Outer diameter	130 mm
Total length	200 mm

2.3 Design Procedure

The conceptual design of a flux shunt DC motor with an anti-demagnetization mechanism is explained in depth in section 2.1. According to this design concept, a design procedure is now proposed from an engineering perspective. The proposed design procedure is illustrated in Fig. 2.5. First of all, the motor specification of the prototype is given. Then, according to the specifications of the prototype, material analysis is made for selecting suitable materials.

Once the main dimensions have been determined, the geometric parameters of field pole and armature can be determined accordingly. Next, the magnetic circuit model of the motor is constructed in terms of design variables, and the sensitivity analysis is employed to evaluate how the objective functions are influenced by single design variable changes, while other design variables are kept constant. Critical design variables can be selected from the results of sensitivity analysis. A proper set of design variables is then determined by maximizing or minimizing the designated objective functions, which are output torque, speed, weight, and efficiency.

Following this, both finite element electromagnetic and thermal analyses are used to verify the results of the analytical design. The former is employed to verify the predetermined motor performance and refine the design variables. The latter is used to evaluate the heat dissipation ability of the motor.

Finally, the manufacturing drawings are prepared for prototyping; while performance tests are also implemented to obtain characteristic curves of the motor.

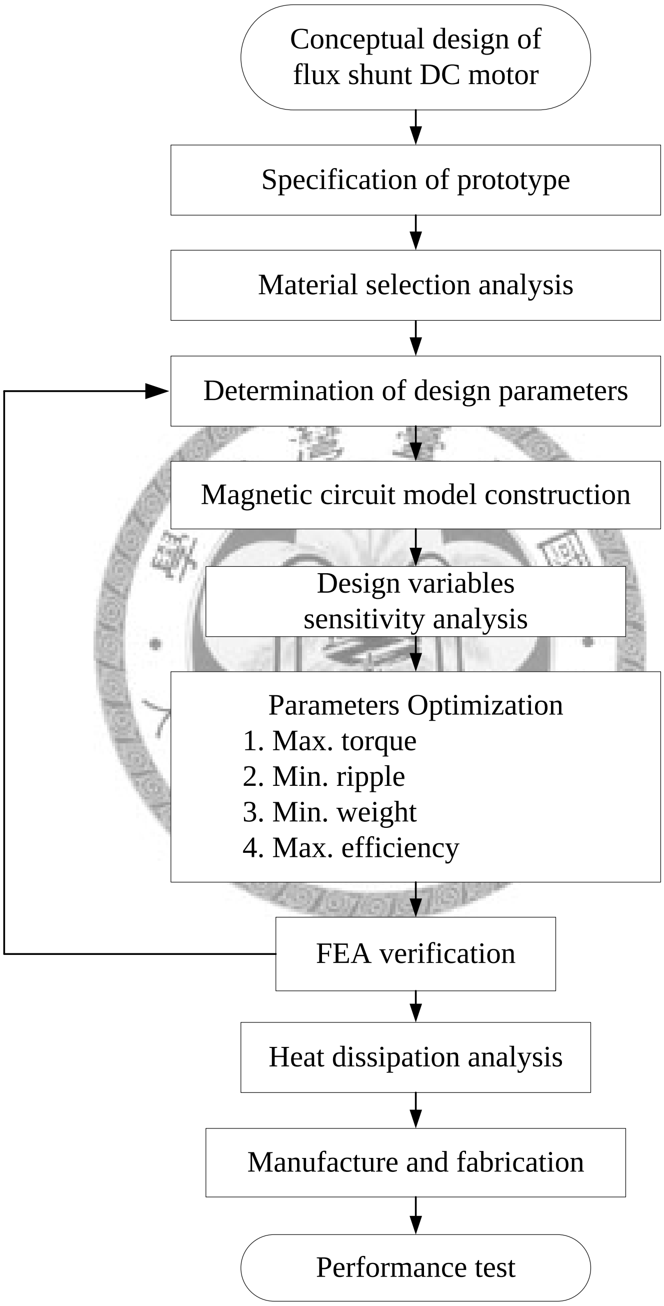

Fig. 2.5 Flowchart of the design procedure for a flux shunt DC motor

2.4 Demagnetization of the Permanent Magnet

Demagnetization of magnets can be classified into reversible and irreversible demagnetization behaviors which are shown in Fig. 2.6 [24]. If this external excitation does not exceed the knee point of *B-H* curve, magnets will operate along the original recoil line. This is called reversible demagnetization. In general, the permanent magnet in an electric machine is designed to operate on the original recoil line, while the stator windings exert a periodic excitation magnetic field. However, if the operation point falls below the knee point of the *B-H* curve in the second or third quadrant, the magnet will be irreversibly demagnetized.

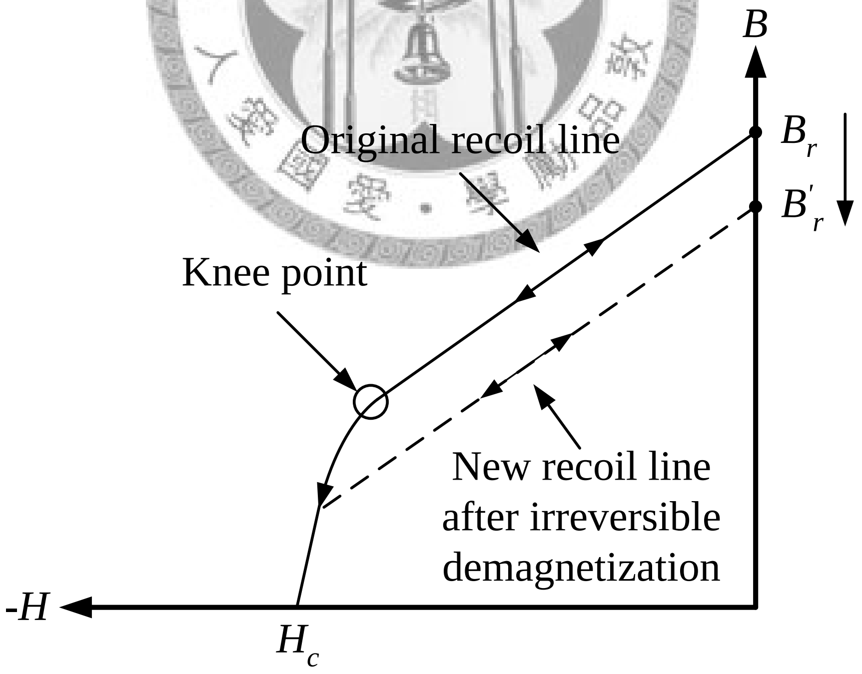

Fig. 2.6 Reversible and irreversible demagnetization behavior

After this irreversible process, the original recoil line will change to a new recoil line and the original remanent flux density B_r will decrease to a lower value B_r'. The demagnetized magnet will not maintain its original behavior even if the excitation magnetic field is removed. The only possible way to remagnetize the demagnetized magnet is for the new recoil line to return to the original one. Irreversible demagnetization not only damages the permanent magnet but it also deteriorates the performance of the machine. Therefore, demagnetization is a critical issue for electric machine design.

2.5 The Causes of Irreversible Demagnetization

The causes of irreversible demagnetization in electric machine can be summarized as follows:

(1) The operating temperature of the permanent magnet material

According to Faraday's law, while a time varying magnetic field is applied on a conductive material, this external field will generate eddy currents which result in a power loss in the material. The generated power loss increases the material temperature. This phenomenon occurs in electric machines. In the design of permanent magnetic machines, permanent magnets must be operated above the knee point of *B-H* curve. The influence of rising temperature in permanent magnets with no-load condition is illustrated in Fig. 2.7. The operation points Q_1, Q_2, Q_3, and Q_4 change while the temperature increases from T_1 to T_4. Operation points Q_1, Q_2, and Q_3 work in the linear region. If the temperature does not exceed T_3, the remanence B_r will recover to its original value B_{r1} while the temperature of the magnet is cooling down to the original temperature T_1. However, operation point Q_4 is below the knee point of the *B-H* curve, which means that the permanent magnet is operating in the nonlinear region and the remanence B_r will never return to its original value B_{r1} even if the temperature is cooled to T_1. This is called irreversible demagnetization.

The rising temperature in permanent magnets has two sources; one is due to the eddy current generated in the rotor, and the other is in the permanent magnet. The stator windings exert a time varying magnetic field on the rotor to induce eddy currents. These eddy currents increase the temperature of the rotor, especially the rotor surface. The permanent magnets arranged on the rotor may then suffer the risk of irreversible demagnetization, if the heat cannot properly be removed by the cooling system.

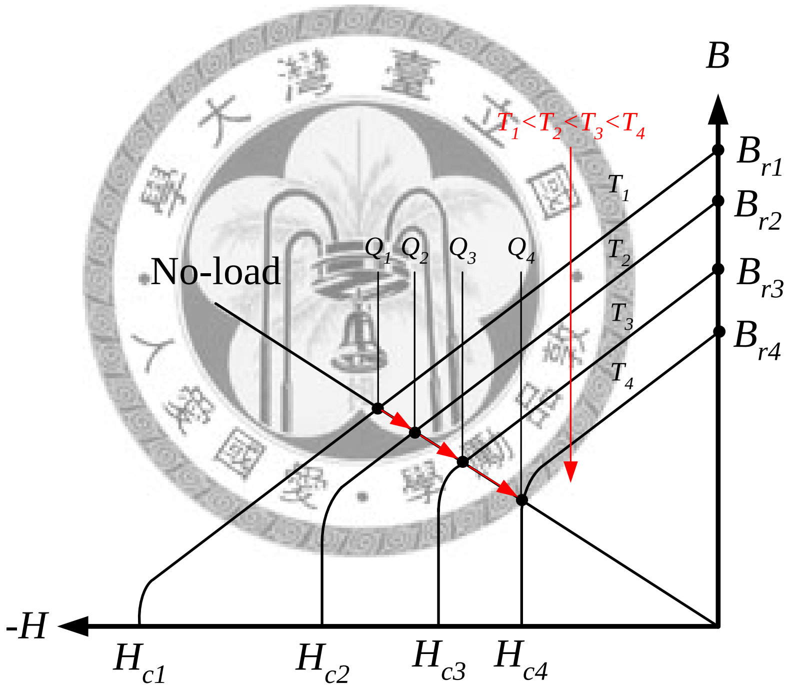

Fig. 2.7 Demagnetization curve of permanent magnets with temperature increase at a constant loading condition

As shown in Fig. 2.8, based on the operating temperature of permanent magnet material, five sintered NdFeB magnets at different grades are selected for comparison of their remanences at different temperatures. The remanence of NdFeB magnets will decrease as the operating temperature increases. In short, machine performance is very sensitive to temperature; therefore, the relation between remanence and temperature must be evaluated while selecting magnets.

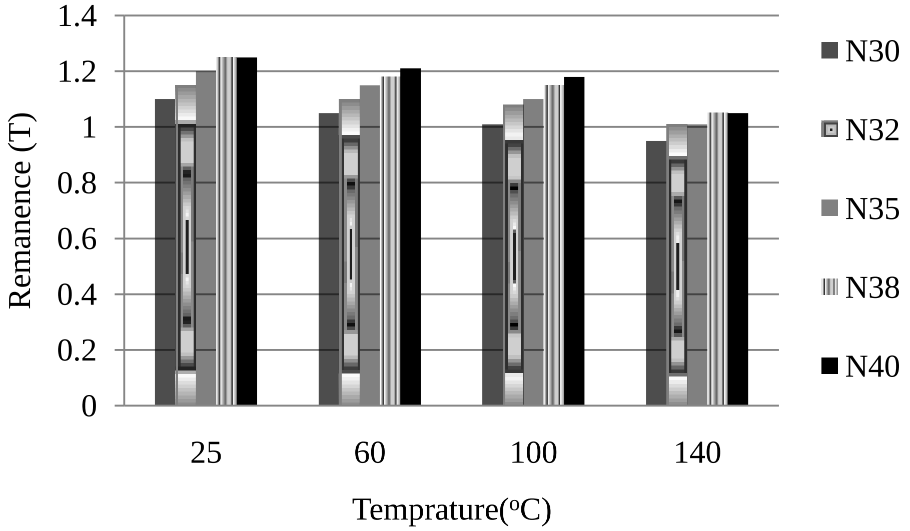

Fig. 2.8 Different grades of NdFeB magnets remanence at different temperature

(2) The loading condition of the machine

According to the load condition of the electric machine, the *B-H* curve can be divided by three load lines designated no-load, rated-load, and over-load, with their corresponding operation points Q_1 ,Q_2 , and Q_3 which are denoted in Fig. 2.9 [19]. In general, the electric machine is designed to operate at a rated-load region. However, the stator winding produces a large magnetic field in some operating conditions, which may lead to irreversible demagnetization if the large magnetic field exceeds the knee point in the *B-H* curve. This phenomenon occurs in the over-load condition and is a result of the instantaneous currents at a starting, locked rotor [25] or the short-circuit current in the stator windings [26].

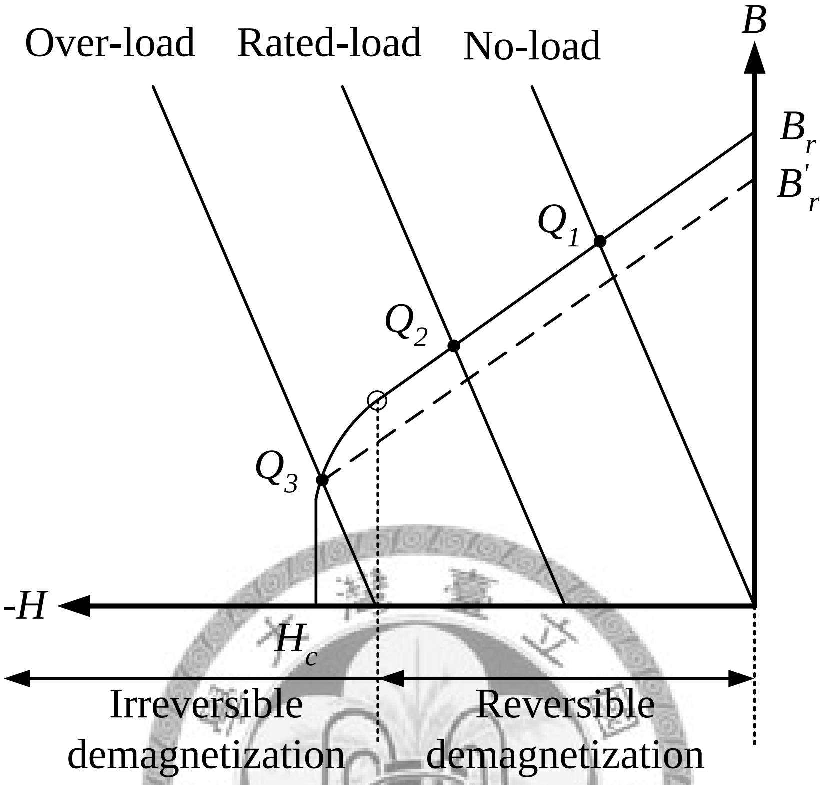

Fig. 2.9 Demagnetization curve of permanent magnets with different load conditions at constant temperature

In a permanent magnet synchronous machine, due to the fixed magnet flux density on the rotor, the flux weakening operation at high speed is implemented by applying a large demagnetization current in the *d*-axis of the magnets (*d*-axis is referred to the direction of magnetic pole). This technique involves the risk of irreversible demagnetization because the applied negative current along the *d*-axis may exceed the limited value. The constrained value of negative *d*-axis current is related to the *B*-*H* curve of the magnet, because this demagnetization current in the stator windings will induce a large magnetic field, causing irreversible demagnetization when the operating point falls below the knee of the magnet’s *B*-*H* curve in the second or third quadrant.

(3) Both of rising temperature and loading condition of the machine

In a real machine operation, the temperature of the machine is related to its load condition. Therefore, irreversible demagnetization could be simultaneously caused by these two modes. The demagnetization curve of permanent magnets with different load condition while temperature is increasing as illustrated in Fig. 2.10. If the heat dissipation system of the machine is well designed, the temperature of magnets rising from T_1 to T_4 will not induce the risk of irreversible demagnetization in the no-load condition. The machine remains in operation for a long time in the rated-load condition. However, if the heat dissipation system of the machine is not well designed, the temperature of the magnets rises from T_1 to T_4 and the risk of irreversible demagnetization increases in rated-load condition. When the driving current is suddenly increased, as the machine is over-loaded from the state of no-load or rated-load condition, the increased current produces considerable heat, which cannot be effectively dissipated by the cooling system of machine. Therefore, the increased temperature induces irreversible demagnetization.

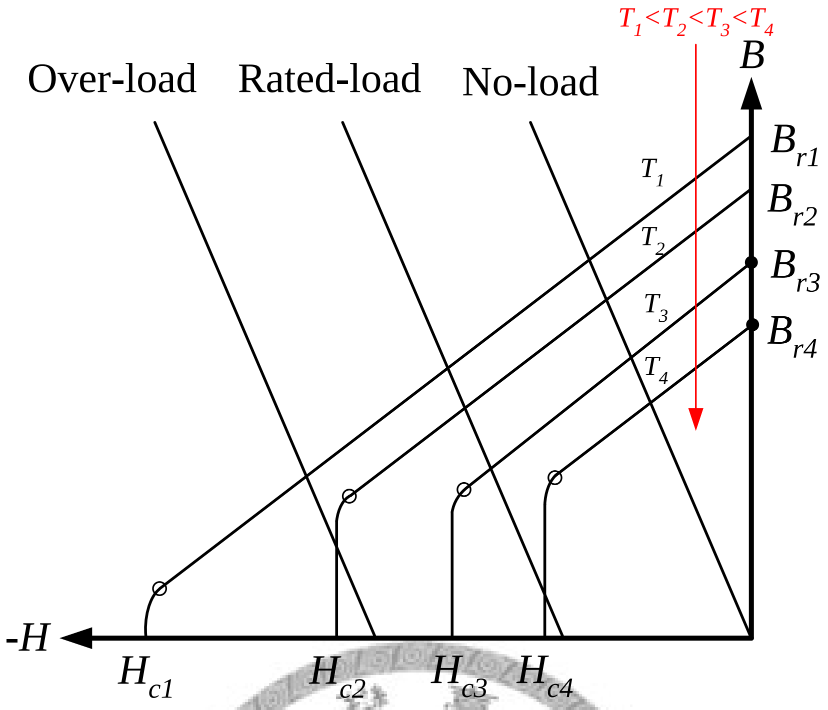

Fig. 2.10 Demagnetization curve of permanent magnets with different load conditions as temperature increases

2.6 The Effects of Irreversible Demagnetization

The remanence of permanent magnets will be decreased after they suffer a large demagnetization field exceeding the knee point. Therefore, the field flux of the machine is also decreased. From an electromechanical energy transformation point of view, the torque is the product of armature current and field flux in the *d*-axis. If the field flux is decreased by irreversible demagnetization, the torque performance decreases accordingly. Therefore, the consumption of armature current will become higher than that rated to maintain the identical load condition [27].

The induced voltage of an electric machine is proportional to the speed and field flux density, which can be inferred from Faraday's law. If the permanent magnet is irreversibly demagnetized, the field flux of the machine is decreased. Therefore, the induced voltage is decreased or distorted, resulting in the distortion or reduction of back-emf and air gap flux density.

From the perspective of electrical machine design, the motor performance will be degenerated because of irreversible demagnetization. The effects of irreversible demagnetization are listed as follows:

1. The reduction of torque ability in the same magnitude of driving current [27].

2. The decrease in motor efficiency.

3. The distortion or reduction of back-emf [26].

4. The decrease in air gap flux density.

Consequently, these harmful influences of irreversible demagnetization should be comprehensively studied in the permanent magnet synchronous motor design, especially if the motor is implemented for highly loaded machines, such as electrical directly driven motors for electric vehicles, machine tools, and aircraft applications.

Chapter 3

Material Selection Analysis

3.1 Brief Review of Magnetic Materials

All magnet materials have magnetization behavior. If a magnet material is placed in an external magnetic field with field intensity H, then the flux density B in the magnet material will vary with the field intensity. This magnetization process can be represented by the relationship between flux density and field intensity (magnetization):

$$B = \mu_0 (H + M) \tag{3.1}$$

and

$$M = \chi_m H \tag{3.2}$$

where χ_m is the magnetic susceptibility, which is a dimensionless quantity, M is the magnetization vector, measured in amperes per meter (A/m), H is magnetic field intensity, also measured in amperes per meter, and B is the magnetic flux density, measured in tesla(T).

Substituting (3.2) into (3.1) yields:

$$B = \mu_0(1+\chi_m)H = \mu_r\mu_0 H = \mu H \tag{3.3}$$

where μ_r is the relative permeability of magnetic material, μ_0 is the permeability of free space ($4\pi\times10^{-1}$ H/m), and μ is the absolute permeability.

In terms of the relative permeability, magnetic materials can be categorized into three groups: diamagnetic, paramagnetic, and ferromagnetic materials. The relationship between relative permeability and magnetic materials is listed in Table 3.1.

Table 3.1 Classification of magnet materials

Classification	Relative permeability	Materials
Diamagnetic materials (μ_r <1)	$1-10^{-5} < \mu_r < 1-10^{-11}$	Cu, Ag, Au, Zn
Paramagnetic materials (μ_r>1)	$1+10^{-8} < \mu_r < 1+4\cdot10^{-4}$	Al, Mg, Ti, W
Ferromagnetic materials (μ_r>>1)	$10^{2} < \mu_r < 5\cdot10^{5}$	Fe, Co, Ni

The characteristics of ferromagnetic materials are usually depicted in *B-H* or *M-H* curves. These hysteresis curves describe the nonlinear relationship between magnet flux density and magnet field intensity (magnetization).

Ferromagnetic materials are predominantly used in electric machines. They can be divided into soft and hard magnetic materials. Soft magnetic materials are excellent conductors of magnetic flux and they have narrow hysteresis loops. Soft magnetic materials are broadly referred to as electrical or silicon steel in electric machine design issues. Hard magnetic materials are used to provide constant magnetic flux and they have wider hysteresis loops. Hard magnetic materials are generally called permanent magnetic materials. The difference between soft and hard magnetic materials can be easily identified from their hysteresis curves, as shown in Fig. 3.1.

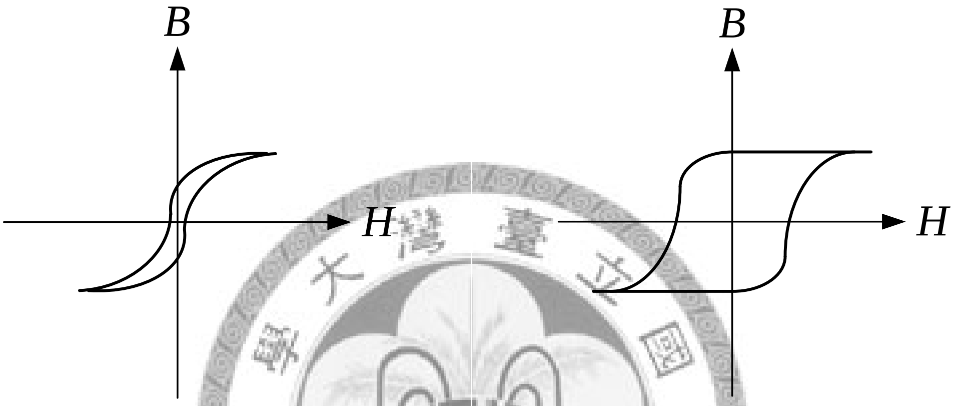

(a) Soft magnetic material (b) Hard magnetic material

Fig. 3.1 Typical hysteresis curves of soft and hard magnetic materials

3.2 Selection of Armature Lamination Steels

Lamination steel is also referred to as silicon steel or electrical steel, and is one of the soft magnetic materials. This material is widely used in electromagnetic power devices, such as transformers and electrical machines. The ideal characteristic of electrical steel should have high inductance at low field magnetic strength and have good conductivity for magnetic flux. In general, since electrical steel is used in alternating magnetic field applications, other requirements for this material are low coercive field strength and a narrow hysteresis loop.

The classification of commercial electrical steel can be divided into non-oriented and grain-oriented. The magnetic characteristic of the non-oriented electrical steel are almost identical in all directions, and is termed isotropic. Hence, non-oriented electrical steel is often used in motors and generators. In contrast, the magnetic characteristic of grain-oriented electrical steel is better in the rolling direction than in the perpendicular direction, due to the orientation effect, which is termed anisotropic. Grain-oriented electrical steel is often used in transformers.

According to the discussion above, the material for laminated armatures is non-oriented electrical steel of a thickness range from 0.12 to 0.64mm. AISI grade M19 of thickness 0.36mm is commonly selected as the armature lamination material.

The *B*-*H* curve of AISI grade M19 is shown in Fig. 3.2.

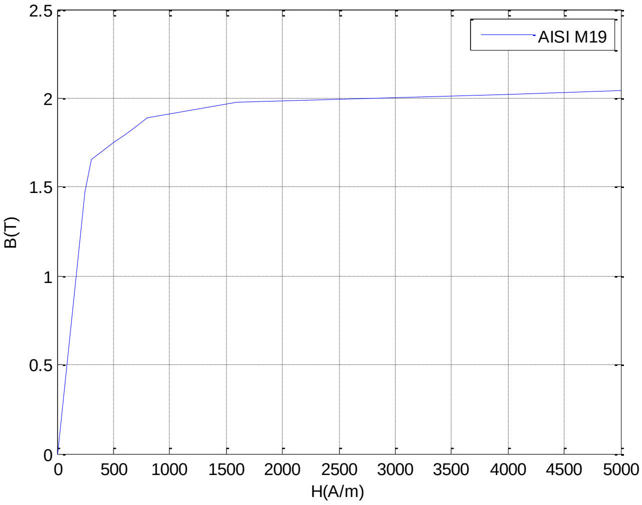

Fig. 3.2 The *B*-*H* curve of AISI grade M19

3.3 Selection of Stator Permeable Pole Face Material

Because a flux shunt magnet circuit loop is composed of a permeable pole face, the stator permeable pole face must be made of permeable material. The selection criterion is good conductivity of magnetic flux; therefore, laminated silicon steel, iron or carbon steel can be adopted. The field winding is wound on the permeable pole face and is excited by direct current to provide the field flux. Because eddy current loss is not induced by direct current, the use of laminated silicon steel may not be necessary. In addition, using laminated silicon steel as a permeable pole face may increase manufacturing difficulty and cost. For these two reasons, low carbon steel grade S15C is normally selected as the permeable pole face material. The *B-H* curve of low carbon steel [28] is shown in Fig. 3.3.

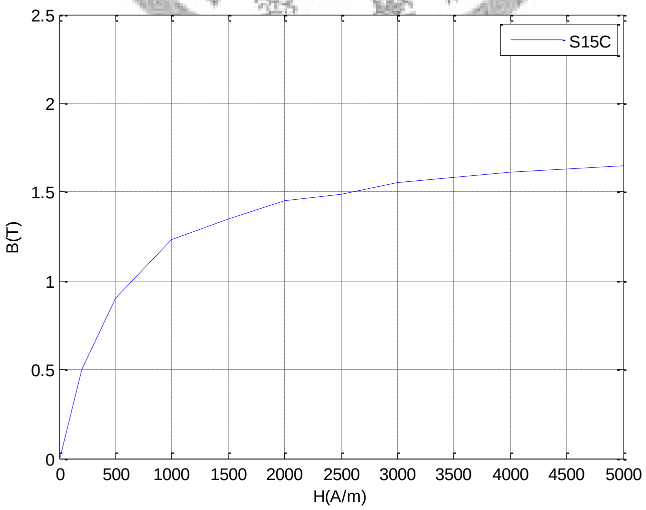

Fig. 3.3 The *B-H* curve of low carbon steel S15C

3.4 Selection of Permanent Magnet Materials

Permanent magnet materials are widely applied in electric machines, because they have highly coercive field strengths, high remanence, and high magnetic permeability. Due to these excellent physical properties, the winding excitation configuration in traditional electric machines has gradually been replaced by permanent magnets. Permanent magnetic materials can be divided into three major classes: alnico, ferrite, and rare-earth magnets, which are the usual candidates for the electric machine applications. The features of several permanent magnetic materials used in electric machine design are introduced as follows:

(1) Alnico magnets

Alnico magnets are composed of alloys of Aluminum, Nickel, and Cobalt. They can be manufactured through either a sintering or a casting process. The features of Alnico magnets are excellent temperature stability and high residual flux density. The physical properties of alnico magnets are listed in Table 3.2.

(2) Ferrite magnets

Ferrite magnets are also referred to as ceramic magnets. These can be manufactured through either a sintering or bonding process. Because of the advantage of cost, ferrite magnets are widely used in commercial electronics. From the mechanical property perspective, ferrite magnets are hard and brittle; therefore, to shape the magnet into a particular form requires special machining techniques. Moreover, ferrite magnets have the risk of irreversible demagnetization at low temperature due to their magnetic properties. Care should be taken to evaluate the working temperature. The physical properties of ferrite magnets are listed in Table 3.2.

(3) Rare-earth magnets

Rare-earth magnets have two major classes, which are Neodymium Iron Boron (NdFeB) and Samarium Cobalt (SmCo) magnets. Because the maximum energy product and remanence of rare-earth magnets are much higher than for other types of magnets, they represent the most advanced permanent magnets today. Compared to ferrite magnets, NdFeB magnets have a better anti-demagnetization ability below 60 $^{\circ}C$, but they are usually expensive. The physical properties of rare-earth permanent magnets are listed in Table 3.3.

Table 3.2 Basic physical properties of ferrite and alnico permanent magnets [29]

Property	Unit	Ferrite		Alnico
		Sintered	Bonded	
B_r	kG	4.3	2.4	8.2
${}_bH_c$	kOe	2.1	2.2	1.65
${}_iH_c$	kOe	2	2.5	1.7
$(BH)_{max}$	MGOe	3.8	1.4	5.3
T_c	^{o}C	450	450	860
$\alpha(B_r)$	%/K	-0.18	-0.03	-0.01
$\beta({}_iH_c)$	%/K	+0.4	-0.2	≈0
R	μΩ•cm	>10^{10}	44000	60
ρ	g/cm^3	5.0	7.0	7.3

Table 3.3 Basic physical properties of rare-earth permanent magnets [29]

Property	Unit	Neodymium Iron Boron		Samarium Cobalt	
		Sintered	Bonded	Sintered	Bonded
B_r	kG	11.6	7.3	9.8	6.3
${}_bH_c$	kOe	10	5.4	8.7	6.8
${}_iH_c$	kOe	12	9	13	11
$(BH)_{max}$	MGOe	32	11	24	10
T_c	^{o}C	310	350	800	720
$\alpha(B_r)$	%/K	-0.03	-0.1	-0.18	-0.11
$\beta({}_iH_c)$	%/K	-0.2	-0.4	+0.4	-0.6
R	μΩ•cm	114	26000	60	150
ρ	g/cm^3	7.3	6	8.3	7.5

The selection of magnetic materials is important in the electric machine design process, because it influences the performance, volume, and cost of the final electric machine. The selection criterion of magnetic materials for electric machine design processes are listed below:

1. The physical properties of the magnetic materials are stable, and they do not sensitively fluctuate with environmental situations, operation temperature, or load condition.
2. The mechanical properties of magnetic materials are sufficiently robust to sustain stress during the operation. Especially for a machine to be operated in critical conditions such as high speed or pressure, the mechanics aspects of the design must be seriously considered.
3. The magnetic materials should be easy to manufacture and assemble.
4. The cost of the magnetic materials should be reasonable for economic reasons.

According to the analysis of permanent magnet material, ferrite magnets are selected to provide main field flux. Because the secondary field flux is provided by current excitation, the total flux is composed by the flux of the permanent magnets and the current excitation flux. The hybrid total flux can satisfy the desired field flux and it is adjustable. Therefore, the utilization of high quality permanent magnets, such as NdFeB magnets, is made unnecessary regardless of their cost.

Chapter 4

The Magnetic Circuit Model and Optimal Design

4.1 The Magnetic Circuit [30]

4.1.1 The Basic Concept of a Magnetic Circuit

A conversion between electrical and mechanical energy occurs in a magnetic field. Generally speaking, a magnetic field can be described by two vector quantities, the magnetic field intensity H (ampere per meter) and the flux density B (tesla). The magnetic field intensity H is related to the net current i_{net} (ampere) flowing through a closed path or contour C, which can be expressed by applying Ampere's law as follows:

$$\oint_C H \cdot dl = i_{net} \tag{4.1}$$

The flux density B can be thought of as the amount of magnetic flux flowing through a given area. The relation between flux density and magnetic field intensity is shown as:

$$B = \mu H \tag{4.2}$$

where μ is the permeability of the magnetic flux medium.

Consider the simple magnetic structure shown in Fig. 4.1, where g is the air gap length, l_a is the average length of the core from one side of the air gap around to the other, ϕ is the magnetic flux excited by the N coil turns and carrying a current of i Ampere.

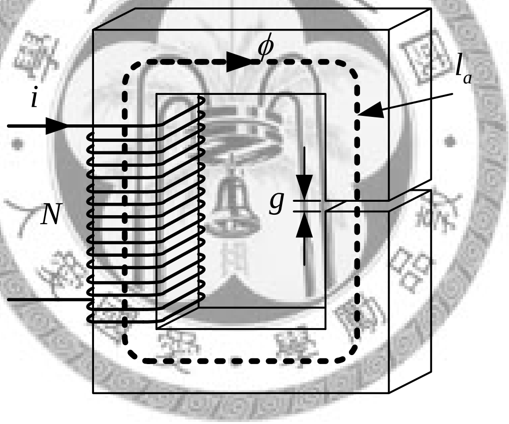

Fig. 4.1 A simple magnetic structure

Assuming that the core material is magnetically permeable, its permeability μ_c is much greater than the permeability μ_0 of the surrounding air. The cross-sectional area of the core in the path of a magnetic flux can be regarded as a constant. Consequently, from equation (4.1), it can be obtained that:

$$Ni = \oint_C H \cdot dl = H_r l_a + H_g g \tag{4.3}$$

where H_r is the field intensity in the core, and H_g is the field intensity in the air gap.

The flux density is defined as the amount of magnetic flux flowing through a given area. Assuming that the cross-sectional areas of the core and air gap are A_c and A_g, respectively, the flux density in the core and air gap can be expressed as:

$$B_c = \frac{\phi}{A_c} \tag{4.4}$$

$$B_g = \frac{\phi}{A_g} \tag{4.5}$$

In addition, the magnetomotive force (MMF) is defined as

$$F = Ni \tag{4.6}$$

From equation (4.3) to (4.6), the following can be obtained:

$$\begin{aligned} F = Ni &= H_r l_a + H_g g \\ &= \frac{B_c}{\mu_c} l_a + \frac{B_g}{\mu_0} g \\ &= \left(\frac{l_a}{\mu_c A_c} + \frac{g}{\mu_0 A_g} \right) \phi \end{aligned} \tag{4.7}$$

where μ_c is the core permeability and μ_0 is the permeability of air ($4\pi \times 10^{-7} H/m$).

By observing equation (4.7), the relationship between magnetomotive force F and magnetic flux ϕ is found to be similar to the relationship between voltage V and current i in an electric circuit, as shown in Fig. 4.2.

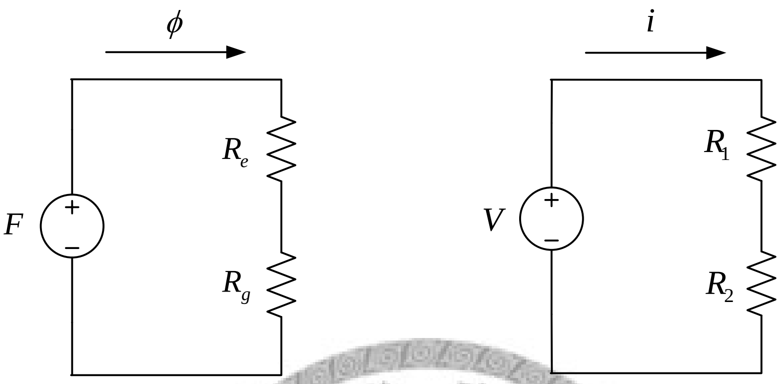

(a) Magnetic (b) Electric

Fig. 4.2 Magnetic circuit model and its analogous electric circuit model

It is well known that the relationship between voltage V and current i in Fig. 4.2 (b) can be represented by Ohm's law, as follows:

$$V = \left(R_1 + R_2\right)i \tag{4.8}$$

where R_1 and R_2 are resistances.

Similarly, the relationship between magnetomotive force F and magnetic flux ϕ in Fig. 4.2 (a) can be described as follows:

$$F = \left(R_e + R_g\right)\phi \tag{4.9}$$

where R_e and R_g are the reluctances of the core and air gap, respectively. Comparing equation (4.7) with (4.9), R_e and R_g can be rewritten as follows:

$$R_e = \frac{l_c}{\mu_c A_c} \tag{4.10}$$

$$R_g = \frac{g}{\mu_0 A_g} \tag{4.11}$$

Although a magnetic circuit is analogous to an electric circuit, their physical meanings are different. For example, the current flowing through a resistance causes energy dissipation, whereas the magnetic flux flowing through reluctance constitutes energy storage.

4.1.2 The PM Magnetic Circuit Model

PMs are made of magnetic materials. In general, the *B*-*H* curve of a PM can be shown as in Fig. 4.3.

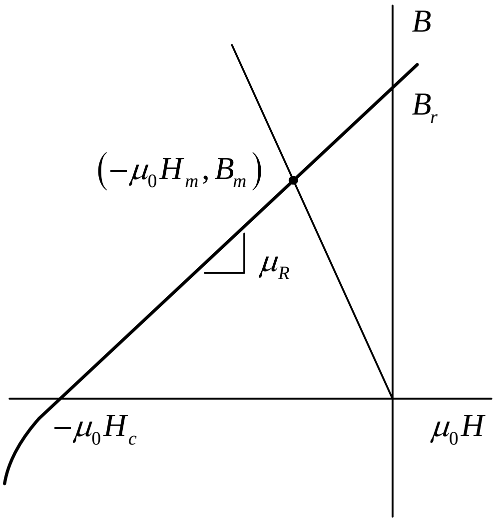

Fig. 4.3 The *B-H* curve of a permanent magnet

For convenience, the field intensity axis is scaled by μ_0, giving both axes dimensions in Tesla (T). In Fig. 4.3, the flux density at the zero field intensity is called the residual flux density B_r, the field intensity at the zero flux density is called the coercive force H_c, and the relative recoil permeability is the slope of the linear part of the *B-H* curve, which is expressed as follows:

$$\mu_R = \frac{B_r}{\mu_0 H_c} \tag{4.12}$$

Point $(-\mu_0 H_m, B_m)$ is the operation point of PMs. It satisfies that:

$$B_r = B_m + \mu_R \mu_0 H_m \tag{4.13}$$

Considering a rectangular magnet of length l_m and cross-sectional area A_m, as shown in Fig. 4.4, the magnetic flux can be derived from the magnetic circuit and represented as follows:

$$\phi_m = \phi_r - \frac{F_m}{R_m} \tag{4.14}$$

Since $\phi_m = B_m A_m$, contrasting equation (4.13) with (4.14), gives the following:

$$\phi_r = B_r A_m \tag{4.15}$$

$$F_m = H_m l_m \tag{4.16}$$

$$R_m = \frac{l_m}{\mu_R \mu_0 A_m} \tag{4.17}$$

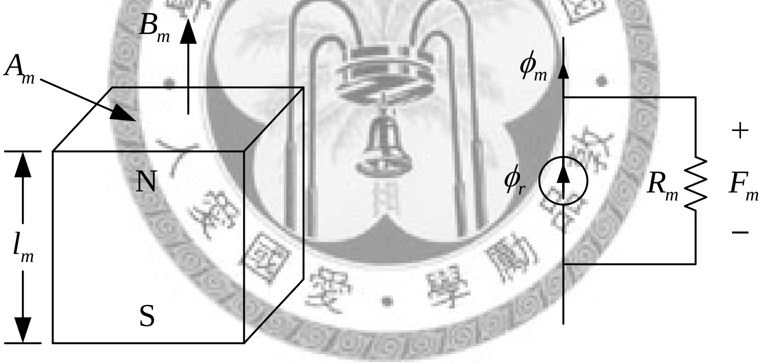

(a) (b)

Fig. 4.4 A rectangular magnet and its magnetic circuit

In order to facilitate the calculation, the value of reluctance is often represented as permeance, whose value is the inverse of reluctance. Therefore, the permeance of the rectangular magnet in Fig. 4.4 can be described as follows:

$$P_m = R_m{}^{-1} = \frac{\mu_R \mu_0 A_m}{l_m} \tag{4.18}$$

where P_m is conventionally called the magnet leakage permeance, although here it is simply called the magnet permeance.

4.1.3 Flux Linkage and Back-EMF

The determination of flux linkage is the total flux linked by the winding, which is expressed as

$$\lambda = N\phi \tag{4.19}$$

From equation (4.7) and (4.9), equation (4.19) can be rewritten as

$$\lambda = \frac{N^2}{R_e + R_g} i \tag{4.20}$$

The expression shows that flux linkage is directly proportional to the current flowing through the coil. As a result, it is common to define the constant relating current to flux linkage as inductance:

$$L = \frac{\lambda}{i} = \frac{N^2}{R_{eff}} = N^2 P_{eff} \tag{4.21}$$

where R_{eff} and P_{eff} are the effective reluctance and permeance of the core and air gap, respectively.

The primary significance of flux linkage is that it induces a voltage across the winding when the flux linkage varies with time. The voltage E that is induced by the variation of flux linkage is given by Faraday's law, which states:

$$E = \frac{d\lambda}{dt} \tag{4.22}$$

Applying equation (4.21) to (4.22), we obtain the following:

$$E = \frac{d\left(Li\right)}{dt} = L\frac{di}{dt} + i\frac{dL}{dt} \tag{4.23}$$

where the first term is referred to as the transformer voltage E_t, which is produced by the changing of the winding current, and the second term is the back-EMF E_b, whose amplitude is directly proportional to the speed of motor.

4.2 Determination of Design Variables

The dimension description of the flux shunt DC motor is shown in Fig. 4.5. Since this topology contains a stator and armature, the definition of design variables are separated into two parts: one is for the stator parameters, the other is for the armature.

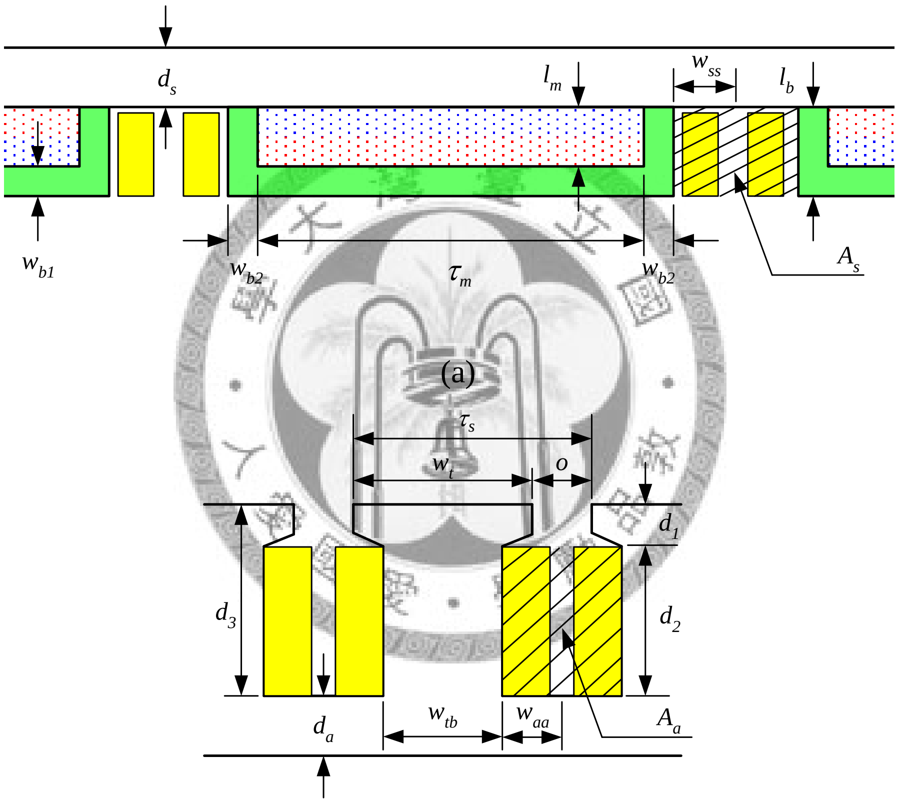

(a)

(b)

Fig. 4.5 Design variables of (a) stator, and (b)armature

Stator parameters are illustrated in Fig. 4.5 (a), where τ_m is the magnet width, l_m is the magnet length, d_s is the stator back iron width, l_b is the front permeable material length, w_{b1} is the front permeable material width, w_{b2} is the lateral permeable material width, w_{ss} is the half of the stator slot width, and A_s is the stator conductor area.

Armature parameters are illustrated in Fig. 4.5 (b), where d_1 is the tooth shoe depth, d_2 is the conductor slot depth, d_3 is the armature tooth depth, τ_s is the slot pitch, o is the slot opening width, w_t is the tooth top width, w_{tb} is the tooth bottom width, d_a is the armature back iron width, w_{aa} is half of the armature slot width, and A_a is the armature conductor area.

The relationship between design variables is discussed as follows:

The armature tooth depth is given by:

$$d_3 = d_1 + d_2 \tag{4.24}$$

The slot pitch is given by the number of slots N_s and the outer radius of armature R_a:

$$\tau_s = \frac{2\pi R_a}{N_s} \tag{4.25}$$

The tooth top width is related to the slot pitch τ_s and the slot opening width o by:

$$w_t = \tau_s - o \tag{4.26}$$

The armature conductor area A_a is determined by half of the armature winding width w_{aa} and conductor slot depth d_2:

$$A_a = 2w_{aa}d_2 \tag{4.27}$$

The stator conductor area A_s is determined by half of the stator winding width w_{ss} and the front permeable material length l_b:

$$A_s = 2w_{ss}l_b \tag{4.28}$$

Other parameters are defined as follows, including the air gap length g, motor axial length l, armature winding diameter d_{wa}, number of turns per armature slot N_a, stator winding diameter d_{ws}, and number of turns per stator slot N_f. The length of the air gap is the difference between the armature outer radius R_a and the stator inner radius R_s.

4.3 Magnetic Equivalent Circuit Construction

In this section, the magnetic equivalent circuit is proposed for the DC motor with an anti-demagnetization mechanism. Due to the symmetrical structure of the motor, the designed motor can be simplified by several minimum magnetic equivalent circuit models, each of which has 10 armature slots and 2 poles.

According to the assumptions of material linearity and collinear flux in the air gap, the magnetic circuit model and energy method are used to formulate the torque produced in the air gap. It is necessary to make the following assumptions:

(1) The stator magnetic material is operated in the linear region of the *B*-*H* curve.

(2) The air gap distribution of stator slot opening is approximated by the effective air gap distribution using Carter's coefficient [31].

(3) The flux flows straightly across the air gap between the stator and rotor, ignoring the leakage flux from teeth and magnets.

(4) The magnetic flux density is uniformly distributed in the stator magnetic material.

Based on these assumptions, a minimum magnetic circuit model of the DC motors having 10 slots and 2 poles can be constructed, as shown in Fig. 4.6 (a).

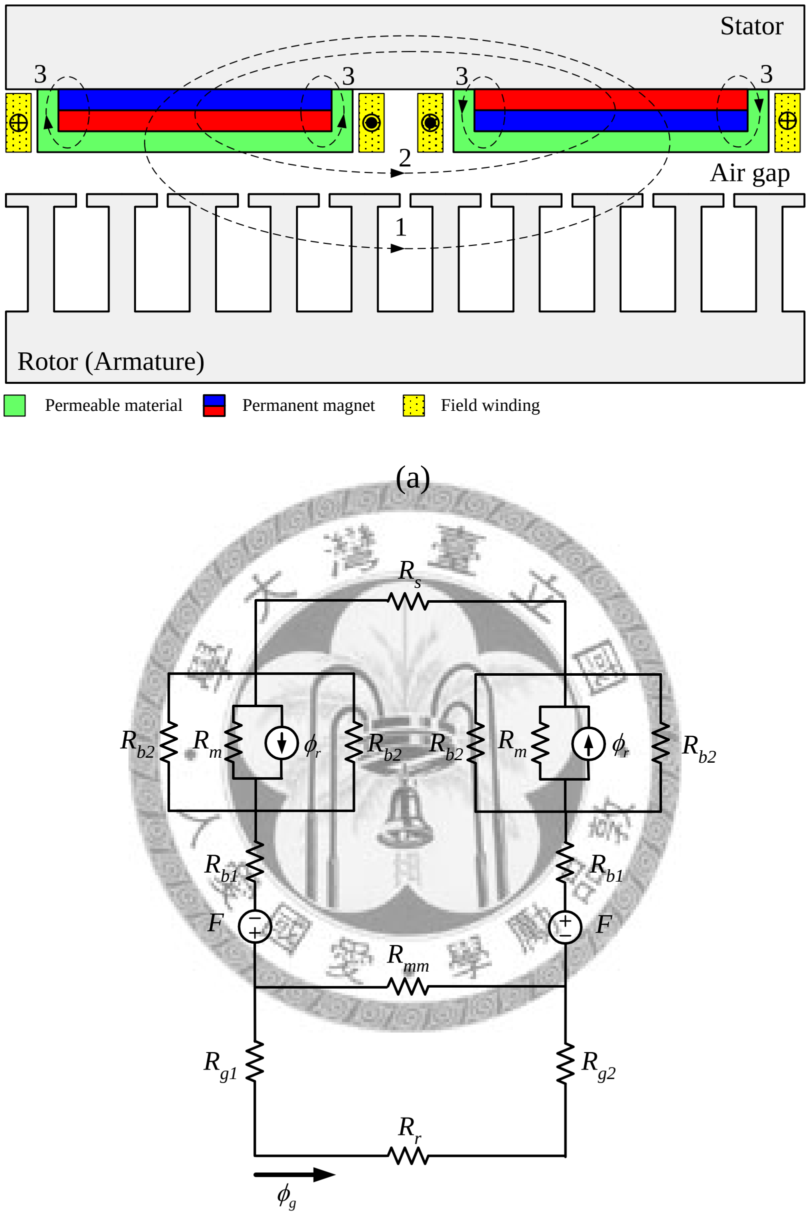

(a)

(b)

Fig. 4.6 Flux shunt DC motor minimum magnetic circuit (a) structure and (b) model

The flux path 1 is assumed to flow straight across the air gap between the stator and rotor. The overlapping area method [5] is used so that the fringing effects of flux are ignored in order to simplify the magnetic analysis. Therefore, the reluctance of the air gap length is modeled by R_{g1} and R_{g2}, which vary with rotor shift. The leakage flux flows through flux path 2 between two adjacent magnets, where the leakage reluctance is denoted by R_{mm}. The self-leakage of the permanent magnet is described in flux path 3, where it passes through the surrounding permeable material rather than air because the reluctance of the permeable material is much smaller than that of air. Hence, the reluctance of the permeable material is modeled as R_{b1} and R_{b2}. The magnet is represented by two parallel elements, ϕ_r and R_m, where ϕ_r is the remanence of the magnet and R_m is the reluctance of the magnet, R_s and R_r are the reluctances of the back iron of the stator and rotor, respectively, and F is the magneto-motive force produced by the field windings. Finally, ϕ_g is the air gap flux. The stator is made of iron and the rotor is made of silicon steel, whose permeability is much greater than air; therefore, R_s and R_r can be neglected in the magnetic circuit model. To simplify the analysis, the reluctance is represented by permeance and the simplified permeance network is shown in Fig. 4.7.

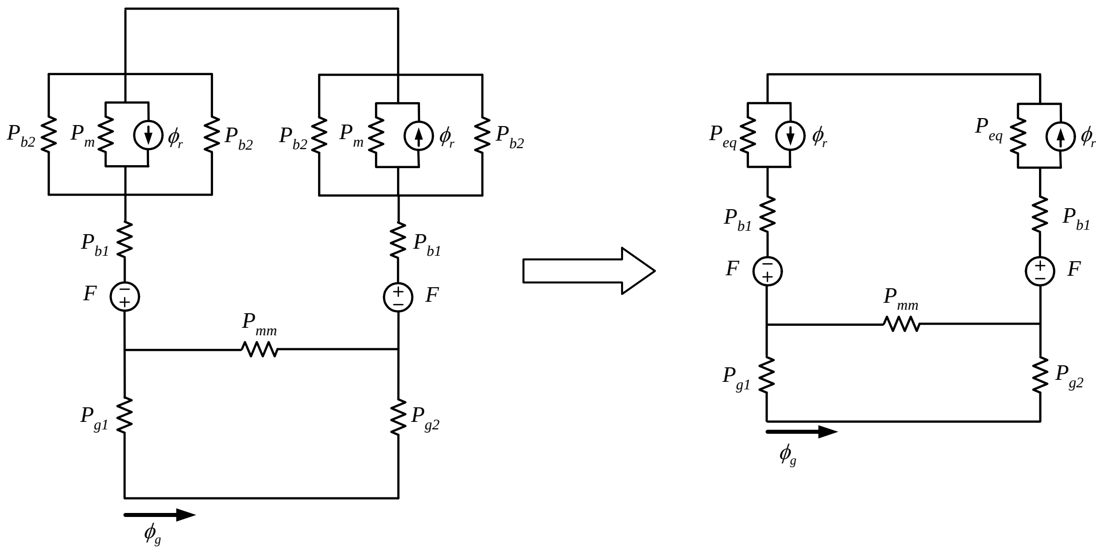

Fig. 4.7 The simplified flux shunt DC motor permeance network

4.3.1 Calculation of Air Gap Permeance

The air gap distribution in the circumferential direction is formulated explicitly as a function of motor geometries [31]. The variation of effective air gap in one slot pitch is shown in Fig. 4.8.

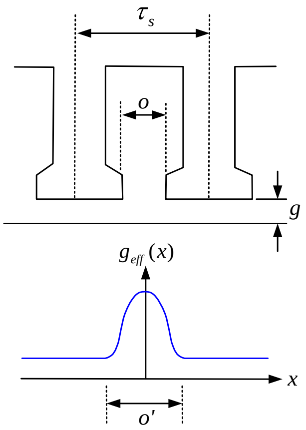

Fig. 4.8 The variation of the effective air gap in a one slot pitch

The effective air gap length on the rotor side is defined as:

$$g_{eff}(x)=\frac{g}{1-\beta\left(1-\cos\frac{2\pi}{o'}x\right)} \tag{4.29}$$

where

$$o'=\frac{t}{\beta}g \tag{4.30}$$

$$\beta=\frac{\left(1-u\right)^2}{2\left(1+u^2\right)} \tag{4.31}$$

$$t=\frac{4}{\pi}\left[\frac{o}{2g}\tan^{-1}\frac{o}{2g}-\ln\sqrt{1+\left(\frac{o}{2g}\right)^2}\right] \tag{4.32}$$

$$u=\frac{o}{2g}+\sqrt{1+\left(\frac{o}{2g}\right)^2} \tag{4.33}$$

where g is the minimum air gap length between the stator and armature, o is the slot opening width of the armature, and o' is the effective armature slot opening width.

The effective air gap distribution in a minimum magnetic circuit model is sketched in Fig. 4.9, where x represents the peripheral coordinate along the circumference of the air gap direction between the rotor and stator.

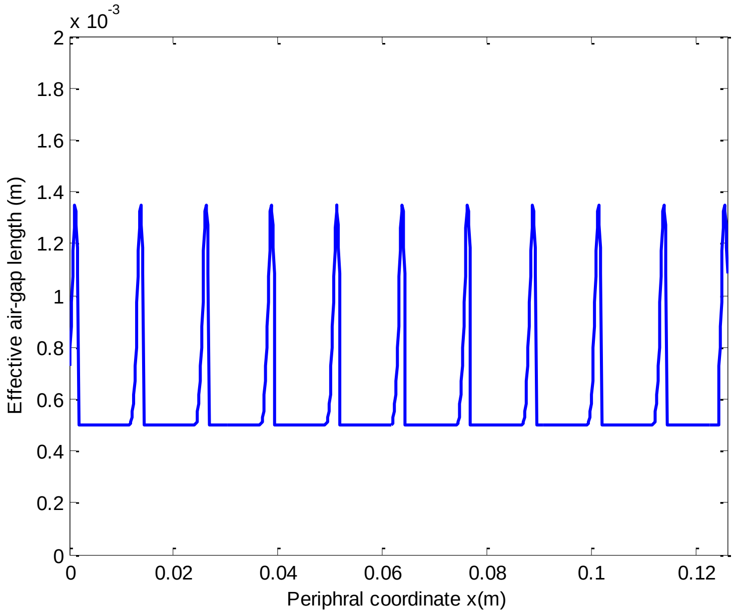

Fig. 4.9 The effective air gap on the rotor side in a minimum magnetic circuit model

In the case of a DC motor, the air gap length on the stator side g_s is established by the magnetic field poles; therefore, g_s is the function of magnet width τ_m and magnet length l_m, which are the geometry parameters of the magnet field poles. For simplicity, the g_s is assumed to be l_m and the total air gap length $\delta(x,s)$ is written as:

$$\delta(x,s) = g_{eff}(x) + g_s(x,s) \approx g_{eff}(x) + l_m \tag{4.34}$$

where s denotes the rotor shift.

The permeance of each slot can be solved by equations (4.18). The air gap permeance in the flux path is calculated by the overlapping area method [5], which is illustrated in Fig. 4.10.

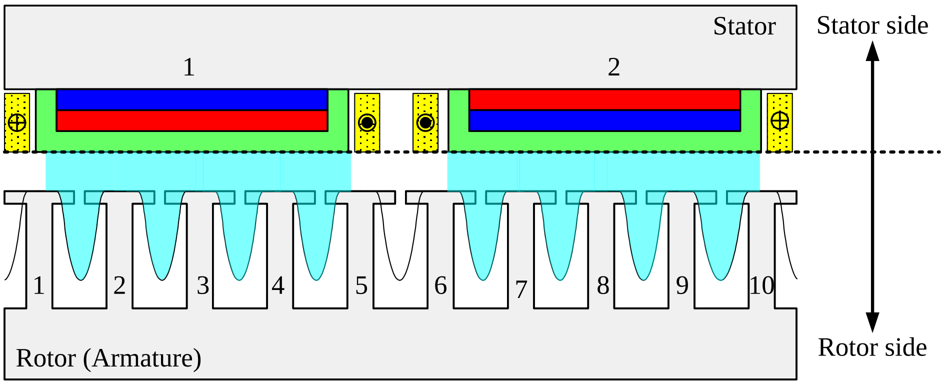

Fig. 4.10 Overlapping area method (s=0)

Because the flux is assumed to flow straight across the air gap between stator and rotor, the fringing flux effect can be ignored. Based on this assumption, the magnet's flux only flows through the slots that face the magnets. The permeance of each slot is proportional to the overlapping area of slot and magnet, which can be expressed as:

$$P_{gisj}(x,s) = \frac{\mu_0 A_{gisj}}{\delta(x,s)}, \begin{cases} i = 1,2 \\ j = 1,2,\ldots,10 \end{cases} \qquad s = 0^{\circ}\,\mathrm{E} \sim 360^{\circ}\,\mathrm{E} \tag{4.35}$$

where P_{gisj} represents the permeance of the j th slot in flux path of the i th magnet; therefore, P_{gisj} is zero if the j th slot does not overlap with any magnet. The overlapping area A_{gisj} of the j th slot and the i th magnet varies with respect to the rotor shift, thereby, P_{gisj} is a function of the rotor shift.

The rotor shift is defined as is shown in the initial position in Fig. 4.10, where slots 1 through 5 align with field pole 1 while slots 6 through 10 align with the field pole 2. It is clear that P_{g1} is a linear combination of P_{g1s1} through P_{g1s5}. Similarly, P_{g2} can be represented by a linear combination of P_{g2s6} through P_{g2s10}. As the rotor rotates, magnet 2 moves fictitiously back to slot 1 and the permeance of slot 1 is included in P_{g1} to complete a period of the magnetic circuit. Therefore, the air gap permeance aligning each magnet can be modeled as a several parallel connection slot permeances in the corresponding flux path, which is given by:

$$P_{g1} = P_{g1s1} + P_{g1s2} + P_{g1s3} + \ldots + P_{g1s10} \tag{4.36}$$

$$P_{g2} = P_{g2s1} + P_{g2s2} + P_{g2s3} + \ldots + P_{g2s10} \tag{4.37}$$

4.3.2 Calculation of Magnet, Permeable Material, and Leakage Permeance

The magnetic circuit of permanent magnets is constructed by (4.4). The magnet permeance can be calculated by:

$$P_m = \frac{\mu_R \mu_0 A_m}{l_m} \tag{4.38}$$

where the cross-sectional area of magnet A_m can be expressed as:

$$A_m = \tau_m l \tag{4.39}$$

The permeable material permeance can be modeled as two parts, which are P_{b1}

and P_{b2}. The former is referred to as the permeance of flux path 2; the latter is referred to as the permeance of flux path 3.

The front permeable material permeance P_{b1} can be calculated by:

$$P_{b1} = \frac{\mu_R \mu_0 A_m}{w_{b1}} \tag{4.40}$$

The self-leakage of a permanent magnet pole in flux path 3 passes through each lateral permeable material; therefore, the lateral permeable material permeance P_{b2} can be calculated by:

$$P_{b2} = \frac{\mu_R \mu_0 w_{b2} l}{l_b} \tag{4.41}$$

Because permeances P_{b2} and P_m are connected in parallel in Fig. 4.7, the equivalent permeance can be calculated by:

$$P_{eq} = P_{b2} + P_{b2} + P_m \tag{4.42}$$

The leakage permeance of a permanent magnet pole in flux path 2 between each pair of adjacent magnets can be described as [32]:

$$P_{mm} = \frac{\mu_0 l}{\pi} \ln[1 + \frac{\pi g}{2 w_{ss}}] \tag{4.43}$$

4.3.3 Calculation of Air Gap Flux

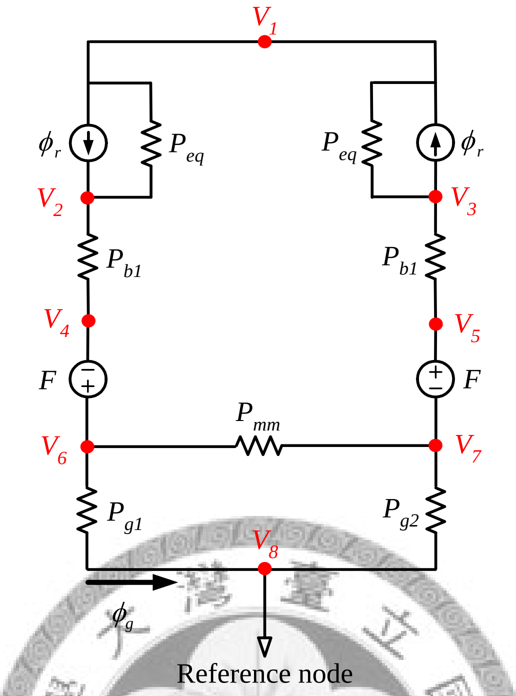

Fig. 4.11 Node voltage method

After the permeances of the magnetic circuit model are acquired, the air gap flux can be determined by Kirchhoff's Current Law (KCL). According to KCL, the node voltage method is employed to formulate the voltage equations; the selected nodes of the magnet circuit are shown in Fig. 4.11. There are eight nodes in the magnet circuit, V_1 through V_8. Assuming that V_8 is the reference node, whose voltage is set to zero, then the others voltage nodes will have their relative values referred to V_8.

By applying the KCL, the voltage equations of the magnet circuit can be formulated as follows:

$$\begin{cases} \left(V_2 - V_1\right) P_{eq} + \left(V_3 - V_1\right) P_{eq} = 0 \\ \left(V_1 - V_2\right) P_{eq} + \left(V_4 - V_2\right) P_{b1} = -\phi_r \\ \left(V_1 - V_3\right) P_{eq} + \left(V_5 - V_3\right) P_{b1} = \phi_r \\ \left(V_2 - V_4\right) P_{b1} + \left(V_7 - V_6\right) P_{mm} + \left(V_8 - V_6\right) P_{g1}(s) = 0 \\ \left(V_3 - V_5\right) P_{b1} + \left(V_6 - V_7\right) P_{mm} + \left(V_8 - V_7\right) P_{g2}(s) = 0 \\ V_6 - V_4 = F \\ V_5 - V_7 = F \end{cases} \tag{4.44}$$

Equation (4.44) can be written as a matrix form

$$\left[P\right]\left[V\right] = \left[Q\right] \tag{4.45}$$

where $\left[V\right]$ is the node voltage vector, $\left[Q\right]$ is the magnetomotive force (mmf)/ magnet flux source vector, and $\left[P\right]$ is the permeance matrix.

The magnetomotive force (mmf)/magnet flux source vector $\left[Q\right]$ is formulated by

$$\left[Q\right] = \left[0 \quad -\phi_r \quad \phi_r \quad 0 \quad 0 \quad F \quad F\right]^T \tag{4.46}$$

where ϕ_r is the magnet flux source and is the magnetomotive force (mmf) of the field windings. The permeance matrix is given by:

$$\left[P\right] = \begin{bmatrix} -2P_{eq} & P_{eq} & P_{eq} & 0 & 0 & 0 & 0 \\ P_{eq} & -P_{b1} - P_{eq} & 0 & P_{eq} & 0 & 0 & 0 \\ P_{eq} & 0 & -P_{b1} - P_{eq} & 0 & P_{b1} & 0 & 0 \\ 0 & P_{b1} & 0 & -P_{b1} & 0 & -P_{mm} - P_{g1} & P_{mm} \\ 0 & 0 & P_{b1} & 0 & -P_{b1} & P_{mm} & -P_{mm} - P_{g2} \\ 0 & 0 & 0 & -1 & 0 & 1 & 0 \\ 0 & 0 & 0 & 0 & 1 & 0 & -1 \end{bmatrix} \tag{4.47}$$

The seven independent equations shown in (4.44) have seven unknown variables V_1, V_2, … , V_6, and V_7. The solution can be obtained by solving these linear equations. Subsequently, the flux distributions of each slot are calculated by:

$$\phi_{sj} = \left(V_6 - V_8\right) P_{g1sj} + \left(V_7 - V_8\right) P_{g2sj} \tag{4.48}$$

where $j = 1, 2, ..., 10$.

The flux distribution ϕ_{s1}, ϕ_{s2}, …, and ϕ_{s10} in an electrical cycle of a rotor shift is illustrated in Fig. 4.12. In this figure, the relative position of the armature and stator is $0^\circ E$, as shown in Fig. 4.10. At this moment, the N-pole of magnet 1 faces the armature slots; therefore, the flux in slots 1 through 5 is positive. In addition, slot 1 and slot 5 face only a portion of magnet 1; hence the received flux of slot 1 and slot 5 is less than that of slots 2 through 4. In contrast, the S-pole of magnet 2 faces the stator, so the fluxes in slots 6 through 10 are negative. Similarly, slot 6 and slot 10 face only a portion of magnet 2; hence the received flux of slot 6 and slot 10 is less than for slots 7 through 9. In addition, as the armature shifts from $0^\circ \mathrm{E}$ to $360^\circ \mathrm{E}$, the flux flowing through each slot varies with respect to the relative position of the magnets.

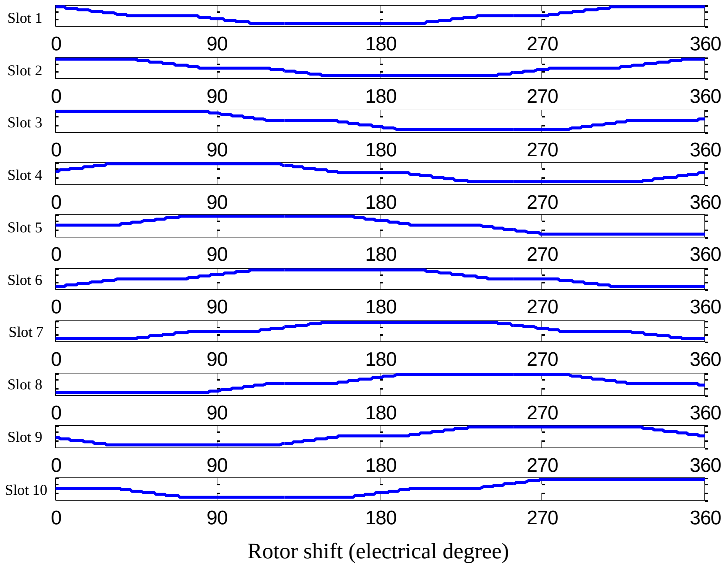

Fig. 4.12 Flux distribution in each slot

4.3.4 Calculation of Torque

Torque is produced by the variation of coenergy with respect to rotor shift, which is defined as the relative angle between the rotor and stator. The field coenergy in the air gap can be calculated by:

$$W_c\left(s\right)=\int Fd\phi=\int FB_g dA=\mu_0 l\int_0^{2\pi R_a}\frac{F^2(x,s)}{\delta(x,s)}dx \tag{4.49}$$

where l is the motor length, μ_0 is the permeability of air gap, B_g is the flux density distribution in the air gap, $F(x,s)$ is the MMF distribution in the air gap and $\delta(x,s)$ is the total air gap length.

The output torque is then calculated by the rate of coenergy change in the air gap, which is expressed as:

$$T(s) = R_a \left. \frac{\partial W_c(s)}{\partial s} \right|_{i=const.} \tag{4.50}$$

where s is denoted the rotor shift, W_c is denoted the magnetic coenergy, and R_a is the outer radius of the armature.

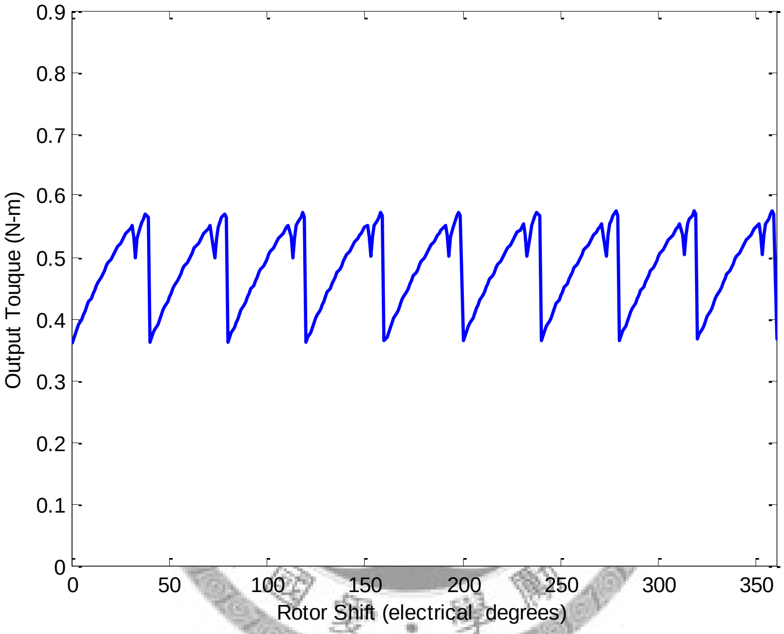

Fig. 4.13 Torque calculated by the magnetic circuit model

In order to calculate torque by a numerical method, the reduced continuous coenergy and torque equation can be transformed to discrete forms as follows:

$$W_c(\beta\Delta\theta) = \mu_0 l \Delta\theta \sum_{n=1}^{N} \frac{F^2(k\Delta\theta, \beta\Delta\theta)}{\delta(k\Delta\theta, \beta\Delta\theta)} \quad k, \beta = 1, 2, 3... \tag{4.51}$$

$$T\left(\beta\Delta\theta\right)=\left.\frac{W_c\left((\beta+1)\Delta\theta\right)-W_c\left(\beta\Delta\theta\right)}{\Delta\theta}\right|_{i=const.}\qquad k,\beta=1,2,3... \tag{4.52}$$

in which the electrical period ($360^\circ E$) is divided by N equally spaced points, each with a mechanical position apart from $\Delta\theta$ and $s=\beta\Delta\theta$. The torque calculated by the magnetic circuit model is shown in Fig. 4.13. The MATLAB m-files of the magnetic circuit are attached in Appendix A.

4.3.5 Calculation of Inductance

The inductances can be calculated by winding function method [31] [33], which states that the inductances between any two windings i and j is

$$L_{ij}(s)=\mu_0 R_a l\int_0^{2\pi}\frac{N_i(x)N_j(x)}{\delta(x,s)}dx \tag{4.53}$$

where μ_0 is the permeability coefficient of air gap, R_a armature outer radius, l is motor axial length, N_i and N_j are the winding functions for windings i and j, respectively, δ is air gap length, s is the rotor shift, and x is the peripheral coordinate.

Before the calculation of inductance, the winding functions need to be defined. In flux shunt DC motor, there are armature windings and field windings, which is defined as follow:

The winding function of armature winding is defined as

$$N_{aa}(x)=\frac{4N_a}{\pi}\sum_{k=1}^{\infty}\sin(k\frac{\pi x}{\tau_s}) \tag{4.54}$$

where N_a is the number of turns per armature slot and τ_s is the slot pitch.

The winding function of field winding is defined as

$$N_{ff}(x)=\frac{4N_f}{\pi}\sum_{k=1}^{\infty}\sin(k\frac{\pi x}{\tau_p}) \tag{4.55}$$

where N_f is the number of turns per stator slot and τ_p is the pole pitch.

The self inductance of the armature winding is calculated by

$$L_{aa}(s)=\mu_0 R_a l\int_0^{2\pi}\frac{N_{aa}^2(x)}{\delta(x,s)}dx \tag{4.56}$$

and the average self inductance of the armature winding $\overline{L}_{aa}$ is calculated by

$$\overline{L}_{aa}=\frac{1}{2\pi}\int_0^{2\pi}L_{aa}(s)ds \tag{4.57}$$

The self inductance of the armature winding calculated by (4.56) is shown in Fig. 4.14.

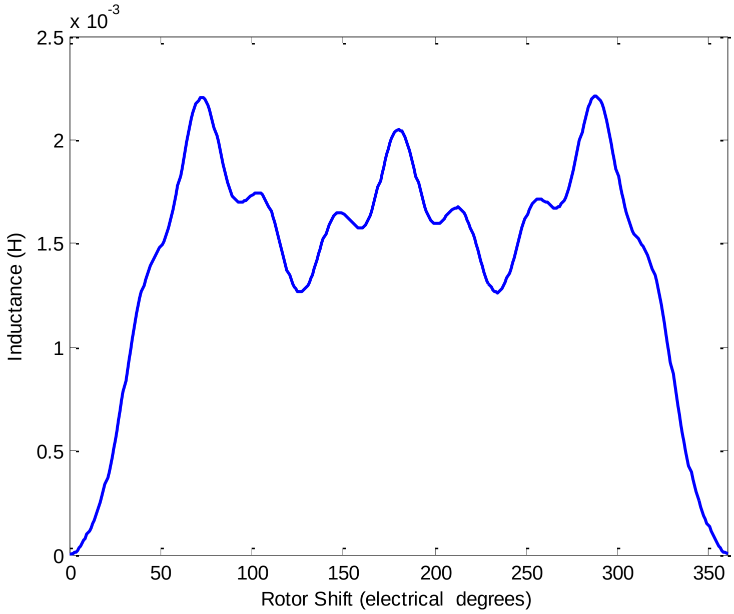

Fig. 4.14 Self inductance of the armature winding

The self inductance of the field winding is calculated by

$$L_{ff}(s) = \mu_0 R_a l \int_0^{2\pi} \frac{N_{ff}^2(x)}{\delta(x,s)} dx \tag{4.58}$$

and the average self inductance of the field winding $\overline{L}_{ff}$ is calculated by

$$\overline{L}_{ff} = \frac{1}{2\pi} \int_0^{2\pi} L_{ff}(s) ds \tag{4.59}$$

The self inductance of the field winding calculated by (4.58) is shown in Fig. 4.15.

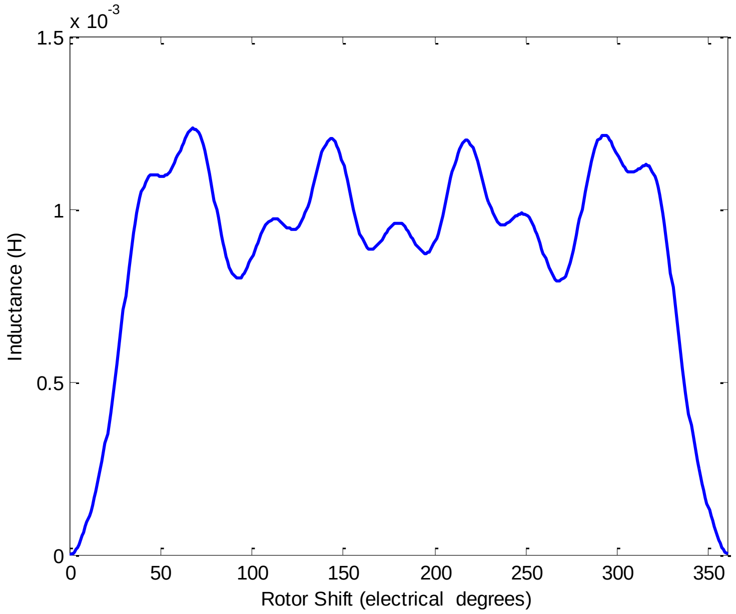

Fig. 4.15 Self inductance of the field winding

The mutual inductance between the armature winding and the field winding is calculated by

$$L_{af}(s) = \mu_0 R_a l \int_0^{2\pi} \frac{N_{aa}(x) N_{ff}(x)}{\delta(x,s)} dx \tag{4.60}$$

and the average self inductance of the field winding $\overline{L}_{ff}$ is calculated by

$$\overline{L}_{af} = \frac{1}{2\pi} \int_0^{2\pi} L_{af}(s) ds \tag{4.61}$$

The mutual inductance between the armature winding and the field winding calculated by (4.60) is shown in Fig. 4.16. The MATLAB m-file of these inductances calculation is attached in Appendix A.

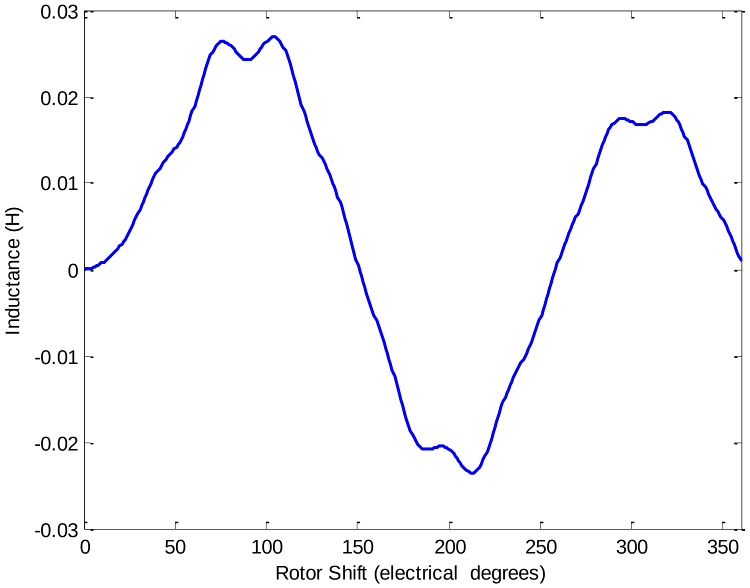

Fig. 4.16 Mutual inductance between the armature winding and the field winding

4.3.6 Calculation of Speed

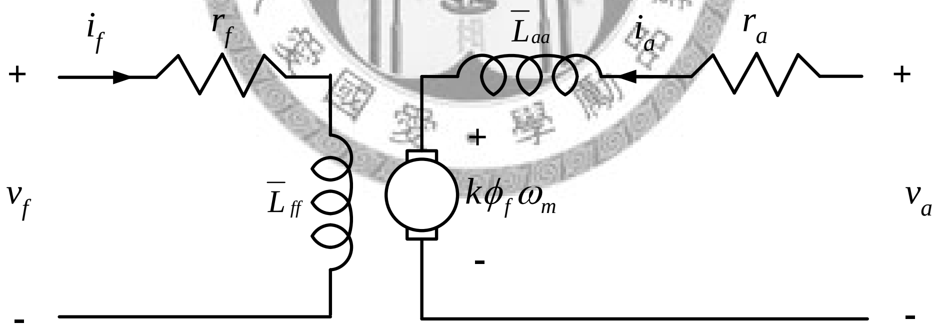

Fig. 4.17 Equivalent circuit of a flux shunt DC motor

The equivalent circuit of a flux shunt DC motor is constructed in Fig. 4.17. By applying Kirchoff's voltage law to write voltage equations, the field winding voltage and armature winding equation can be expressed by (4.62) and (4.63), respectively.

$$v_f = r_f i_f + \bar{L}_{ff} \frac{di_f}{dt} \tag{4.62}$$

$$v_a = r_a i_a + \bar{L}_{aa} \frac{di_a}{dt} + k\phi_f \omega_m \tag{4.63}$$

where v_f is the field winding voltage, r_f is the field winding resistance, i_f is the field winding current, $\bar{L}_{ff}$ is the average field winding self inductance; v_a is armature winding voltage, r_a is the armature winding resistance, i_a is the armature winding current, $\bar{L}_{aa}$ is the average armature winding self inductance, ϕ_f is the field flux, k is a constant and ω_m is the mechanical angular speed.

Because the field flux can be controlled by additional field windings, it can be written as:

$$k\phi_f = \bar{L}_{af} i_f + \phi_r \tag{4.64}$$

where $\bar{L}_{af}$ is the average mutual inductance between armature winding and field winding, i_f is the field winding current, and ϕ_r is the remanence flux.

Therefore, the armature voltage equation can be rewritten as:

$$v_a = r_a i_a + \bar{L}_{aa} \frac{di_a}{dt} + (\bar{L}_{af} i_f + \phi_r)\omega_r \tag{4.65}$$

and the mechanical angular speed equation can be represented by:

$$\omega_m = \frac{v_a - r_a i_a - \bar{L}_{aa}\frac{di_a}{dt}}{\bar{L}_{af} i_f + \phi_r} \tag{4.66}$$

According to (4.66), the field flux is inversely proportional to the mechanical angular speed. Since the field flux is controlled by the field winding current, so also is the mechanical angular speed. A continuously variable speed technique can therefore be implemented by this machine.

4.4 Sensitivity Analysis

Before the optimization process, the designer has to evaluate the influences of design parameters on the objective functions. Sensitivity analysis is implemented to assess how objective functions are influenced by a single design variable by assuming that other design variables are kept constant. The objective functions chosen in sensitivity analysis are output torque, speed, efficiency, and weight.

4.4.1 Objective Functions

Objective functions are chosen for sensitivity analysis and the optimization process. The objective functions are defined in this section.

(1) Output torque

The torque equation is calculated by:

$$T\left(s\right)=R_a\left.\frac{\partial W_c(s)}{\partial s}\right|_{i=const.} \tag{4.67}$$

where s is denoted the rotor shift, W_c is denoted the magnetic coenergy, and R_a is the outer radius of the armature.

(2) Speed

The speed of a motor is proportional to the driving voltage and inversely proportional to the field flux. The maximum speed of motor can be obtained by equation (4.66).

(3) Efficiency

In the energy conversion process, power losses of an electrical machine can be categorized as copper losses, magnet losses, iron losses, and mechanical losses. Therefore, the relation between input power and output power is given by:

$$P_{in} = P_{shaft} + P_{copper} + P_{PM} + P_{iron} + P_{mech} \tag{4.68}$$

where P_{in} is the input electrical power, P_{shaft} is the output apparent motor shaft power, P_{copper} is the copper loss, P_{PM} is the magnet loss, P_{iron} is the iron loss and P_{mech} is the mechanical loss.

The apparent motor shaft output power is defined as:

$$P_{shaft} = T\omega_m \tag{4.69}$$

where T is the output torque actually transferred through the motor shaft and ω_m is the mechanical angular speed. The power flow diagram of an electrical machine is shown in Fig. 4.18. Loss calculations for each component are introduced in the following sections.

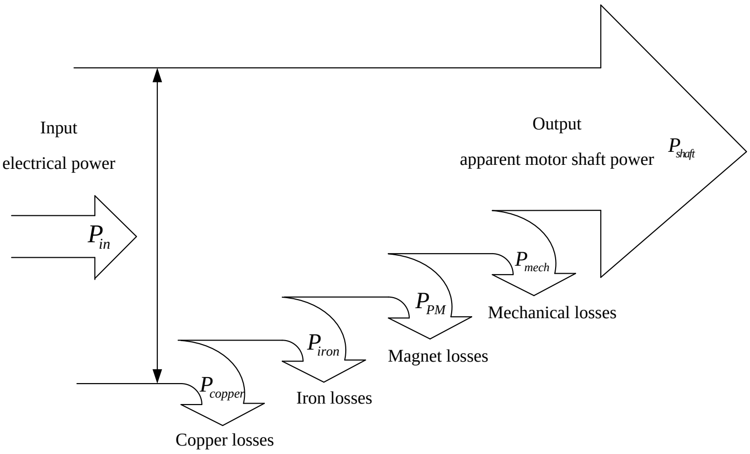

Fig. 4.18 Power flow diagram of an electrical machine

Copper loss is also referred to winding or ohmic loss and is the effect of time-varying current in copper coils. Copper loss mainly includes the DC resistance loss $P_{winding,DC}$ and the eddy current loss $P_{winding,eddy}$. Accordingly, copper losses can be expressed as:

$$P_{copper} = P_{winding,DC} + P_{winding,eddy} \tag{4.70}$$

The DC-resistance loss is related to the coil length, cross-sectional area, and material resistivity of the copper coils. Therefore, the DC resistance R_{DC} for a single phase winding is given by:

$$R_{DC} = \frac{\rho\, l_w}{A} \tag{4.71}$$

where l_w is coil length, A is cross-section area and ρ is the resistivity. The resistivity of copper is $1.72\times10^{-8}\,\Omega\bullet m$ at 20^oC.

In general, DC resistance losses of a single phase electric machine can be represented as:

$$P_{winding,DC} = R_{DC} I_{rms}^{2} \tag{4.72}$$

where I_{rms} is the RMS phase current for one phase winding.

Eddy current losses in windings can be attributed to skin effects, internal proximity effects and external alternating magnetic fields. Especially in a small volume machine, the eddy current losses are a minor component of the copper losses and therefore can be neglected to simplify the calculation of copper losses.

The main explanation of loss in permanent magnets can be attributed to three aspects. First, because of the winding distribution, the harmonics of windings induce time-varying magnetic fields and therefore a loss in permanent magnets occurs. Second, because the current waveform generated by the invert (driver) contains time harmonics, it is regarded as the source that induces eddy currents. Third, slot effects in the machine lead to the variation of permeance and also induce eddy currents in permanent magnets, even in the no-load condition. Based on these three facts, eddy currents cause the bulk of the loss in permanent magnets and are significant, especially in high speed or high-frequency conditions.

The induced power loss in a single permanent magnet piece is given by [34] [35]:

$$P_{PM} = \frac{\sigma}{24} l_m t_m \tau_m^3 B^2 \omega_{eddy}^2 \tag{4.73}$$

where σ is the conductivity, B is the flux density produced by the applied MMF or permeance variation, ω_{eddy} is the angular frequency of the eddy current, l_m is the magnet length, t_m is the thickness of magnet, and τ_m is the magnet width. According to (4.73), the induced power losses in a permanent magnet are closely related to its dimensions.

Iron loss is also referred to as core loss and includes the hysteresis and eddy current loss components in silicon steels in electric machines. Silicon steels are excited by the alternative or simply sinusoidal magnetic fields. The alternative magnetic field dissipates energy in the material and it can be calculated by the area of hysteresis loop in BH curve. Hysteresis loss can be estimated as:

$$P_h = k_h f B^n \tag{4.74}$$

where k_h is a constant that depends on the type and dimensions of material, f is the excitation frequency of a silicon steel, and B is the flux density for the selected silicon steel. n is an exponent that depends on the material property of silicon steels and ranges between 1.5 and 2.5.

The other component of iron loss is the eddy current loss, which can be alleviated by increasing the lamination of silicon steels. Eddy current loss can be estimated as:

$$P_e = k_e h^2 f^2 B^2 \tag{4.75}$$

where h is the thickness of a silicon steel and k_e is a material constant.

Therefore, total iron loss can be estimated as:

$$P_{iron} = P_h + P_e \tag{4.76}$$

The resistances from wind and friction are another sources of losses while the machine is in operation. Windage loss is caused by gaseous particles sliding on the rotor surface. It can be estimated as [35]:

$$P_{windage} = \frac{\pi}{16} C_f \rho_a \omega_m^3 D_a^4 l \tag{4.77}$$

where ρ_a is the mass density of air, which is usually selected as $\rho_a = 1.092$ kg/m^3 at $40^\circ C$, ω_m is the mechanical angular speed, D_a is the diameter, and l is the length of the armature respectively, C_f is the windage friction coefficient that depends on geometrical dimensions and the state of the gaseous flow.

The other component of mechanical losses is friction loss, which arises from the internal friction in bearings. It can be estimated as:

$$P_{bearing} = C_b D_b^3 \omega_m \tag{4.78}$$

where C_b is the bearing coefficient related to the bearing type, D_b is the diameter of the bearing. Therefore, mechanical loss P_{mech} is expressed as:

$$P_{mech} = P_{windage} + P_{bearing} \tag{4.79}$$

Therefore, the efficiency can be calculated by the ratio between the shaft output power and the electrical input power, as follows:

$$\eta = \frac{T\omega_m}{T\omega_m + P_{copper} + P_{PM} + P_{iron} + P_{mech}} \times 100\% \tag{4.80}$$

(4) Weight

The motor weight is determined by the motor volume and the density of materials. Mathematically, it is represented as:

$$W_m = \sum \rho_i \, V_i \tag{4.81}$$

where ρ_i and V_i represent the density and volume of the different components of motor, respectively.

4.4.2 Sensitivity Analysis

Sensitivity analysis is executed to determine how the objective functions are influenced by each single design variable while other design variable kept constant. The initial value of the selected design variables and their corresponding objective functions are listed in Table 4.1. The result of sensitivity analysis for each design variable will be discussed as follows.

Table 4.1 The initial value of design variables and their corresponding objective functions

<table>
<tr><th>No.</th><th>Variable</th><th>Symbol</th><th>Initial value</th><th>Range</th></tr>
<tr><td>1</td><td>Tooth shoe depth</td><td>d_1</td><td>0.8 mm</td><td>0.8~1.3</td></tr>
<tr><td>2</td><td>Conductor slot depth</td><td>d_2</td><td>13 mm</td><td>13~18</td></tr>
<tr><td>3</td><td>Slot opening width</td><td>o</td><td>1 mm</td><td>1~1.5</td></tr>
<tr><td>4</td><td>Half of the armature slot width</td><td>w_{tb}</td><td>1.5 mm</td><td>1.5~3</td></tr>
<tr><td>5</td><td>Armature back iron width</td><td>d_a</td><td>12.5 mm</td><td>12.5~15</td></tr>
<tr><td>6</td><td>Magnet length</td><td>l_m</td><td>7 mm</td><td>7~9.5</td></tr>
<tr><td>7</td><td>Magnet width</td><td>τ_m</td><td>44.26 mm</td><td>44.26~47</td></tr>
<tr><td>8</td><td>Armature outer radius</td><td>R_a</td><td>40 mm</td><td>40~42.5</td></tr>
<tr><td>9</td><td>Stator back iron width</td><td>d_s</td><td>12.75 mm</td><td>12.75~15.3</td></tr>
<tr><td>10</td><td>Air gap length</td><td>g</td><td>0.5 mm</td><td>0.5~0.8</td></tr>
<tr><td>11</td><td>Motor axial length</td><td>l</td><td>100 mm</td><td>100~120</td></tr>
<tr><td>12</td><td>Number of turns per armature slot</td><td>N_a</td><td>64 turns</td><td>64~80</td></tr>
<tr><th colspan="5">Operation condition</th></tr>
<tr><td colspan="2">Armature voltage</td><td colspan="3">48V</td></tr>
<tr><td colspan="2">Armature current</td><td colspan="3">10A</td></tr>
<tr><td colspan="2">Field voltage</td><td colspan="3">0V</td></tr>
<tr><td colspan="2">Field current</td><td colspan="3">0V</td></tr>
<tr><th colspan="5">Corresponding objective functions</th></tr>
<tr><td colspan="2">Torque</td><td colspan="3">4.2 N-m</td></tr>
<tr><td colspan="2">Speed</td><td colspan="3">3147 rpm</td></tr>
<tr><td colspan="2">Efficiency</td><td colspan="3">80.7 %</td></tr>
<tr><td colspan="2">Weight</td><td colspan="3">6.98 kg</td></tr>
</table>

(1) Tooth shoe depth d_1

The sensitivity of tooth shoe depth is shown in Fig. 4.19. The changes in tooth shoe depth affecting torque, speed, and efficiency approximate zero. This is because the armature material property is assumed to be linear in the region of the B-H curve. Therefore, saturation behavior of the armature is not observed in our analysis. Empirically, a small tooth shoe depth causes efficiency to degrade with the flux saturation in the tooth shoe. In addition, the increase in shoe depth slightly decreases the total weight of the armature.

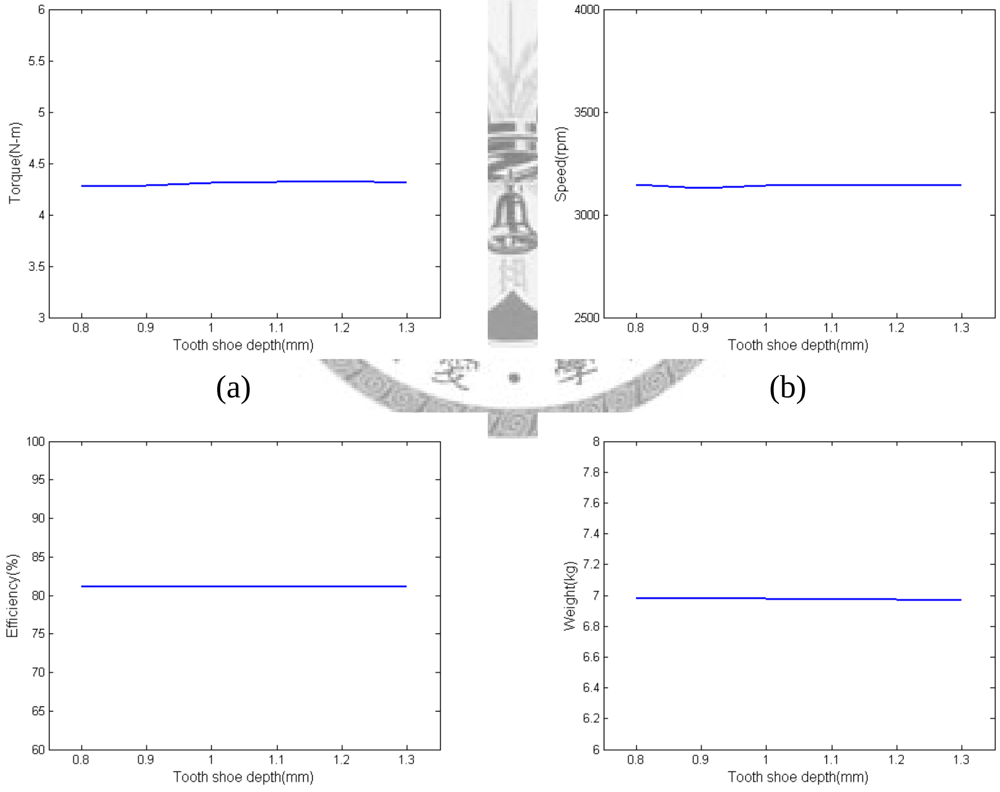

(a) (b)

(c) (d)

Fig. 4.19 Sensitivity of (a) Torque, (b) Speed, (c) Efficiency, and (d) Weight versus tooth shoe depth

(2) Conductor slot depth d_2

The sensitivity of conductor slot depth is shown in Fig. 4.20. Conductor slot depth does not influence the torque, speed, or efficiency but mainly influences the armature winding space. Because the volume armature material is decreased by the increasing of conductor slot depth, the motor weight is also decreased. A deeper slot depth on the armature offers more space to insert copper conductors.

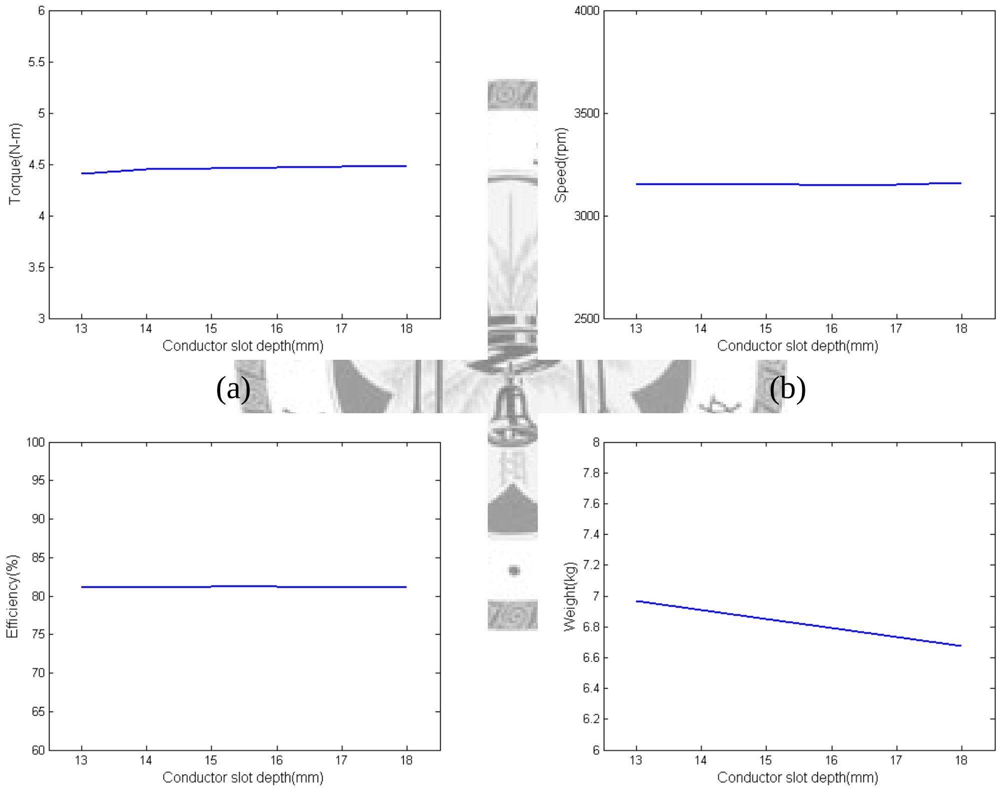

(a) (b)

(c) (d)

Fig. 4.20 Sensitivity of (a) Torque, (b) Speed, (c) Efficiency, and (d) Weight versus conductor slot depth

(3) Slot opening width o

The sensitivity of slot opening width is shown in Fig. 4.21. The slot opening width is related to the effective air gap distribution. Increases in slot opening result in the decrease of armature tooth width. Therefore, the flux flowing through the armature teeth is reduced, and consequently the output torque decreases. This will also decrease the efficiency because the magnet flux provided by the field poles does not entirely enter the armature teeth. In general, increases in slot opening width causes higher reluctance variation, but the decrease of slot opening width causes flux leakage between adjacent teeth. Empirically, the slot opening is suggested to be twice larger than the air gap.

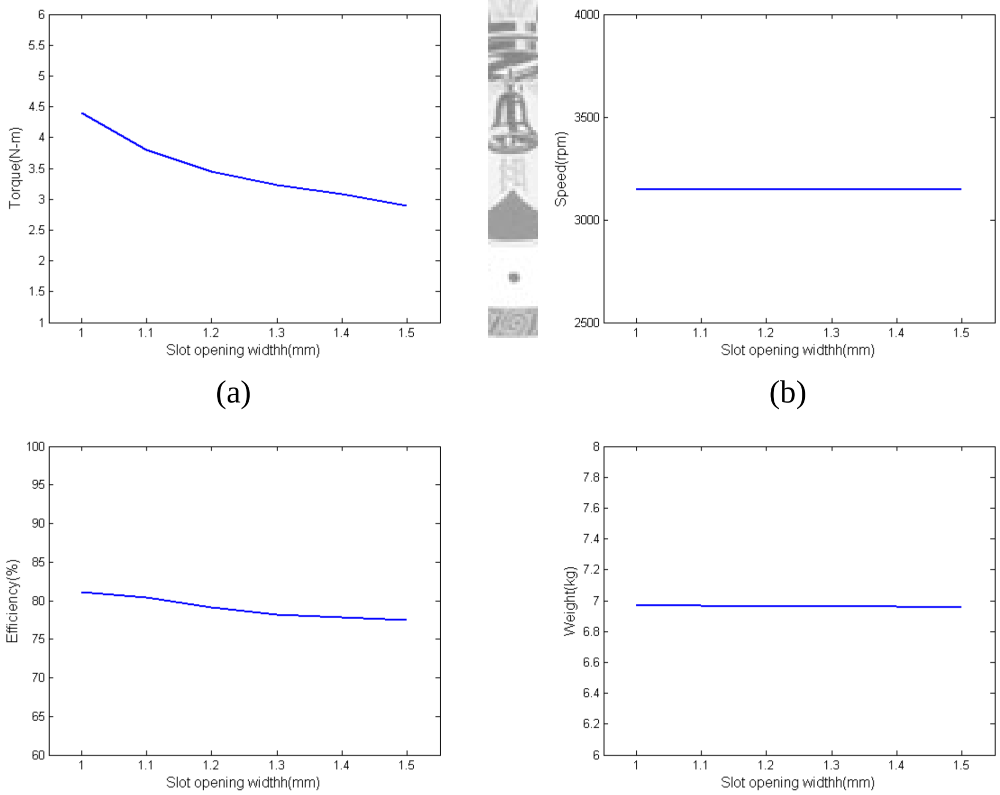

(a) (b)

(c) (d)

Fig. 4.21 Sensitivity of (a) Torque, (b) Speed, (c) Efficiency, and (d) Weight versus slot opening width

(4) Half of the armature slot width w_{aa}

The sensitivity of the half of the armature slot width is shown in Fig. 4.22. As was seen for the sensitivity of conductor slot depth, half of the armature slot width does not influence the torque, speed, and efficiency but mainly influences the armature winding space. Because the volume of armature material is decreased by increasing half of the armature slot width, the motor weight is also decreased. A wider half of the armature slot width offers more winding space into which copper conductors can be inserted.

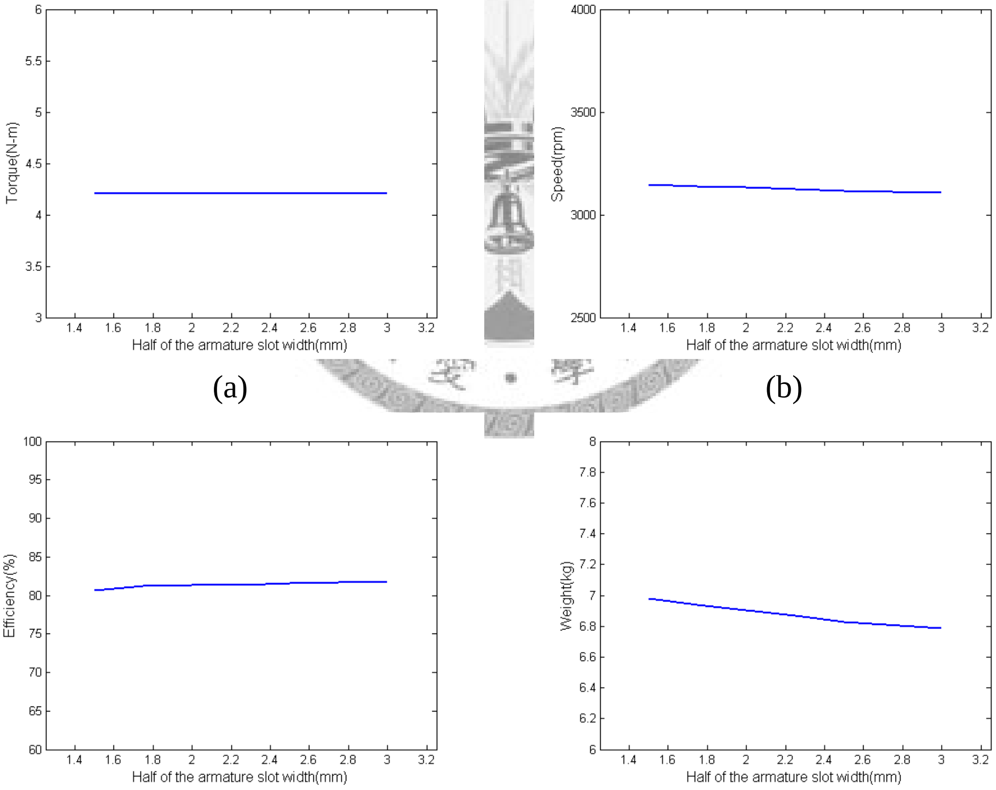

(a) (b)

(c) (d)

Fig. 4.22 Sensitivity of (a) Torque, (b) Speed, (c) Efficiency, and (d) Weight versus half of the armature slot width

(5) Armature back iron width d_a

The sensitivity of armature back iron width is shown in Fig. 4.23. The armature back iron is also used to establish a flux path for the MMF provided by armature winding and to form a closed magnetic circuit loop. Therefore, changes in the armature back iron affecting torque, speed, and efficiency approximates zero. Moreover, the increases in armature back iron will consume more materials; hence, the motor weight is also increased.

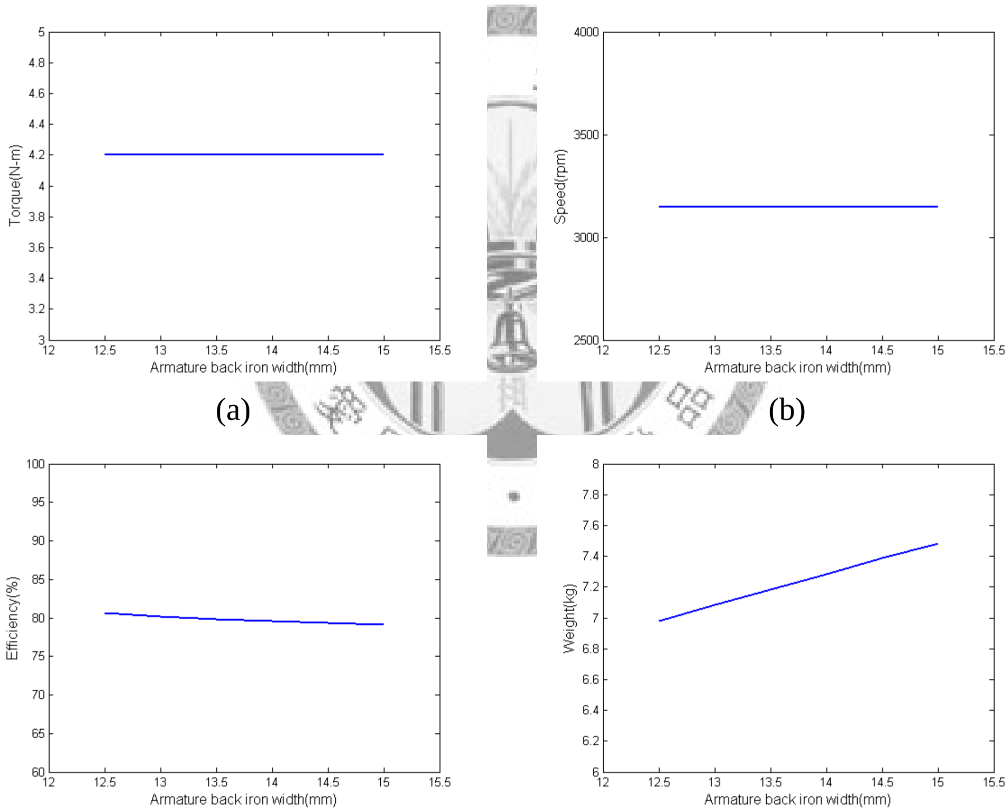

(a) (b)

(c) (d)

Fig. 4.23 Sensitivity of (a) Torque, (b) Speed, (c) Efficiencyt, and (d) Weight versus armature back iron width

(6) Magnet length l_m

The sensitivity of magnet length is shown in Fig. 4.24. The magnet length affects all of the objective functions, which means that the motor performance is closely related to magnet length. Because the magnet length dominates the stator MMF produced by magnets, an increase in stator MMF results a large field flux. Therefore, the torque and efficiency is increased significantly by increasing the magnet length. Moreover, the increases in magnet length will consume more materials; hence, the motor weight is also increased.

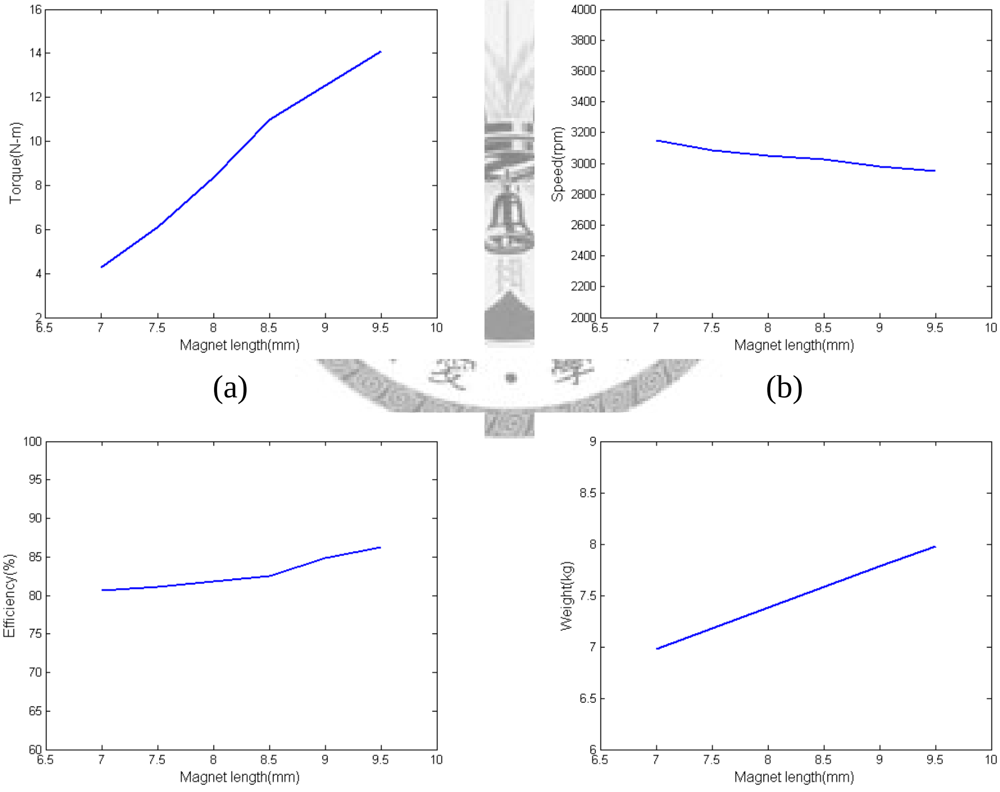

(a) (b)

(c) (d)

Fig. 4.24 Sensitivity of (a) Torque, (b) Speed, (c) Efficiency, and (d) Weight versus magnet length

(7) Magnet width τ_m

The sensitivity of magnet width is shown in Fig. 4.25. Similar to the magnet length, the magnet width affects all of the objective functions. Because the magnet width also dominates the stator MMF produced by magnets, the increases in stator MMF results in a large field flux. Therefore, the torque and efficiency is significantly increased by increasing the magnet width. If the field flux is increased, the speed is decreased for the same armature voltage. Moreover, the increases in magnet width will consume more materials; hence, the motor weight is also increased.

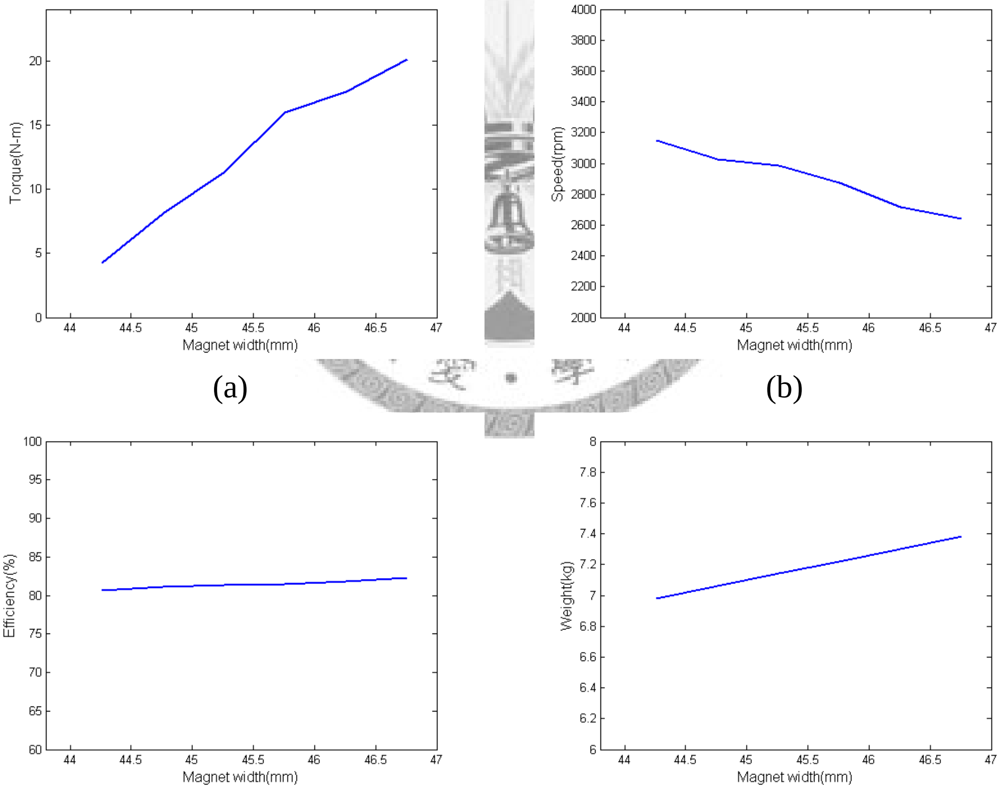

(a) (b)

(c) (d)

Fig. 4.25 Sensitivity of (a) Torque, (b) Speed, (c) Efficiency, and (d) Weight versus magnet width

(8) Armature outer radius R_a

The sensitivity of armature outer radius is shown in Fig. 4.26. The output torque is usually increased proportionally to the armature outer radius. Increasing the armature outer radius of a motor will also increase the use of materials; therefore, the motor weight has a significant increase, which is proportionally to the armature outer radius of the motor.

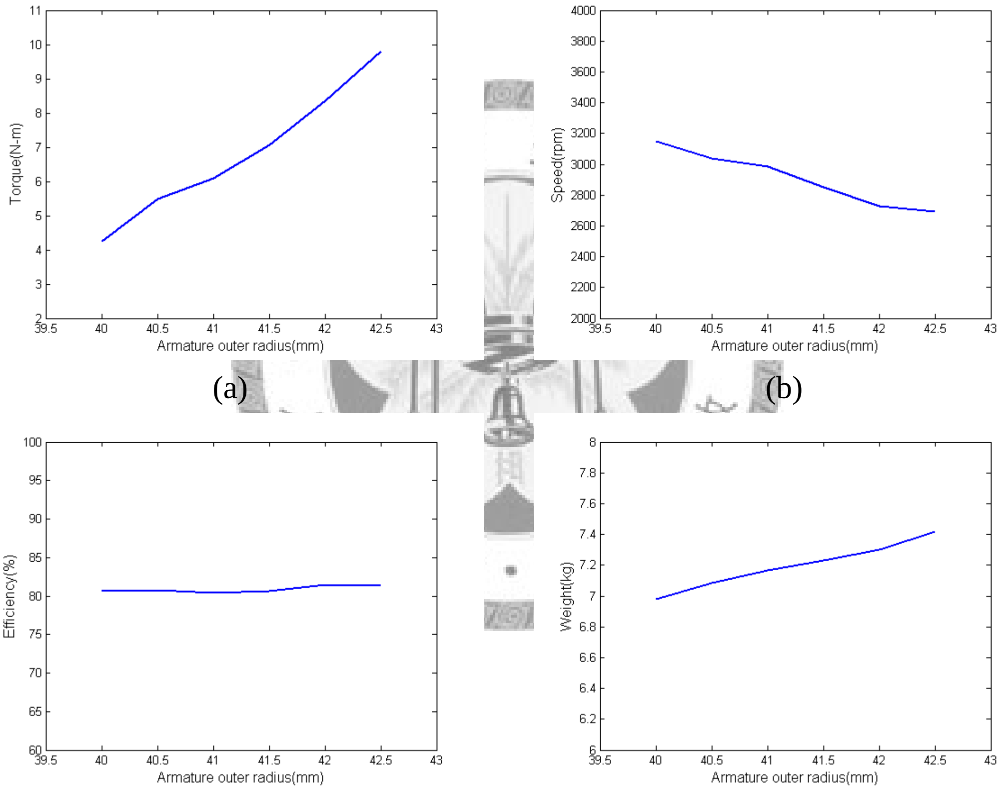

(a) (b)

(c) (d)

Fig. 4.26 Sensitivity of (a) Torque, (b) Speed, (c) Efficiency, and (d) Weight versus armature outer radius

(9) Stator back iron width d_s

The sensitivity of stator back iron width is shown in Fig. 4.27. The stator back iron is also used to provide a flux path for magnetic flux so that the magnetic circuit loop is closed. Therefore, changes in the stator back iron affecting torque, speed, and efficiency approximates zero. Moreover, the increasing of stator back iron will consume more materials; hence, the motor weight is also increased.

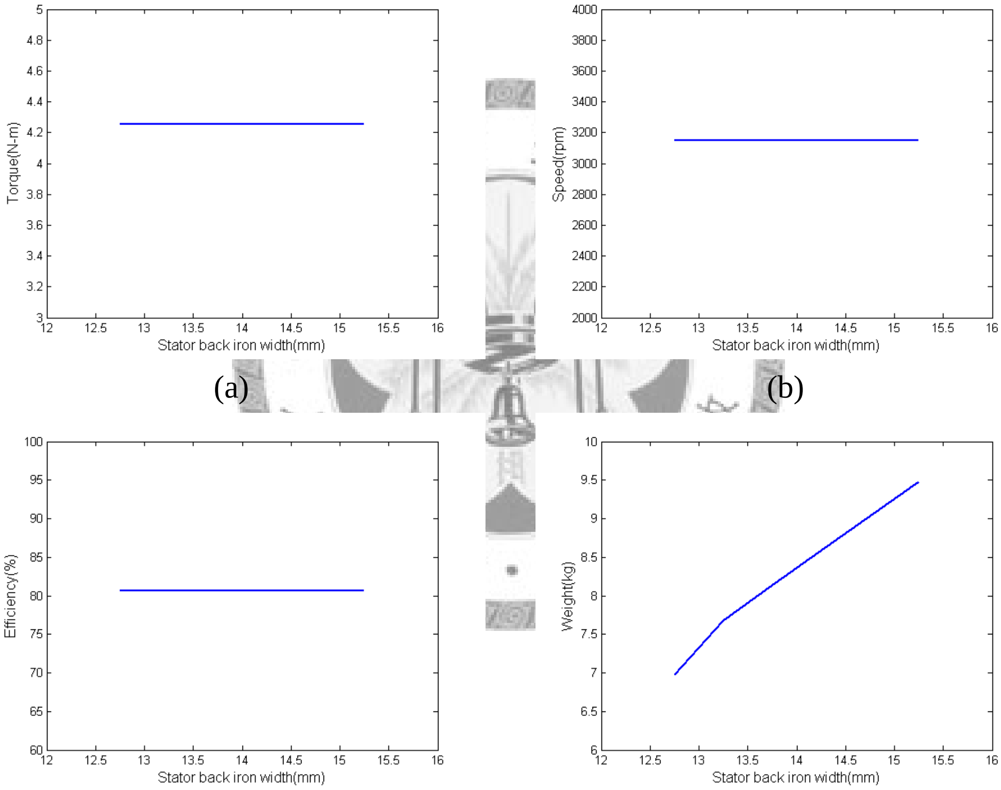

(a) (b)

(c) (d)

Fig. 4.27 Sensitivity of (a) Torque, (b) Speed, (c) Efficiency, and (d) Weight versus stator back iron width

(10) Air gap length g

The sensitivity of air gap length is shown in Fig. 4.28. The gap between the stator and the armature is defined as the air gap length, which is a primary region that provides electrical mechanical energy transformation and storage of magnetic energy. Therefore, the sensitivity of output torque with respect to the air gap length is high. Moreover, the increase in air gap length causes a large reluctance in the magnetic flux path; hence, the torque and efficiency are decreased by enlarging the air gap length.

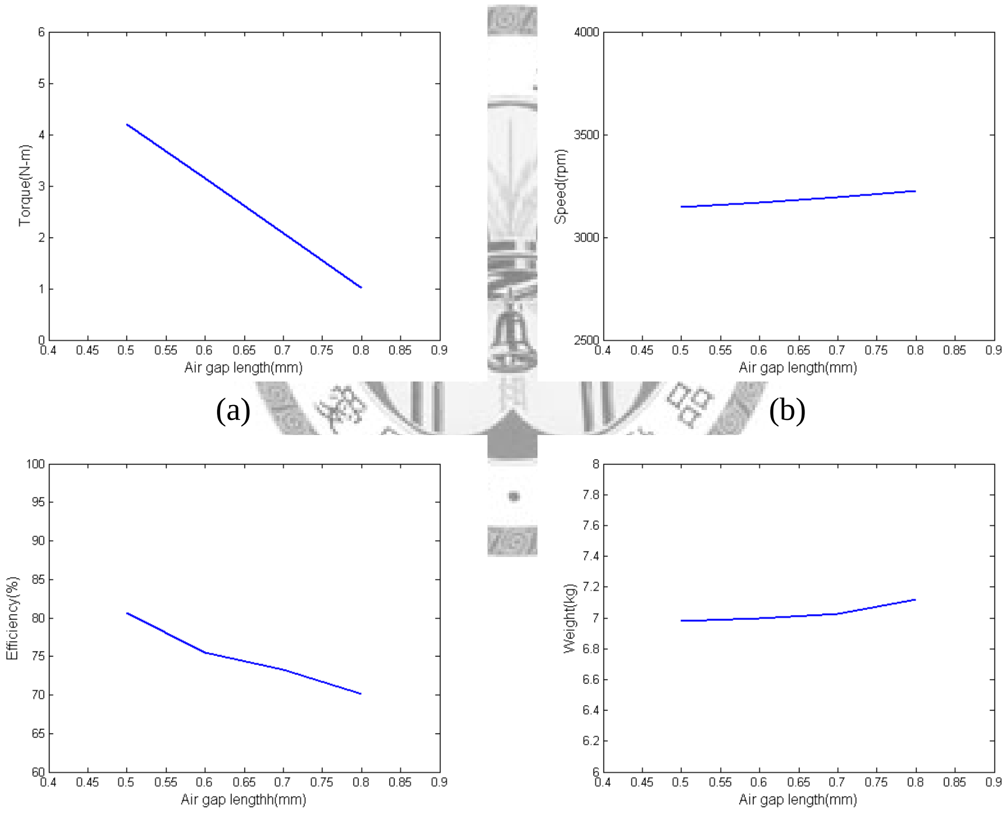

(a) (b)

(c) (d)

Fig. 4.28 Sensitivity of (a) Torque, (b) Speed, (c) Efficiency, and (d) Weight versus air gap length

(11) Motor axial length l

The sensitivity of motor axial length is shown in Fig. 4.29. Similar to the sensitivity of armature outer radius, the output torque is usually increased proportionally to the motor axial length. Increasing the axial length of a motor will also increase the use of materials. Therefore, the motor weight has a significant increase, which is proportionally to the axial length of the motor.

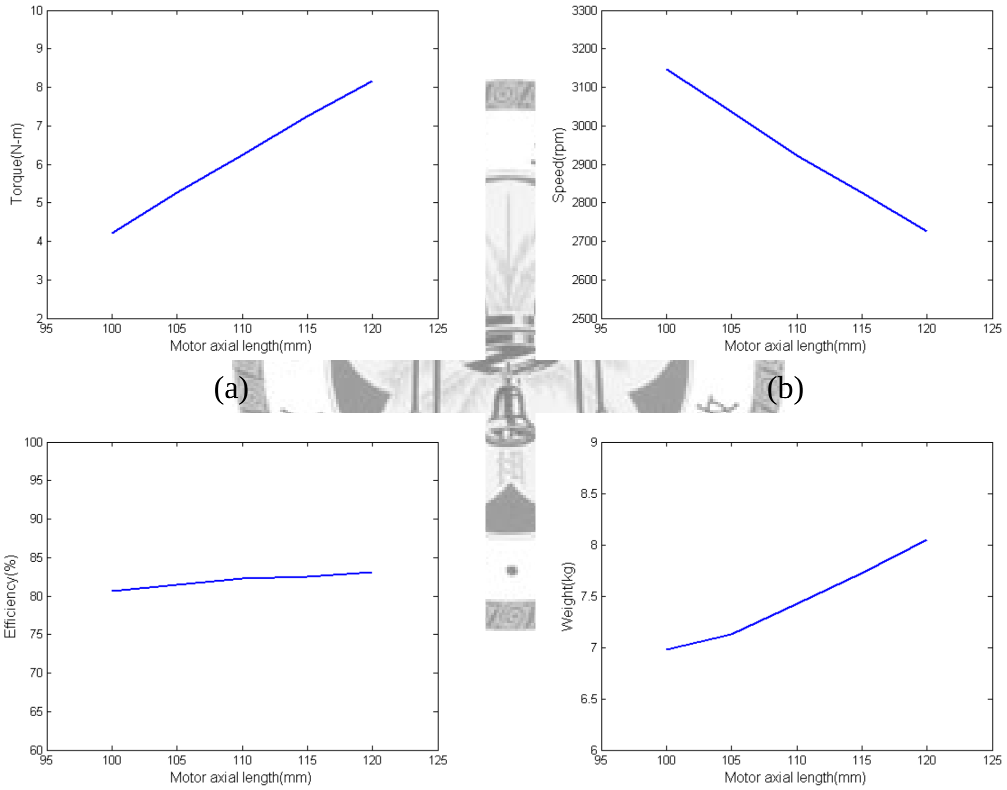

(a) (b)

(c) (d)

Fig. 4.29 Sensitivity of (a) Torque, (b) Speed, (c) Efficiency, and (d) Weight versus motor axial length

(12) Number of turns per armature slot N_a

The sensitivity of the number of turns per armature slot is shown in Fig. 4.30. The armature MMF is produced by conductors in the armature slots. If the number of turns per armature slot is increased, the armature MMF is also increased. Therefore, the torque increases with the increases in conductors per slot. The increases in conductors will consume more copper, and so the motor weight will also be increased. However, the increase in copper will also cause more copper losses; therefore, the efficiency will decrease substantially. The increase of conductors in the armature slots will increase the back EMF; therefore, the maximum speed of motor will decrease at an identical armature voltage.

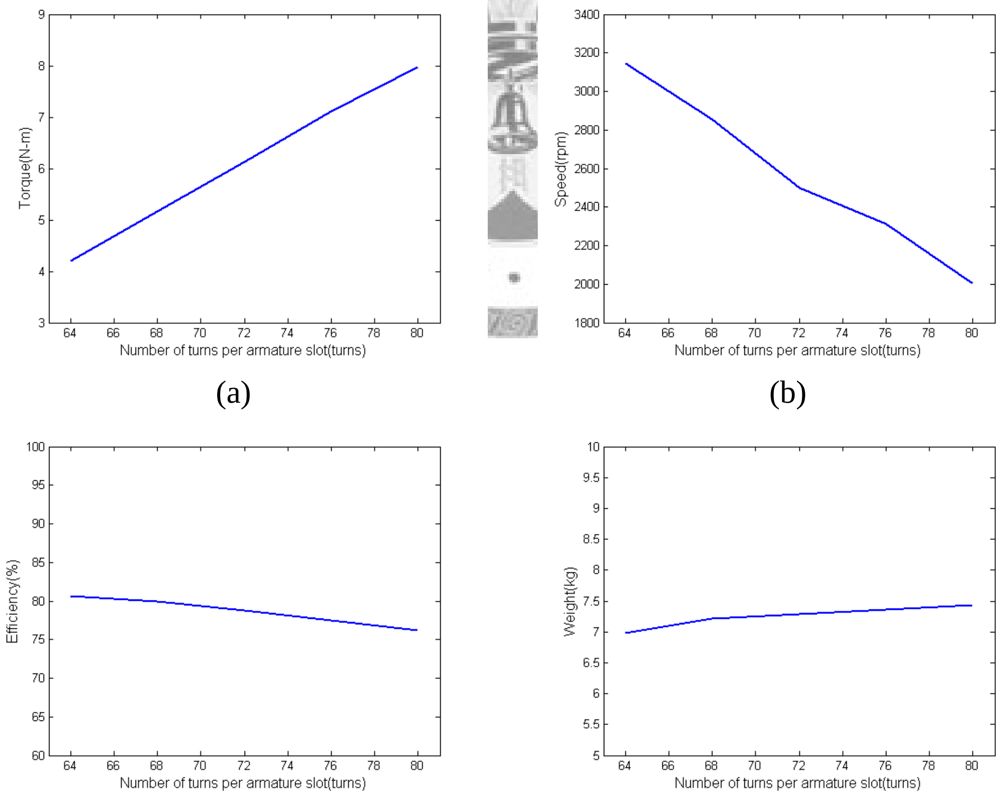

(a) (b)

(c) (d)

Fig. 4.30 Sensitivity of (a) Torque, (b) Speed, (c) Efficiency, and (d) Weight versus number of turns per armature slot

4.4.3 Sensitivity Indices

Sensitivity indices are defined as the ratio between the variation of an object function and the variation of a design variable, and are used for describing the influence of each objective function by each design variable per unit change [36]. This type of index helps designers to determine a proper set of design variables. The sensitivity indices for torque T, speed ω_{m}, efficiency η, and weight W_m are defined by $\Delta T/\Delta\phi$, $\Delta\omega_m/\Delta\phi$, $\Delta W_m/\Delta\phi$, and $\Delta\eta/\Delta\phi$ where ϕ symbolizes design variables. The sensitivity index of torque, speed, efficiency and weight are shown in Fig. 4.31, Fig. 4.32, Fig. 4.33, and Fig. 4.34 respectively.

According to these sensitivity indices, the tooth shoe depth d_1, the conductor slot depth d_2, and the half of the armature slot width w_{aa} have less sensitivity on the objective functions of torque and efficiency. Moreover, the armature back iron width d_a and the stator back iron width d_s have less sensitivity on the objective functions of torque, speed and efficiency. Hence, the influence of these five design variables is too small to be neglected in the optimal design process. Finally, seven design parameters are selected as design variables in the optimal design process; these are slot opening width o, magnet length l_m, magnet width τ_m, armature outer radius R_a, air gap length g, and number of turns per armature slot N_a.

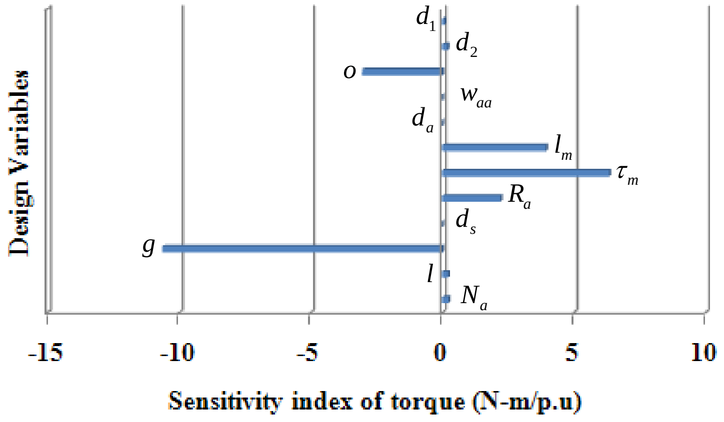

Fig. 4.31 Sensitivity index of torque

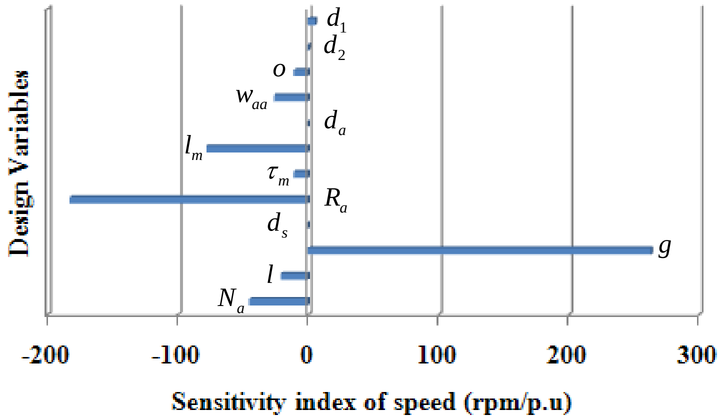

Fig. 4.32 Sensitivity index of speed

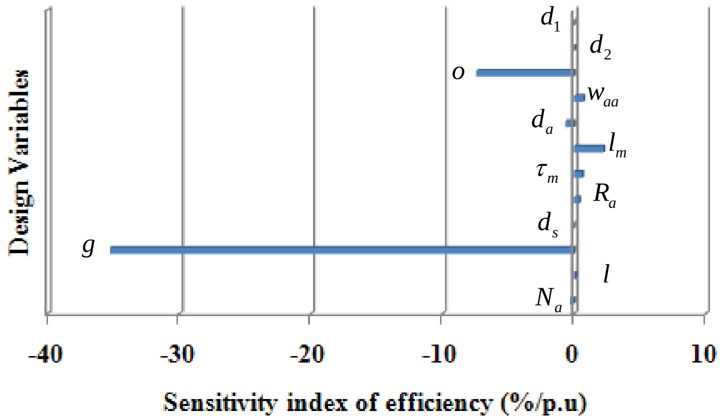

Fig. 4.33 Sensitivity index of efficiency

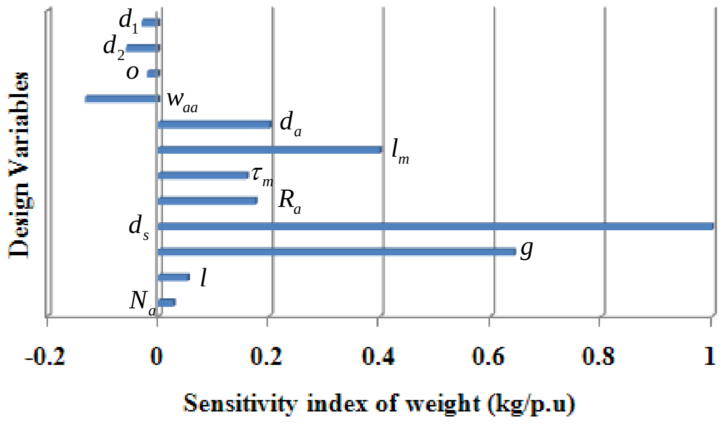

Fig. 4.34 Sensitivity index of weight

4.5 Optimal Design

4.5.1 The Optimal Design Tool

The optimal design utilized the multifunctional optimization system tool (MOST) [37], which is applied to deal with the multi-functional optimal design process. MOST is developed by the C++ language and a sequential quadratic programming (SQP) is selected as the single objective optimizer for the continuous variables. In addition, engineering design problems always involve a mix of continuous and discrete variables. As a result, a brand-to-bound method is developed to cope with discrete design variables. The MOST provides demonstrations with examples to help designers efficiently find the best solution for minimizing or maximizing the performance indices subject to the size and constraints [38] [39].

The purpose of optimization is to find a set of design variables in the feasible region, which gives a minimum value of the cost function. In the following discussion, two fundamental programming methods are introduced.

(1) Goal programming (GP) [40]

The goal programming is used to minimize the error between the optimal solution and the ideal solution in the objective function spaces. First, the errors, namely under-achievement and over-achievement of the i th objective function

$f_i(x)$, are defined as:

$$\begin{aligned} d_i^+ &= 0.5\{\left| f_i(x) - T_i^* \right| + (f_i(x) - T_i^*)\} \\ d_i^- &= 0.5\{\left| f_i(x) - T_i^* \right| - (f_i(x) - T_i^*)\} \end{aligned} \tag{4.82}$$

where T_i^* represents the goal set by the designer for the ideal solution in the i th objective function. Based on equation (4.82), the general formulation for optimal problems can be written as follows:

$$\min\ f(x) = \{\sum_{i=1}^{k} (d_i^+ + d_i^-)^p\}^{\frac{1}{p}},\ \ p \geq 1 \tag{4.83}$$

where p is determined by the designer according to the gradient of convergence.

(2) Compromise programming (CP) [41]

The compromising programming is used to minimize the distance between the optimal solution and the ideal solution. Unlike the goal programming, the distance, instead of the error, measured by the compromise programming is to evaluate how close the set of non-dominated points come to the ideal point with the cost function index L_q. The objective function $L_q(x)$ is defined as follows:

$$\min\ L_q(x) = \{\sum_{i=1}^{k} \alpha_i{}^p \left| \frac{f_i(x) - f_i^*}{f_{i,\max} - f_i^*} \right|^p\}^{\frac{1}{p}},\ \ p \geq 1 \tag{4.84}$$

where α_i are the weights, f_i^* and $f_{i,\max}$ are the optimal value and the worst values of the i th objective function, respectively. The $f_i(x)$ is the value of implementing the design variable x with respect to the ith objective. The subscript q represents the order of the cost function, which is defined by the designers.

In this thesis, the CP method is the candidate for the multi-functional optimal design process. Therefore, the optimization goal is to minimize the chosen cost function L_q. All of the design variables and objective functions are constructed by magnetic circuit models. The variation of each variable is based on the result of sensitivity analysis.

4.5.2 Optimal Design Process

After the sensitivity analysis, the critical design parameters are selected and further optimized. The objective of the optimization process is to accomplish the maximal output torque, the maximal speed, the minimal weight, and the maximal efficiency. The optimal design process in MOST is shown in Fig. 4.35.

First, an initial guess of design variables is given by the designer to evaluate the objective functions constructed in the optimizer. The initial values are then assigned in the magnetic circuit model and the gradients of objective functions and constraints are calculated. If any constraints are violated or the convergence test is not satisfied, the above steps have to be repeated until a final solution is obtained, which is the optimal design parameter. In MOST, different weightings of objective functions can be selected for optimization.

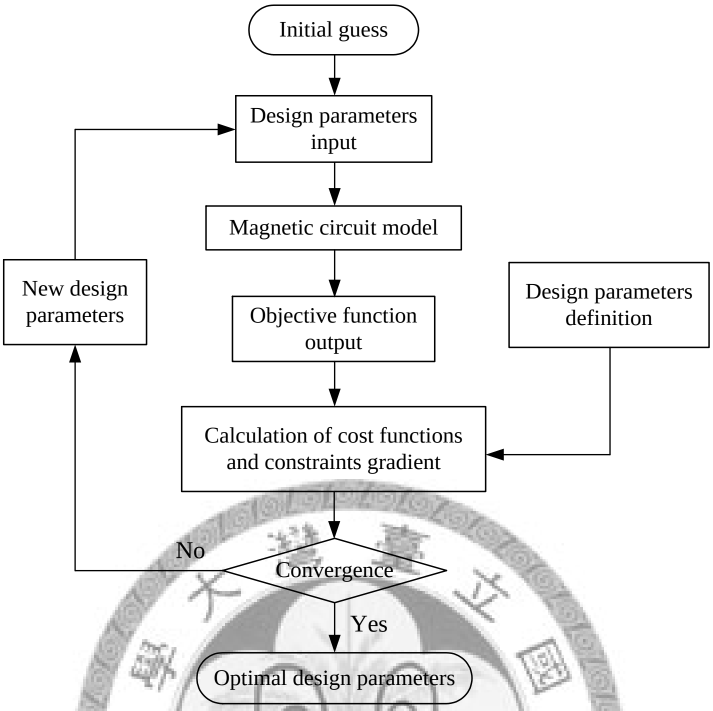

Fig. 4.35 Flowchart of optimal design process

The weighting of objective functions is assigned to be 3, individually, for fair comparison. The optimized variables based on different weighting of objective functions in group A are listed in Table 4.2. The best performance, or the least dimension, is considered to be the optimal solution. The results obtained from the group A can be discussed as follows:

(1) The optimization with weightings 1:1:1:1 for objective functions is the default value of MOST. By comparing to the initial design results, the values of weight seen to be better in the initial design, but the output torque and efficiency are worse

than for the initial design.

(2) The optimization with weightings 3:1:1:1 is the best among the other results due to better performance in the torque and speed. Moreover, it provides the second best efficiency and weight. Although the magnet width is larger than the initial design result, this is an acceptable trade-off. Therefore, this is considered to be the best among all of the results.

(3) The optimization with weightings 1:3:1:1 provides the second best speed, but its efficiency is worse than the initial design results. It seems to be inadequate due to its poor efficiency.

(4) The optimization with weightings 1:1:3:1 provides the second best torque, but its weight has no significant reduction compared with the original result. Therefore, it is not adopted.

(5) The optimization with weightings 1:1:1:3 provides the best efficiency, but the magnet width and weight are the largest among the results. It is not adopted because of the increased material costs it will incur.

Because the assigned weightings of objective functions have different combinations, the case of two selected objective functions can be further investigated. Two objective functions are selected from the four objective functions. The weighting of these selected objective functions is assigned to be 2, resulting in six different combinations. The optimized variables based on different weighting of objective functions in group B are listed in Table 4.3. The optimization with weightings 1:2:2:1 provides the best speed and the second best efficiency in group B. Because its torque performance and weight are in the middle level of other results, it is considered to be the best result in group B.

In conclusion, it seems that the result in group A with weighting 3:1:1:1 is the best for the specification requirements, and the resulting geometries are chosen for the finite element verification and fabrication. The optimization program is attached in Appendix B.

Table 4.2 Optimized variables of different weighting of objective functions (group A)

Variables	**Weighting (Torque: Speed: Weight: Efficiency)**					
	Initial	**1:1:1:1**	**3:1:1:1**	**1:3:1:1**	**1:1:3:1**	**1:1:1:3**
o (mm)	1	1.1	1.2	1.1	1.2	1.1
l_m (mm)	7	7.2	6.9	7.2	7.1	6.2
τ_m (mm)	44.26	43.8	48.4	49.2	50.5	51.2
R_a (mm)	40	38.9	41.2	40.2	40.3	39.8
g (mm)	0.5	0.51	0.48	0.52	0.5	0.5
l (mm)	100	98	100	99	99	102
N_a (turns)	64	60	64	64	60	64
Objective functions						
Torque (N-m)	4.2	4.15	4.68	4.21	4.54	4.49
Speed (rpm)	3147	3058	3245	3240	3142	3214
Efficiency (%)	80.7	78.6	81.2	80.3	80.6	82.5
Weight (kg)	6.98	6.72	6.83	7.25	6.92	7.42

Table 4.3 Optimized variables of different weighting of objective functions (group B)

Variables	**Weighting (Torque: Speed: Weight: Efficiency)**					
	2:2:1:1	**2:1:2:1**	**2:1:1:2**	**1:2:2:1**	**1:2:1:2**	**1:1:2:2**
o (mm)	1	1	1.1	1.1	1.2	1.2
l_m (mm)	7.1	7.2	7.2	7.3	7.1	7.2
τ_m (mm)	48.2	45.6	45.2	46.3	48.3	49.8
R_a (mm)	39.8	38.6	40.2	40.2	40.3	40.3
g (mm)	0.5	0.5	0.49	0.48	0.5	0.5
l (mm)	100	99	100	99	99	100
N_a (turns)	66	64	64	64	68	64
Objective functions						
Torque (N-m)	4.69	4.37	4.61	4.57	4.85	4.61
Speed (rpm)	3117	3122	3123	3246	3111	3122
Efficiency (%)	80.1	77.8	80.9	81.1	80.9	81.3
Weight (kg)	7.25	6.78	7.35	7.28	7.37	7.37

Chapter 5

Finite Element Verification

5.1 Introduction of Finite Element Analysis Tools

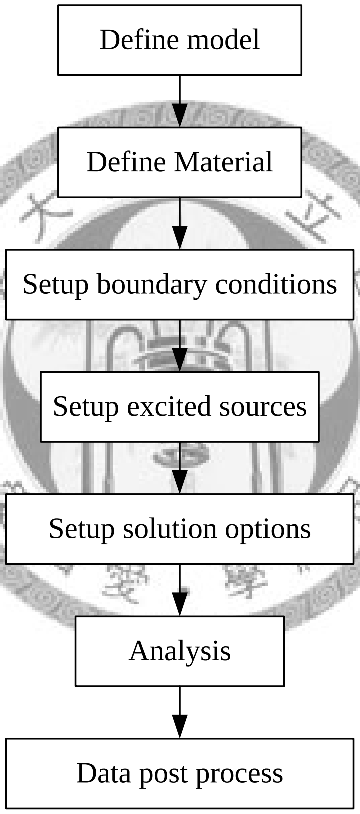

Fig. 5.1 Finite element analysis process flowchart

Although the linear magnetic circuit model was constructed in Chapter 4 to optimize the design variables, the nonlinear characteristics of material properties were not considered, such as the saturation of magnetic flux, the leakage flux between adjacent teeth and the operating temperature distribution. Commercial FE software for engineering problems provides effective analysis tools. Therefore, ANSOFT Maxwell 3D ver11.1 was selected for electromagnetic analysis and COSMOS Works was selected for thermal analysis. The analysis process using the commercial FE software is shown in Fig. 5.1.

5.2 The Flux Density Distribution in the Air Gap

In order to further investigate the flux density distribution, the 3D FEM tool is employed for analysis in this section. The FE model constructed in the ANSOFT Maxwell 3D ver11.1 is shown in Fig. 5.2. This model has six components: armature, armature winding, field winding, permanent magnet, stator and permeable material. After the model is constructed, the material for each component in the model needs to be assigned. The armature material is selected as steel 1008 because it is available in the ANSOFT Maxwell 3D material library and its material property is similar to AISI grade M19 lamination steel. The material of armature winding and field winding is copper. The stator and permeable material is low carbon steel S15C. The material of permanent magnet is ferrite magnet C3440. The detailed material information is listed in Appendix C.

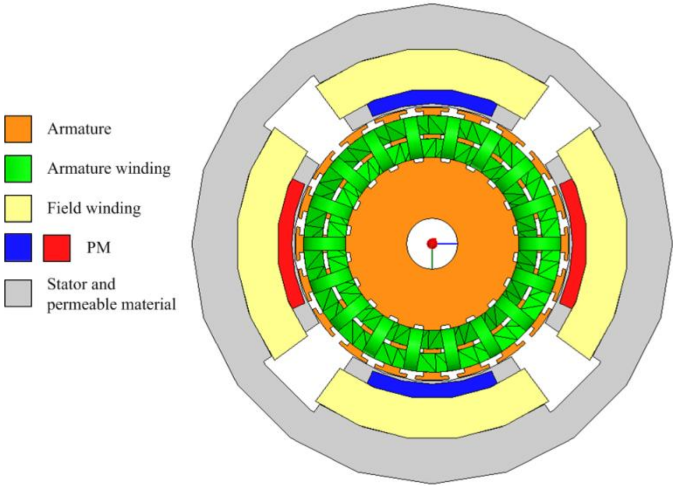

Fig. 5.2 ANSOFT Maxwell 3D FEA design model

The flux density distribution of the flux shunt DC motor is show in Fig. 5.3. According to the direction of flux density distribution, there are 4 closed magnetic loops formed by 4 poles and 20 armature slots. The presence of polarity N and polarity S poles can easily be seen in this figure. The maximum flux density of the stator happens on the lateral side of permeable pole face and is around 1.9T. The leakage flux occurs in the stator back iron and is around 0.4T. It should be noted that the flux resulting from the armature passing through the front permeable pole face is shunted to each lateral side of permeable pole face. Based on the simulation result, it can be inferred that the concept of flux shunt is validated in this design.

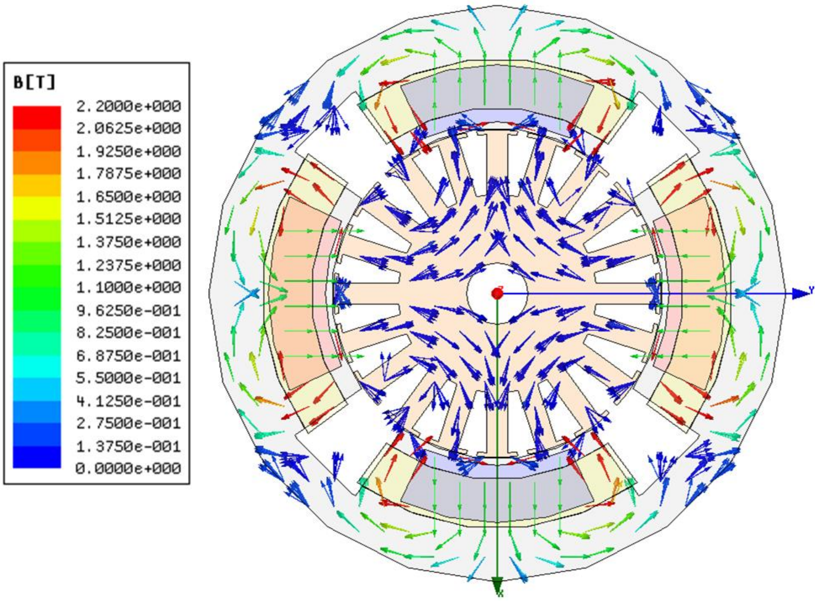

Fig. 5.3 Flux density distribution of the flux shunt DC (field current 10A)

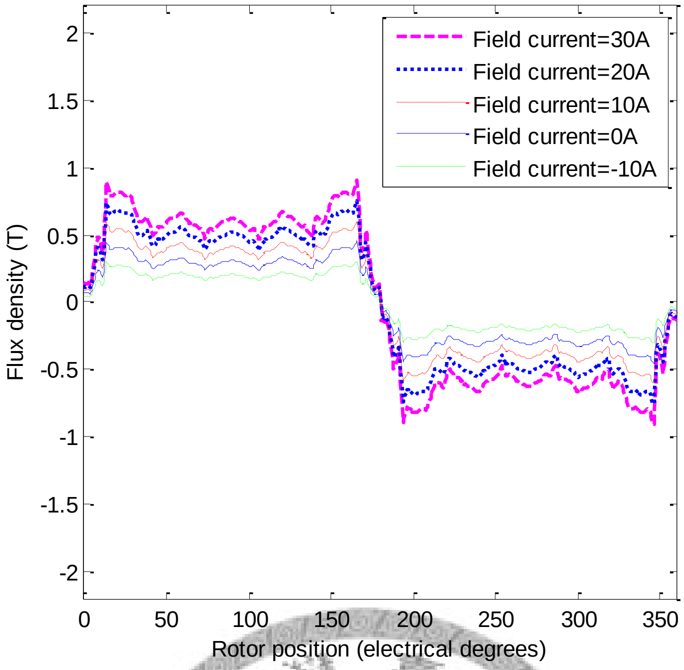

Fig. 5.4 Flux density distribution in the air gap (V_a=48V, i_a=10A)

The flux density distribution in the air gap is illustrated in Fig. 5.4. This figure shows the variation of flux density distribution in the air gap when field windings are excited by DC current with the following current values of 0, 10A, 20A, 30A and -10A. The field current value of 0A is in the original mode. The field current values of 10A, 20A and 30A are in the accumulative excited mode; the field current value of -10A is in the subtractive excited mode. Due to the use of a ferrite magnet, the air gap flux density is around 0.4T in the original mode. In the accumulative excited mode, the flux density is increased by the field excitation windings and the maximum flux density in the air gap is about 0.8T, while the field current is 30A. In contrast, the flux density is decreased by the field excitation windings in the subtractive excited mode and the minimum flux density in the air gap is about 0.2T, while the field current is -10A. The notches resulting from the armature slot effect influences the flux density waveform. Moreover, the flux density near the lateral permeable pole face becomes higher than that at the pole center due to the flux concentration.

According to the variation in flux density, it is clear that the flux field is controllable. The relationship between electric machine performance and field current will be further investigated in Chapter 6, with numerous experimental data.

5.3 Thermal Analysis

The purpose of thermal analysis is to investigate the stator temperature under the current excitation of field windings. Because the magnet is wound by the field winding, the magnet tends to be demagnetized when it is exposed to a high temperature environment, which reduces the motor performance. Therefore, the influence of the temperature should be carefully investigated during the design process.

Heat losses in the motor are results of the copper loss in coils and the core loss in the silicon steel. The source of copper loss is dominated by two components, copper loss from the armature windings and from the field windings. The copper loss can be estimated as [42]:

$$P_{copper} = R_c \left\{1 + \left[0.00393(T_c - 20)\right]\right\} i_c^2 \tag{5.1}$$

where P_{copper} is the copper loss (W) at coil temperature T_c, R_c is the coil resistance (Ω) at 20℃, T_c is the coil temperature (℃) and i_c is the coil current (A) at the coil temperature T_c. The core loss consists of two parts; the eddy current loss and the hysteresis loss. The core loss is related to the square of frequency of the alternative current in the silicon iron. The core loss characteristic can be obtained by reference to the datasheet provided by manufacturers. These data are inputted into COSMOS

Works for finite element thermal analysis. The boundary conditions set in the software are described as follows: ambient temperature is 25℃, heat convection coefficient is 25 W/m^2-K, heat sources are field windings, and quantity of heat is 100W. The thermal analysis simulates the condition of field windings fed by a 30A excitation current, which is the most severe operating condition. The stator thermal analysis model is shown in Fig. 5.5. In this model, the maximum stator temperature rises to about 75℃, which guarantees that the magnets will not suffer a demagnetization risk resulting from the heating of the field windings. This simulation result will be further verified by the temperature test, which is introduced in Chapter 6.

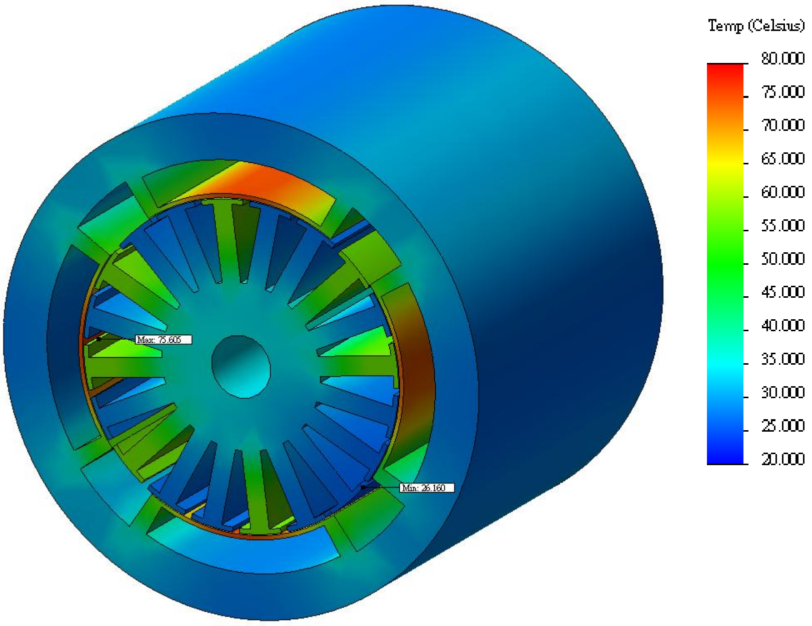

Fig. 5.5 Thermal analysis model (i_f=30A)

Chapter 6

Experiment and Discussion

6.1 Fabrication

The flux shunt DC motor has 20 slots on the armature, as shown in Fig. 6.1. The armature winding is wound by double-layer lap winding. These coils of two turns are bunched together before they are wound into the armature slots. The diameter of wire is selected as 0.75mm. The number of turns per coil is 16 and each slot contains two coils; therefore, each armature slot contains 64 conductors, as shown in Fig. 6.2. The commutator on the armature is in contact with a carbon brush set on the brush holder. The configuration of the carbon brush and brush holder unit is shown in Fig. 6.3.

Fig. 6.1 The armature of a flux shunt DC motor with armature winding

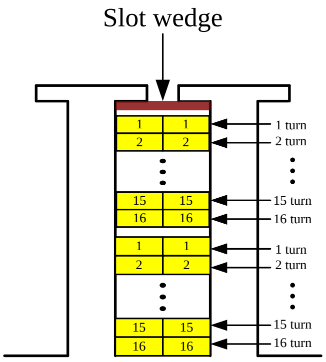

Fig. 6.2 The configuration of conductors in an armature slot

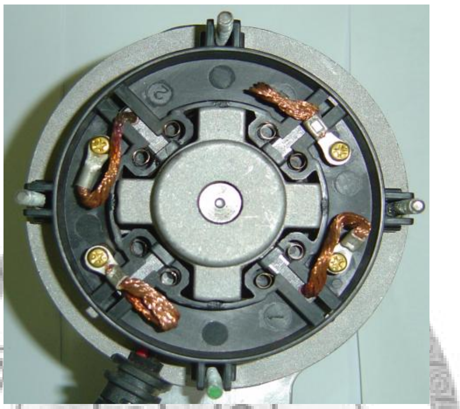

Fig. 6.3 The configuration of the carbon brush and brush holder unit

The flux shunt DC motor has four field poles on the stator; each field pole is wound by 10 turns of 1.5mm diameter wire as a field winding. The stator of the flux shunt DC motor with field winding is shown in Fig. 6.4.

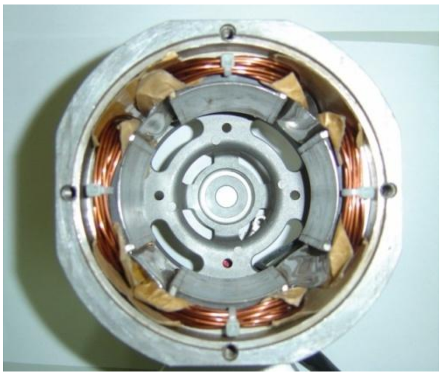

Fig. 6.4 The stator of flux shunt DC motor with field windings

After the winding process of the armature and the stator, these are assembled together to form a flux shunt DC motor. The assembly of the armature and stator is shown in Fig. 6.5. Finally, the front case and back case are fixed onto the stator, and the final flux shunt DC motor appears as shown in Fig. 6.6.

Fig. 6.5 The assembly of armature and stator

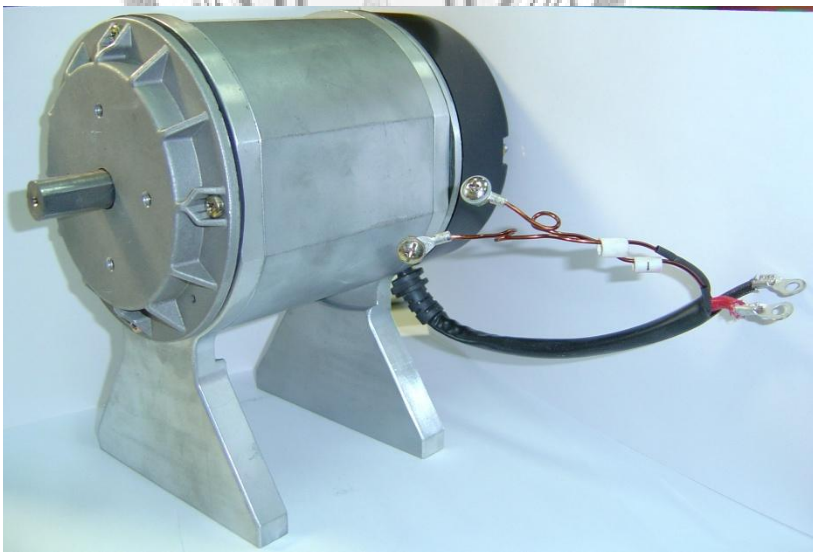

Fig. 6.6 The assembly of the flux shunt DC motor

6.2 Experimental Equipment

MAGTROL Motor test system [43]

HD-810 Hysteresis Dynamometer

5100 Power Analyzer

DSP6001 Dynamometer Controller

PC based motor testing program

Adjustable motor fixture

Fig. 6.7 HD-810 Hysteresis Dynamometer

(a) (b)

Fig. 6.8 (a) DSP6001 Dynamometer Controller [44], (b) 6530 Power Analyzer [45]

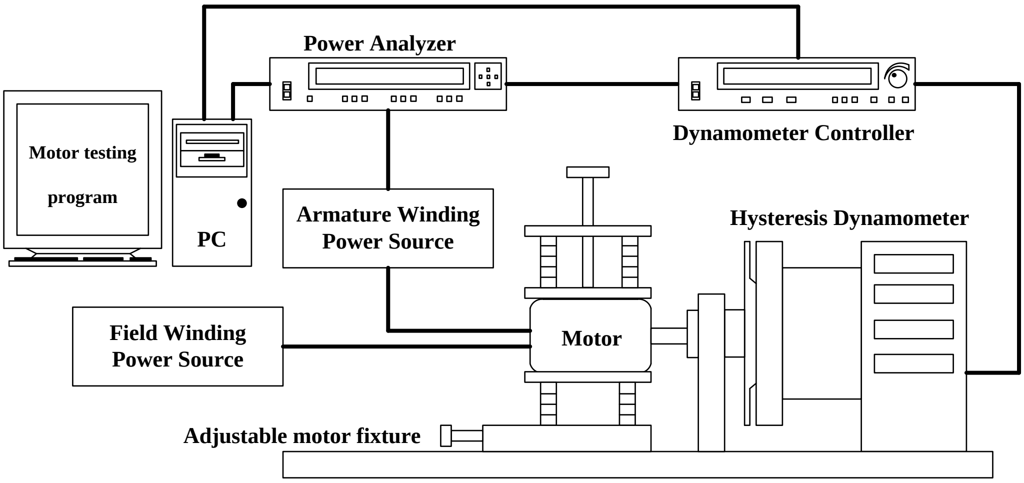

Fig. 6.9 Motor test system configuration

Power Supply

IDRC CD-2000:60V/100A/6kW;

GW Instek SPS-1230:12V/ 30A/360W;

Standard power supply: 50V/450A/22.5kW;

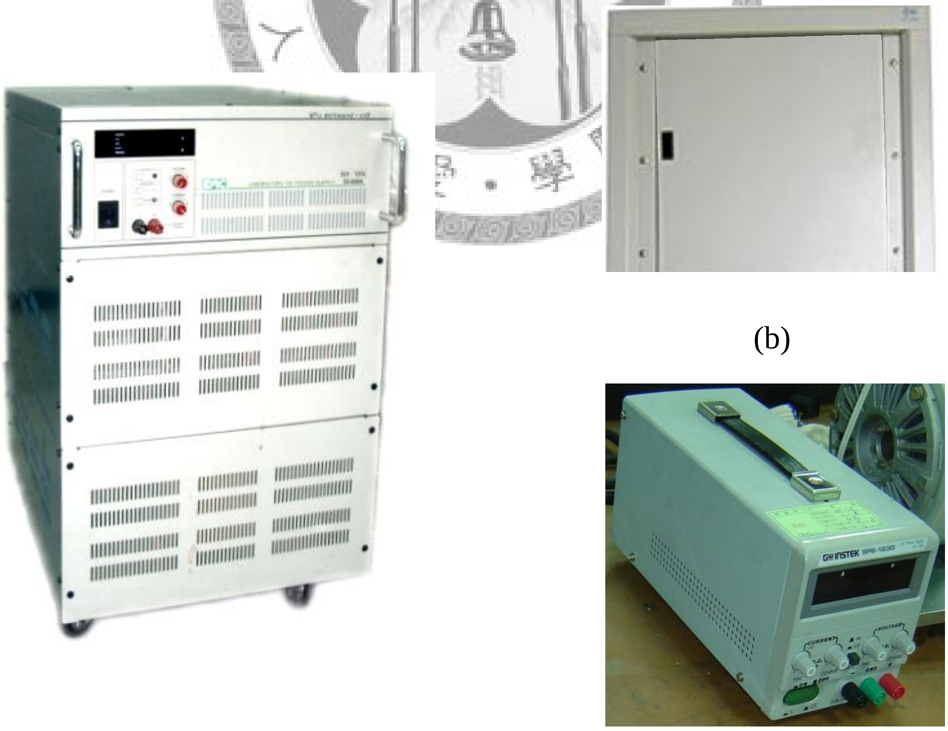

(b)

(a) (c)

Fig. 6.10 (a) IDRC CD-2000, (b) Standard power supply, (c) GW InstekSPS-1230

Oscilloscopes

Fig. 6.11 TDS 3014 Digital Phosphor Oscilloscopes

Other Instruments

Digital Multimeter: YFE YF-3140;

Clamp-on Power Meter: MIC 2080W;

Temperature gauge: CHY 506R Type: K/J/T/E/R/S/N;

(a) (b) (c)

Fig. 6.12 (a) Digital Multimeter, (b) Clamp-on Power Meter, (c) Temperature gauge.

6.3 Performance Test of the Flux Shunt DC motor

Experimental objective

In order to evaluate the torque capacity of the flux shunt DC motor with different armature current and field winding current, the torque versus armature current curve is measured. In addition, the torque versus speed curve of the flux shunt DC motor is measured with the armature voltage of 24V, 36V and 48V. In the corresponding armature voltage, the field winding current is fed by 10A, 20A, 30A, which are in the accumulative excitation mode; the field winding current is also fed by -10A, which is in the subtractive excitation mode. According to the experimental data generated, torque vs. speed curve, efficiency vs. speed curve, output power vs. speed curve, output power vs. torque curve, and efficiency vs. torque curve can be acquired. The machine performance in accumulative excitation mode and subtractive excitation mode is compared and evaluated.

Experimental procedure

1. Mount the motor on the adjustable motor fixture, as shown in Fig. 6.13.
2. The specific motor speed is set in the motor testing program for Windows-based data acquisition and the output torque will be recorded by the motor testing software. In the test process, armature winding current is fed by a standard power supply; field winding current is fed by a GW Instek SPS-1230 power supply.
3. Record the data displayed by the motor testing program.

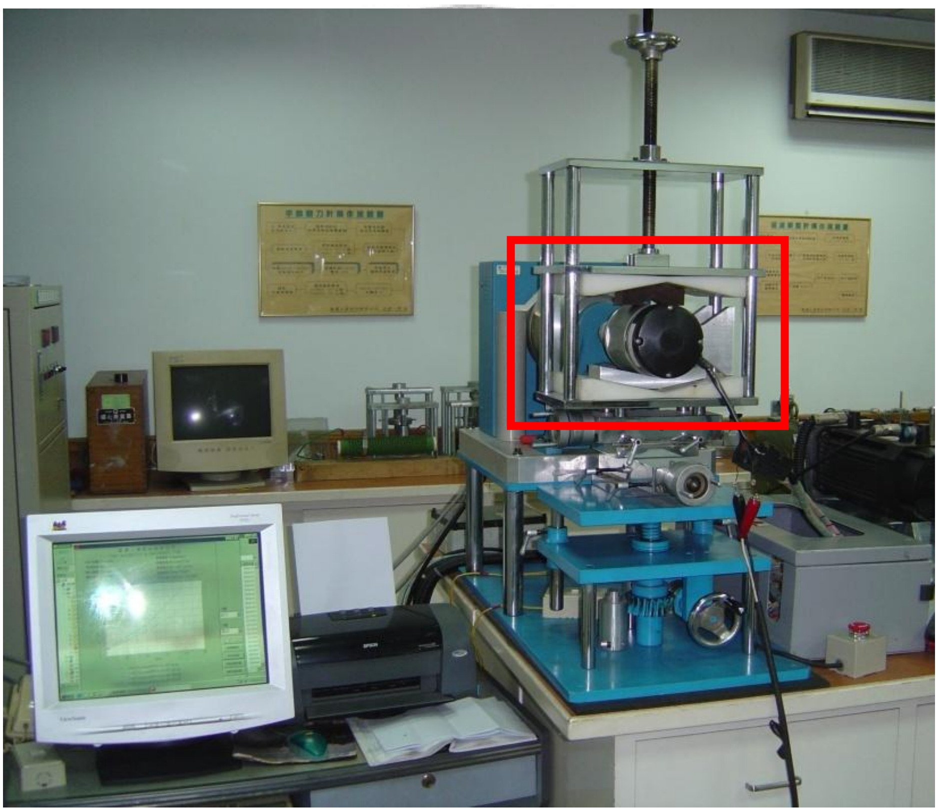

Fig. 6.13 Motor mounted on the motor test system

Experimental Results

The armature voltage is 24V

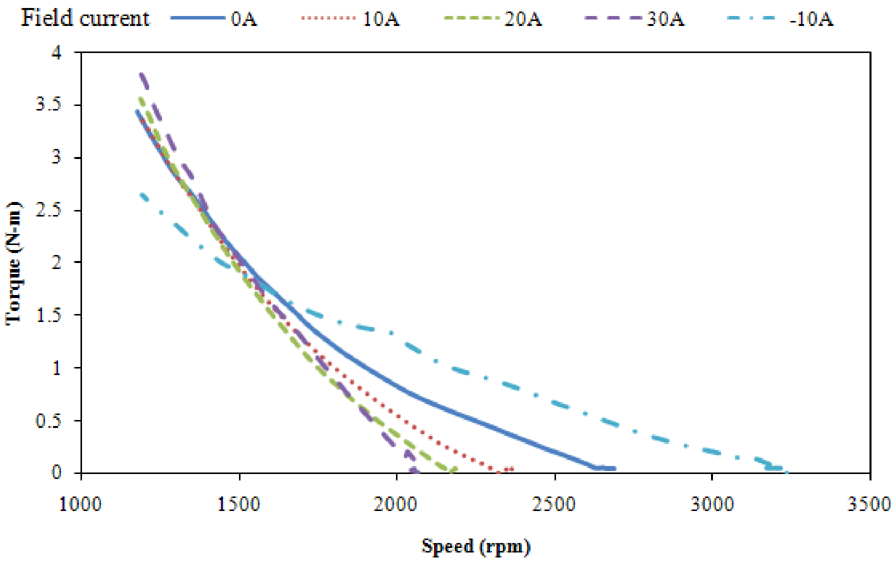

Fig. 6.14 Torque vs. Speed at 24V armature voltage

First, the armature voltage is supplied at 24V in this test. The motor’s field winding is fed by the current of 0A, 10A, 20A, 30A and -10A. The resulting torque vs. speed curve is shown in Fig. 6.14. The minimum speed is 1189 rpm when the field winding current is 30A. The maximum speed can reach as high as 3250 rpm when the field winding current is -10A. These four T-N curves intersect at the motor speed of about 1550 rpm, which is defined as the rated speed (base speed).When the motor speed exceeds the rated speed, the output torque drops with further increases in motor speed. This indicates that the motor has entered its constant power operation region. The constant power operation region can be extended by the field winding current, because the field flux is weakened in the subtractive excitation mode. This extension of the constant power operation region will also increase the maximum motor speed. In order to evaluate this behavior, the constant power speed ratio (CPSR) γ can be defined as follows [46]:

$$\gamma = \frac{\omega_{\max}}{\omega_{\text{rated}}} \tag{6.1}$$

where $\omega_{\max}$ is the maximum speed and ω_{rated} is the rated speed (base speed). In the case of 24V armature voltage, γ is calculated as $\frac{3250}{1550}$, yielding a value of 2.1.

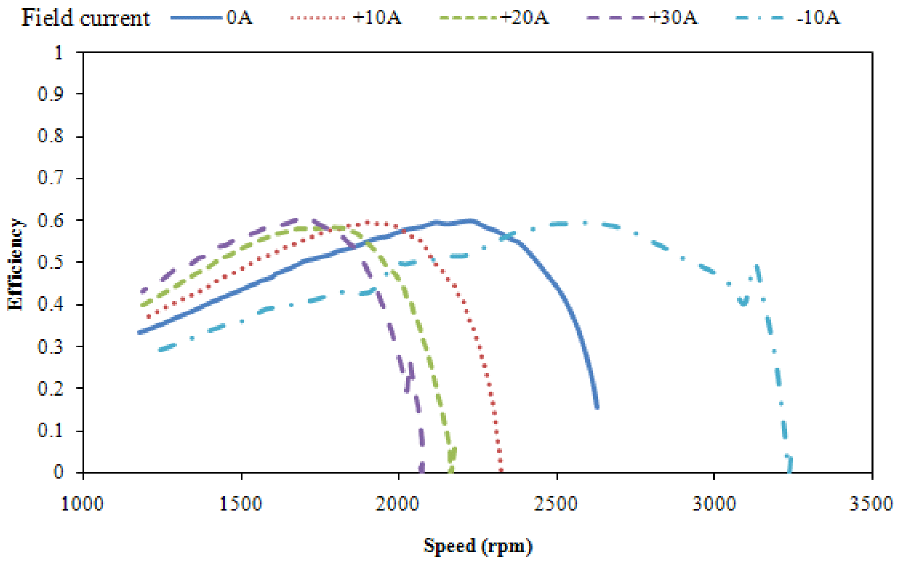

Fig. 6.15 Efficiency vs. Speed at 24V armature voltage

The resulting efficiency vs. speed curve is shown in Fig. 6.15. The maximum efficiency of the motor proposed in this thesis is 0.61 at 1694 rpm when the field winding current is 30A. The maximum efficiency is 0.6 at 2235 rpm when the field winding current is 0A. The maximum efficiency is 0.6 at 2515 rpm when the field winding current is -10A. According to the trend of the efficiency vs. speed curves, the maximum efficiency point is changed by different field winding currents. Although the maximum efficiency point in different field winding currents does not show a significant increase, the average efficiency below 1880 rpm is increased by positive field winding currents.

The efficiency of the motor is calculated by equation (6.2), which considers the losses resulting from field winding current and dynamometer as follows:

$$\eta = \frac{T\omega}{(V_a I_a + V_f I_f)\eta_{dyno}} \tag{6.2}$$

where T is the output torque (N-m), ω is the motor speed (rad/s), V_a and I_a are the input armature voltage and current, respectively; V_f and I_f are the input field winding voltage and current, respectively; The efficiency of the dynamometer is assumed to be 0.85. The power losses in the field winding excitation P_{fw} are calculated by the product of V_f and I_f, as listed in Table 6.1.

Table 6.1 The power losses in the field winding excitation

I_f	V_f	P_{fw}
10A	0.96V	9.6W
20A	2.31V	46.2W
30A	3.36V	100.8W

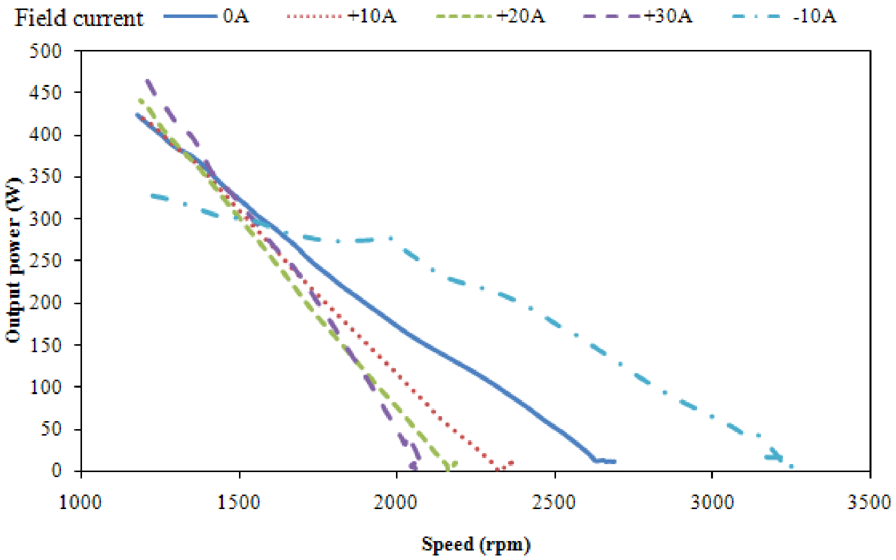

Fig. 6.16 Output power vs. Speed at 24V armature voltage

The resulting output power vs. speed curve is shown in Fig. 6.16. Because of the limitation of the armature current, the data of output power below 1100 rpm cannot be measured. It should be noted that the four curves intersect at the motor speed of 1550 rpm and then the output power drops immediately. The motor speed is extended to approximately 3250 rpm because the field flux is weakened by a field current of -10A.

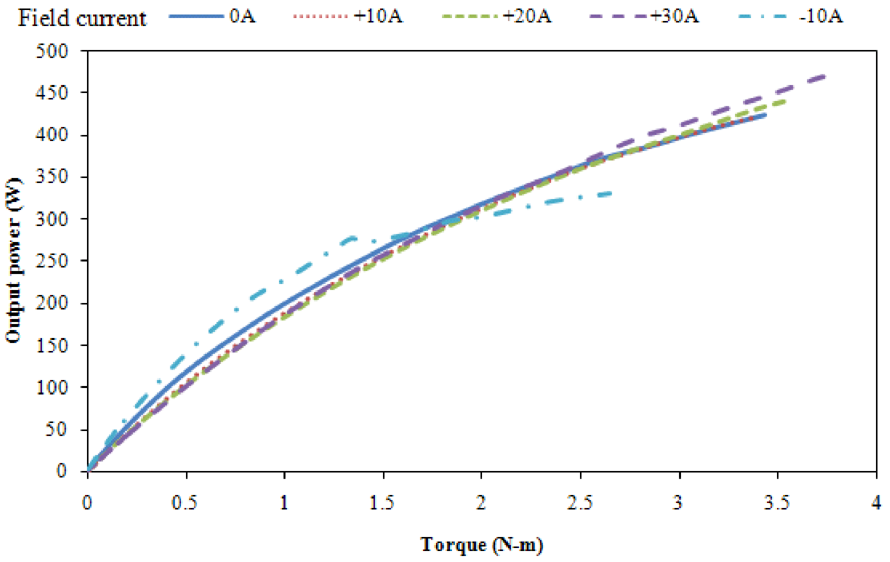

Fig. 6.17 Output power vs. Torque at 24V armature voltage

The resulting output power vs. torque curve is shown in Fig. 6.17. The field winding current has no significant influence on the output power.

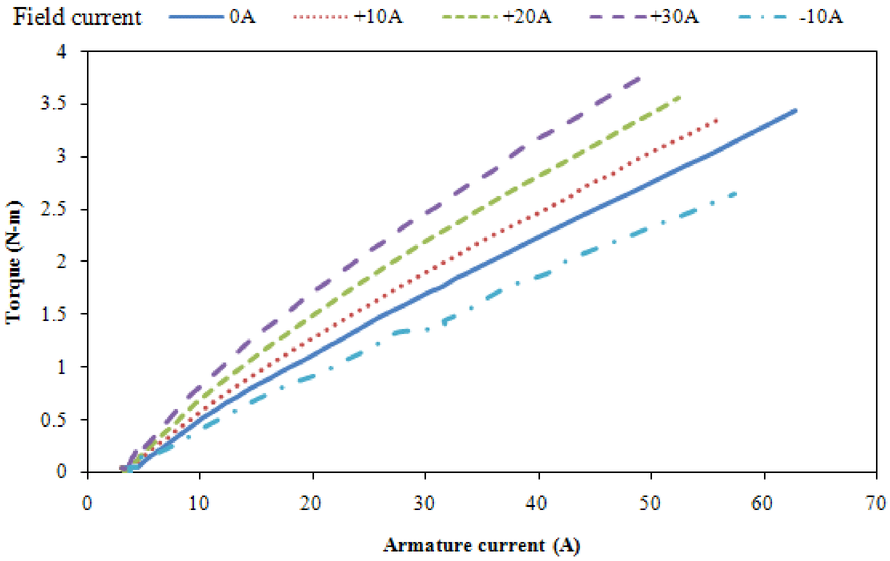

Fig. 6.18 Torque vs. Armature current at 24V armature voltage

The resulting torque vs. armature current curve is shown in Fig. 6.18. It indicates that the torque can be increased by the field winding current and the relationship between torque and armature current presents is positive and proportional. Therefore, it can be represented by linear equations of different field winding currents. The linear equations obtained by curve fitting are shown as follows:

$$T = 0.0587 i_a - 0.1348 \quad (\text{field current} = 0\text{A}) \tag{6.3}$$

$$T = 0.0656 i_a - 0.1428 \quad (\text{field current} = 10\text{A}) \tag{6.4}$$

$$T = 0.0752 i_a - 0.1647 \quad (\text{field current} = 20\text{A}) \tag{6.5}$$

$$T = 0.0855 i_a - 0.1919 \quad (\text{field current} = 30\text{A}) \tag{6.6}$$

$$T = 0.0497 i_a - 0.1258 \quad (\text{field current} = -10\text{A}) \tag{6.7}$$

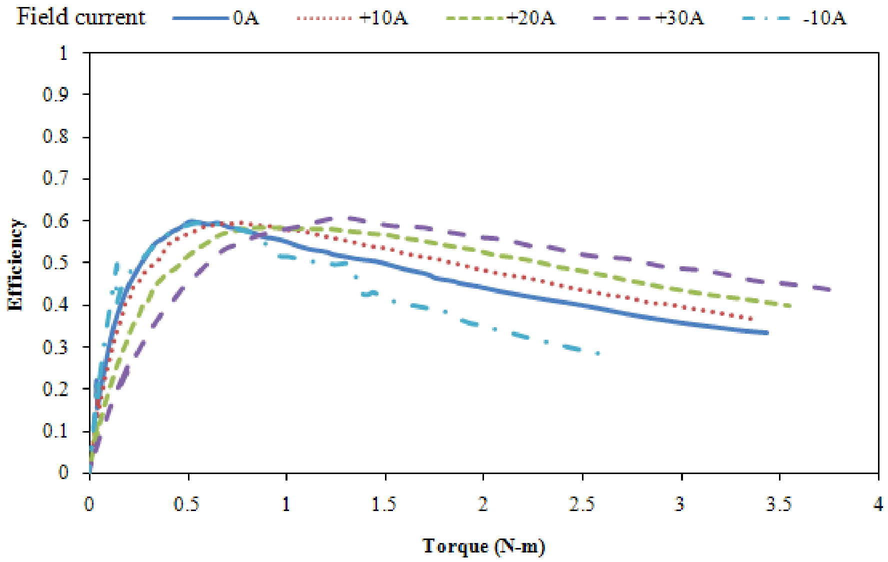

Fig. 6.19 Efficiency vs. Torque at 24V armature voltage

The resulting efficiency vs. torque curve is shown in Fig. 6.19. The maximum efficiency of the motor is 0.61 at 1.3 N-m when the field winding current is 30A. The maximum efficiency is 0.6 at 0.66 N-m when the field winding current is 0A. According to the trend of efficiency vs. torque curve, the motor efficiency at an identical torque can be increased by a positive field winding current but is decreased by a negative field winding current.

The armature voltage is 36V

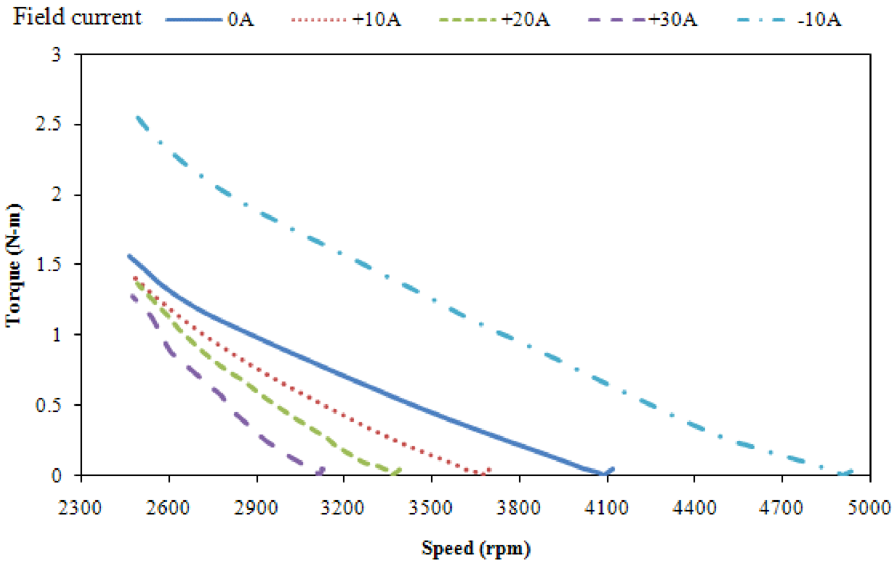

Fig. 6.20 Torque vs. Speed at 36V armature voltage

Second, the armature voltage is supplied at 36V in this test. The motor's field winding is fed by the current of 0A, 10A, 20A, 30A or -10A. The resulting torque vs. speed curve is shown in Fig. 6.20. The rated speed of the motor is 2480 rpm. The maximum speed can reach as high as 4932 rpm when the field winding current is -10A. This validates that the field flux provided by the permanent magnet is weakened by the field winding, resulting a significant maximum speed extension. In the case of 36V armature voltage, the γ is calculated by $\frac{4932}{2480}$, to yield a value of 1.99.

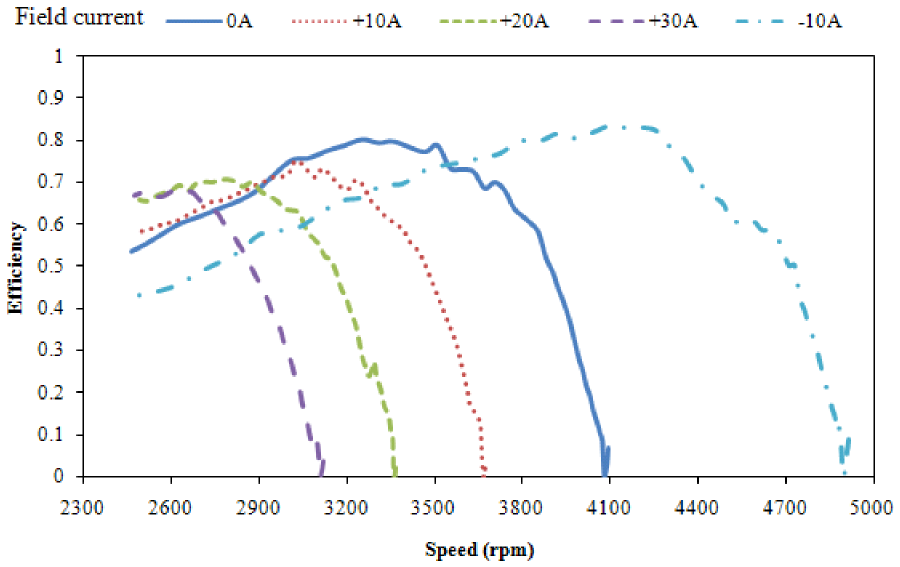

Fig. 6.21 Efficiency vs. Speed at 36V armature voltage

The resulting efficiency vs. speed curve is shown in Fig. 6.21. The maximum efficiency of the motor is 0.68 at 2507 rpm when the field winding current is 30A. The maximum efficiency is 0.80 at 3251 rpm when the field winding current is 0A. The maximum efficiency is 0.84 at 4103 rpm when the field winding current is -10A. According to the trend of the efficiency vs. speed curves, the maximum efficiency point is changed by different field winding currents. Although the maximum efficiency point in different field winding currents does not show a significant increase, the average efficiency below 3000 rpm is increased by a positive field winding current.

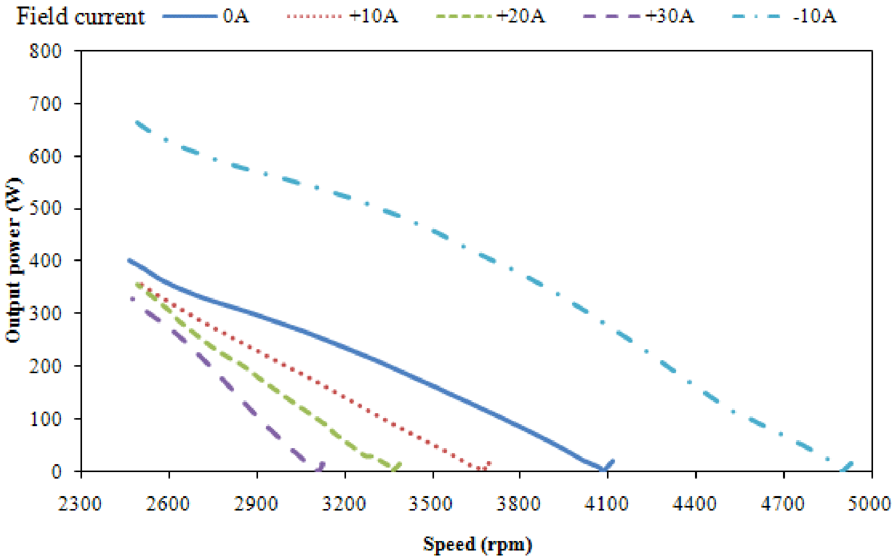

Fig. 6.22 Output power vs. Speed at 36V armature voltage

The resulting output power vs. speed curves are shown in Fig. 6.22. Because of the limitation of armature current, the output power below 2500 rpm cannot be measured. It should be noted that there are three curves of field current 0A, 10A, 20A and 30A that intersect at the motor speed of 2463 rpm and then the output power drops immediately. The motor speed is extended around 5000 rpm because the field flux is weakened by the field current of -10A.

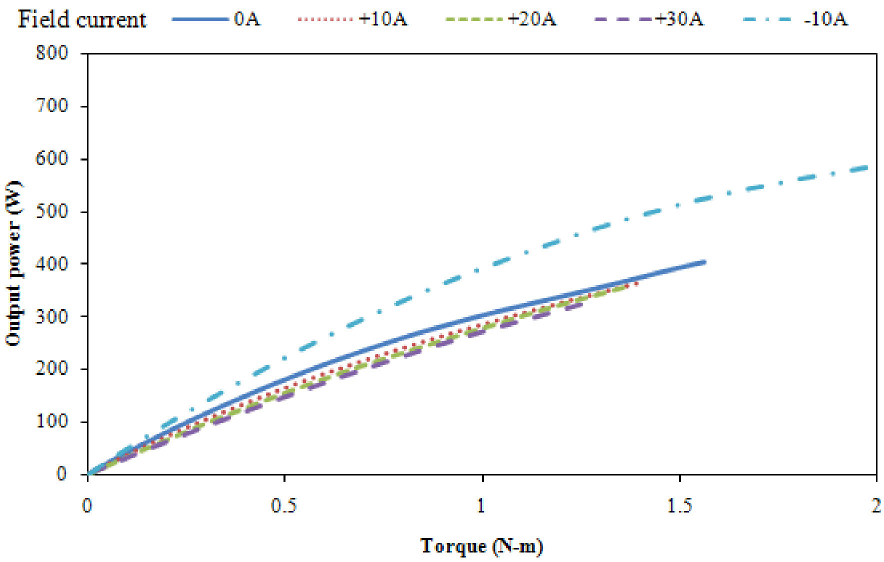

Fig. 6.23 Output power vs. Torque at 36V armature voltage

The resulting output power vs. torque curve is shown in Fig. 6.23. It indicates that the field winding currents have no significant influence on the output power.

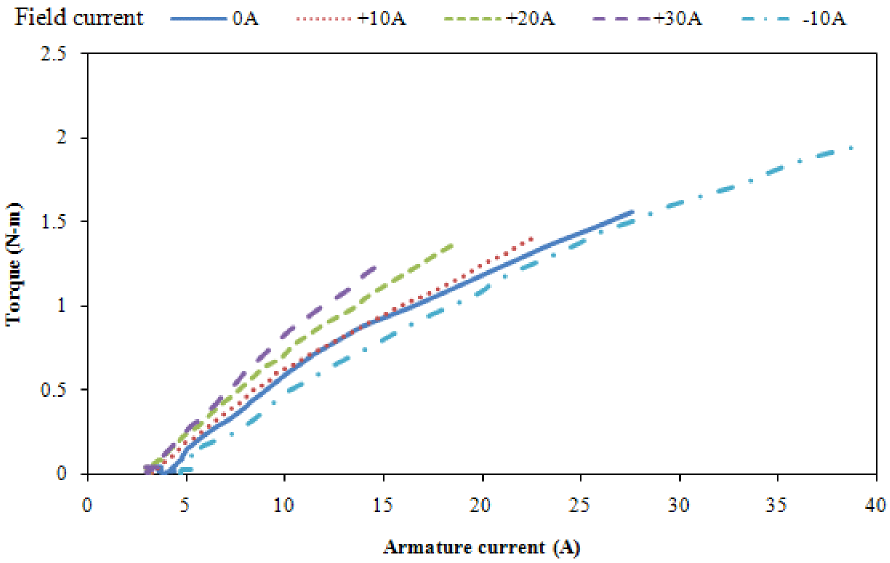

Fig. 6.24 Torque vs. Armature current at 36V armature voltage

The resulting torque vs. armature curve is shown in Fig. 6.24. It indicates that the torque can be increased by the field winding current and the relationship between torque and armature current presents a positive proportional relationship; therefore, the linear equations obtained by curve fitting are as follows:

$$T = 0.0699 i_a - 0.209 \quad (\text{field current} = 0\text{A}) \tag{6.8}$$

$$T = 0.0738 i_a - 0.1863 \quad (\text{field current} = 10\text{A}) \tag{6.9}$$

$$T = 0.0913 i_a - 0.2419 \quad (\text{field current} = 20\text{A}) \tag{6.10}$$

$$T = 0.1095 i_a - 0.3081 \quad (\text{field current} = 30\text{A}) \tag{6.11}$$

$$T = 0.0605 i_a - 0.1996 \quad (\text{field current} = -10\text{A}) \tag{6.12}$$

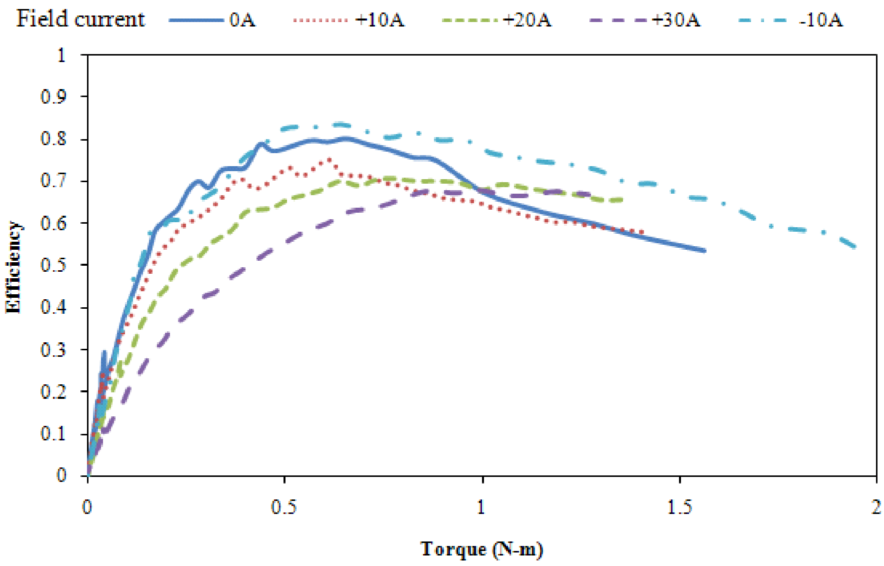

Fig. 6.25 Efficiency vs. Torque at 36V armature voltage

The resulting efficiency vs. torque curve is shown in Fig. 6.25. The maximum efficiency of the motor is 0.68 at 1.19 N-m when the field winding current is 30A.

The maximum efficiency is 0.8 at 0.65 N-m when the field winding current is 0A.

The armature voltage is 48V

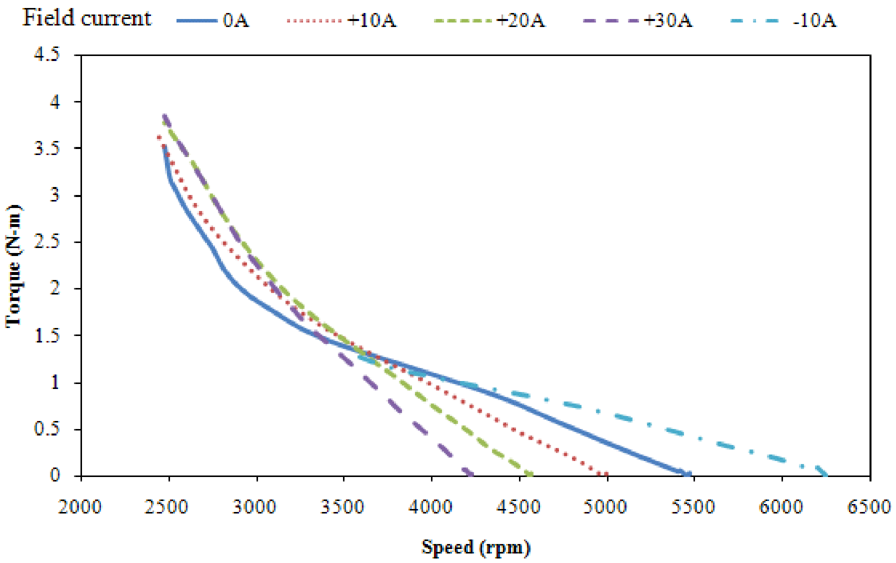

Fig. 6.26 Torque vs. Speed at 48V armature voltage

Third, the armature voltage is supplied at 48V in this test. The motor’s field winding is fed by the current of 0A, 10A, 20A, 30A or -10A. The resulting torque vs. speed curve is shown in Fig. 6.26. The rated speed of the motor is 3350 rpm. The maximum speed can reach as high as 6242 rpm when the field winding current is -10A. The field flux provided by the permanent magnet is weakened by the field winding, resulting in a significant maximum speed extension. In the case of 48V armature voltage, the γ is calculated by $\frac{6242}{3350}$, yielding a value of 1.86.

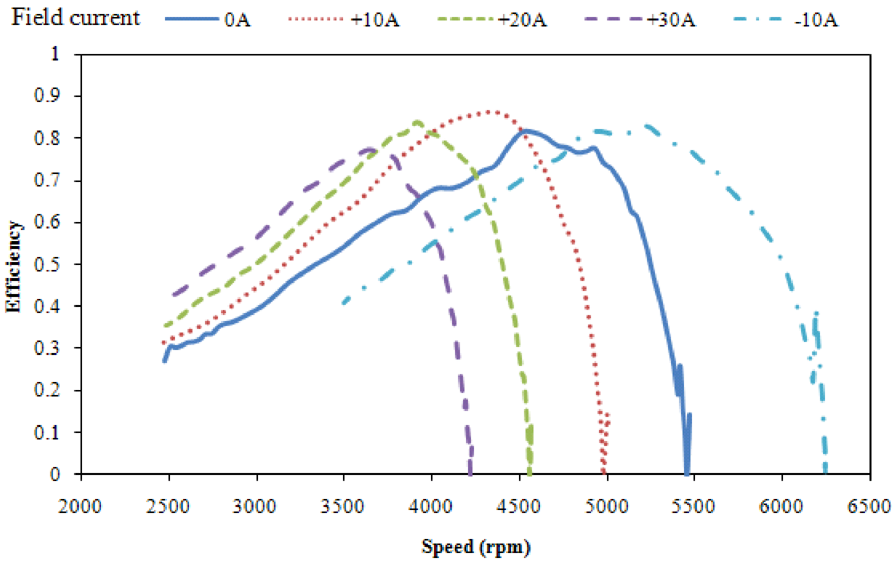

Fig. 6.27 Efficiency vs. Speed at 48V armature voltage

The resulting efficiency vs. speed curve is shown in Fig. 6.27. The maximum efficiency of the motor is 0.77 at 3635 rpm when the field winding current is 30A. The maximum efficiency is 0.81 at 4583 rpm when the field winding current is 0A. The maximum efficiency is 0.83 at 5221 rpm when the field winding current is -10A. According to the trend of the efficiency vs. speed curve, the maximum efficiency point is changed by different field winding currents. Although the maximum efficiency point in the different field winding currents does not show a significant increase, the average efficiency below 3692 rpm is increased by a positive field winding current.

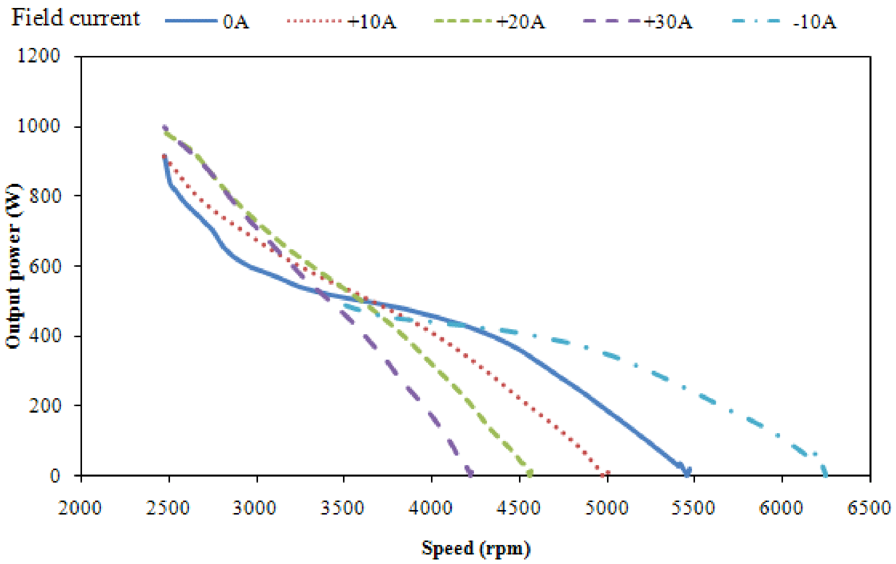

Fig. 6.28 Output power vs. Speed at 48V armature voltage

The resulting output power vs. speed curve is shown in Fig. 6.28. Because of the limitation of the armature current, the output power below 2477 rpm cannot be measured. There are four curves for field current 0A, 10A, 20A and 30A that intersect at the motor speed of 3274 rpm and the output power then drops immediately. The motor speed is extended around 6200 rpm because the field flux is weakened by a field current of -10A.

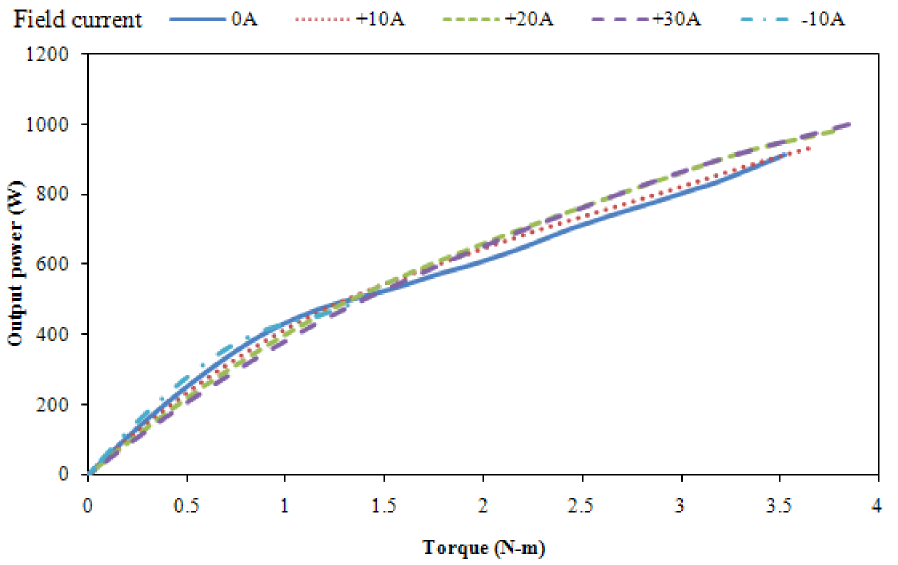

Fig. 6.29 Output power vs. Torque at 48V armature voltage

The resulting output power vs. torque curve is shown in Fig. 6.29. The field winding currents have no significant influence on the output power.

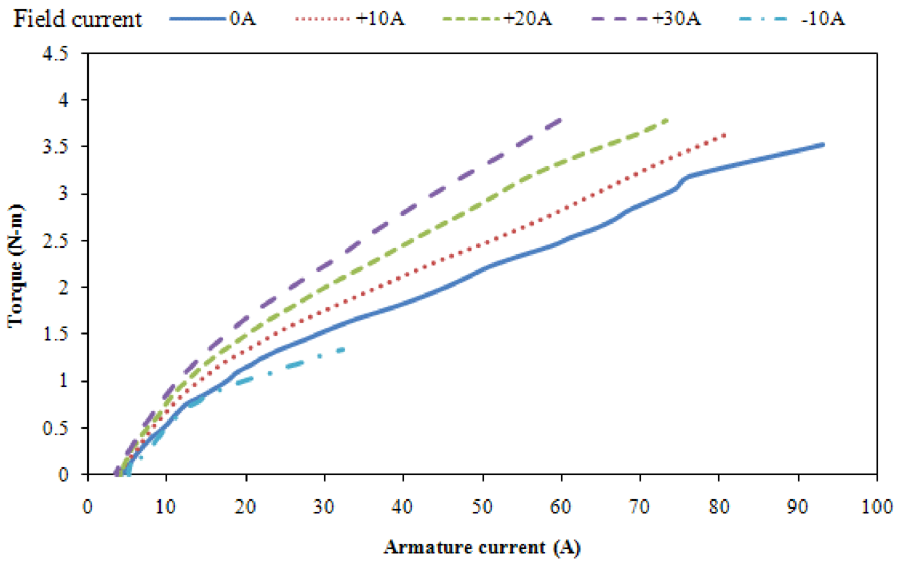

Fig. 6.30 Torque vs. Armature current at 48V armature voltage

The resulting torque vs. armature current curve is shown in Fig. 6.30. It indicates that the torque can be increased by the field winding current and the relationship between torque and armature current is positive and proportional. Therefore, the linear equations obtained by curve fitting can be shown as follows:

$$T = 0.0432 i_a - 0.0122 \quad (\text{field current} = 0\text{A}) \tag{6.13}$$

$$T = 0.0491 i_a - 0.0175 \quad (\text{field current} = 10\text{A}) \tag{6.14}$$

$$T = 0.0591 i_a - 0.0714 \quad (\text{field current} = 20\text{A}) \tag{6.15}$$

$$T = 0.0717 i_a - 0.1062 \quad (\text{field current} = 30\text{A}) \tag{6.16}$$

$$T = 0.0564 i_a - 0.1917 \quad (\text{field current} = -10\text{A}) \tag{6.17}$$

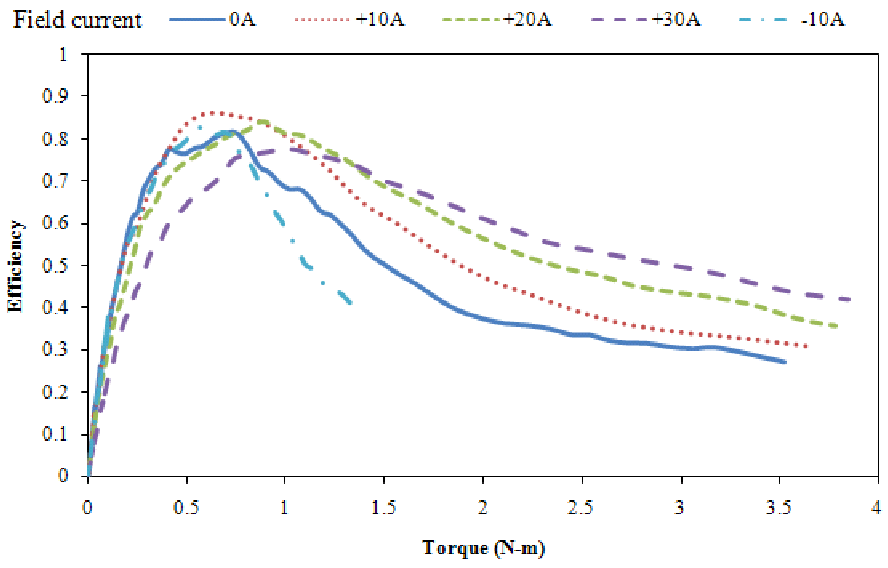

Fig. 6.31 Efficiency vs. Torque at 48V armature voltage

The resulting efficiency vs. torque curve is shown in Fig. 6.31. The maximum efficiency of the motor is 0.77 at 1.024 N-m when the field winding current is 30A.

The maximum efficiency is 0.81 at 0.69 N-m when the field winding current is 0A. According to the trend of efficiency vs. torque curve, the motor efficiency at an identical torque can be increased by a positive field winding current but is decreased by a negative field winding current.

6.4 Temperature Test

Experimental objective

Because a field winding is wound around the permanent magnet for current excitation, the temperature rise of the field winding has a great influence on the permanent magnet. In order to evaluate whether the heat loss from the field winding will cause irreversible demagnetization, a temperature test was implemented.

Experimental procedure

1. Maintain the motor operating in the no load condition with a 48V armature voltage.
2. The field winding current 10A, 20A, or 30A is fed by the IDRC CD-2000 power supply in that order and each is maintained for 30 minutes.
3. Record the field winding temperature of each field pole with a temperature gauge every minute, as shown in Fig. 6.32.

Fig. 6.32 The temperature measurement of the field winding

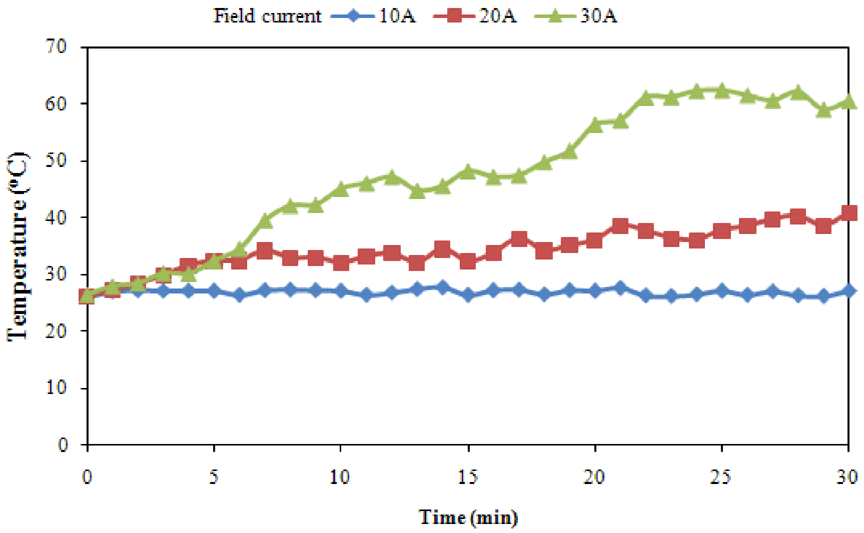

Fig. 6.33 The rising field winding current curve with different field currents

The rising field winding current curve with different field currents is shown in Fig. 6.33. The field winding temperature in the condition of field current 10A showed no significant rise. The field winding temperature in the condition of field current 20A was slightly increased; it reached about 40℃ after the 20th minute. It should be noted that the field winding temperature reaches its maximum 65℃ after the 22nd minute while the field current is 30A. It is assumed that the temperature of the magnets is very close to the temperature of the field winding. If the *B-H* curve of grade C3440 ferrite magnet at 60℃ shown in Appendix C is consulted, it can be found that a knee point for that *B-H* curve does not exist. According to the results of temperature test, it can be concluded that irreversible demagnetization of the proposed machine is not a risk and does not occur in the no load condition, if the field excitation current is maintained under 30A.

6.5 Measurement of Back EMF Waveform

Experimental objective

In order to evaluate the effect of anti-demagnetization, the back EMF waveform of the flux shunt DC motor is measured. In addition, the back EMF waveform of a permanent magnet (PM) DC motor which has no flux shunt magnet circuit is also measured for a comparative study.

Experimental procedure

1. Maintain the motor operating at the constant speed of 3000rpm.

2. Measure the armature winding back EMF waveform of flux shunt DC motor and permanent magnet (PM) DC motor by oscilloscopes and save data before demagnetization.

3. Lock the armature of the flux shunt DC motor and fed armature current 40A for 3 second. The permanent magnet of flux shunt DC motor is demagnetized in this step.

4. Lock the armature of the PM DC motor and fed armature current 40A for 3 second. The permanent magnet of PM DC motor is demagnetized in this step.

5. Measure the armature winding back EMF waveform of flux shunt DC motor and PM DC motor by oscilloscopes and save data after demagnetization.

Experimental Results

The measured back EMF of flux shunt DC motor before and after demagnetization is shown in Fig. 6.34. The back EMF of the motor is 15.69V before demagnetization. The back EMF of the motor is 15.59V after demagnetization. The back EMF value is reduced because of demagnetization. The decrease rate of back EMF is calculated as $\frac{|15.59-15.69|}{15.69}\times\frac{100}{100}$, yielding a value of 0.64%.

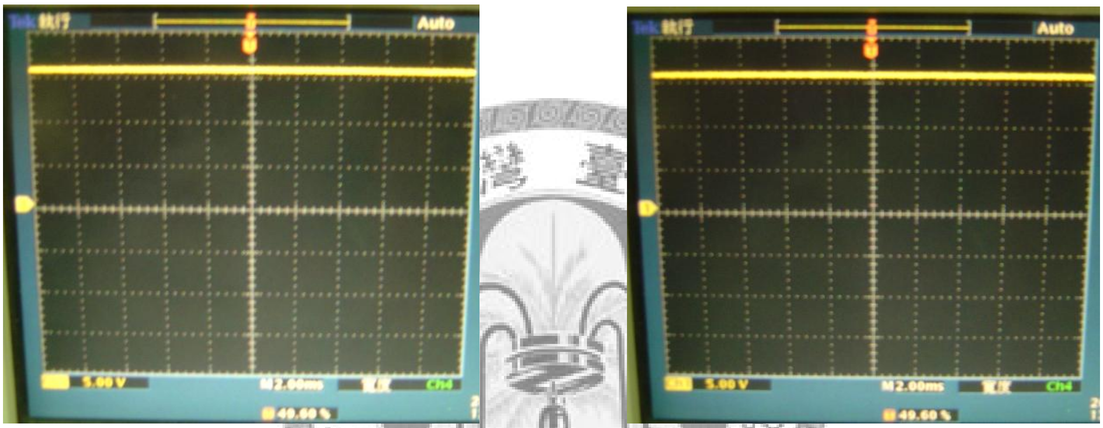

(a) (b)

Fig. 6.34 Comparison of the measured back EMF of flux shunt DC motor
(a) before demagnetization and (b) after demagnetization

The measured back EMF of PM DC motor before and after demagnetization is shown in Fig. 6.35. The back EMF of the motor is 14.23V before demagnetization. The back EMF value is reduced because of demagnetization. The back EMF of the motor is 14.05V after demagnetization. The decrease rate of back EMF is calculated as $\frac{|14.23-14.05|}{14.23}\times\frac{100}{100}$, yielding a value of 1.3%.

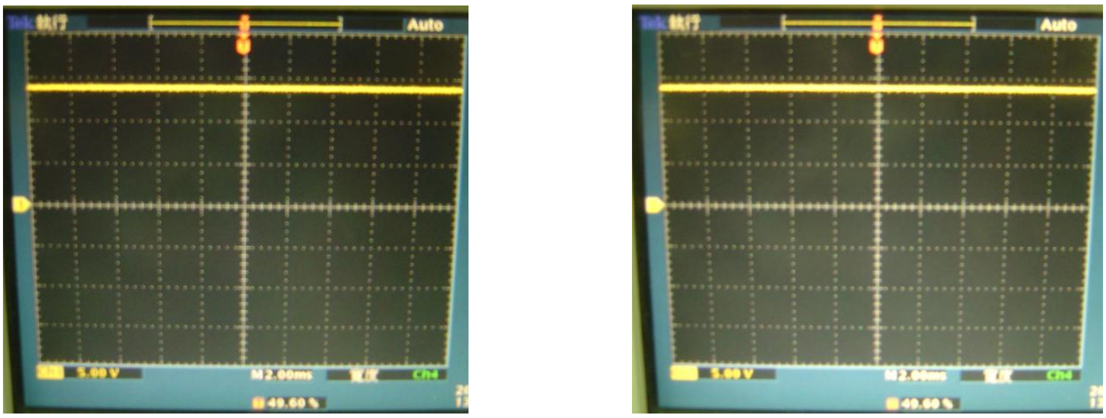

(a) (b)

Fig. 6.35 Comparison of the measured back EMF of PM DC motor (a) before demagnetization and (b) after demagnetization

The results of measured back EMF is listed in Table 6.2 for comparative study. Because the decrease rates of back EMF of flux shunt DC motor is lower than PM DC motor, it indicates that flux shunt DC motor has an advantage in anti-demagnetization.

Table 6.2 The comparison of back EMF value

	Flux shunt DC motor	**PM DC motor**
Before demagnetization	15.69V	14.23V
After demagnetization	15.59V	14.05V
Decrease rates of back EMF	0.64%	1.3%

Chapter 7

Conclusions

7.1 Conclusions

The conceptual design of a flux shunt DC motor with anti-demagnetization mechanism is developed in this thesis to resolve the disadvantages of permanent magnet machines. The design process, analytical magnetic circuit model, sensitivity analysis, optimal design, finite element analysis, fabrication, and experimental study of the prototype have been presented. The design parameters of the machine and the criteria for material selection are demonstrated in the design process. The analytical magnetic circuit model for the flux shunt DC motor was constructed as a function of the armature shift that was defined as the relative angle between the armature and the stator. A multi-functional optimization tool is applied in the optimal design process. The concept of flux shunt has been validated by a finite element electromagnetic analysis tool. Finite element thermal analysis has been carried out to confirm any irreversible demagnetization problems of the permanent magnet. A temperature test suggests that the highest temperature of the motor should not exceed 70℃ under the maximum field winding excitation current kept for 30 minutes. It can be concluded that an irreversible demagnetization problem does not rise from the field winding. Experimental results in a motor performance test indicate that the torque performance and efficiency of the proposed machine can be increased by the use of auxiliary field windings in the accumulative excitation mode, while the armature voltage is maintained at a constant value. The maximum speed of the machine can be extended by the auxiliary field windings in the subtractive excitation mode at constant armature voltage. This control technique of speed extension can be referred to as the flux weakening control technique used in permanent magnet synchronous machines. The field flux control ability in a permanent magnet DC machine can be implemented without complex electronic power elements. Therefore, the designed flux shunt DC motor is an interesting alternative for the situations that demand high speed variations, such as wind generators, electric vehicles, or electric tools.

7.2 Contributions

The main contribution of the research is the development of a novel class of DC motors and a method to design and optimize this type of motor. Specifically, the contributions can be summarized as follows:

1. The conceptual design of the flux shunt DC motor is presented.
2. The design parameters of the flux shunt DC motor topology are defined.
3. The operating principle, field flux distribution, and motor performances are investigated in this study.
4. The magnetic circuit model for the flux shunt DC motor is constructed.
5. The sensitivity analysis is executed to investigate the design parameters.
6. An optimization process of the proposed motor is demonstrated in this study.
7. The prototype of the flux shunt DC motor is fabricated.
8. The performance test of the prototype is evaluated by experimental measurements.

7.3 Future Work

Although the prototype of a flux shunt DC motor has been designed, fabricated and tested, there are several suggestions provided for the future work and further investigation.

1. Because of the limitations of available experimental devices, the measurement of the stator flux density distribution could not be executed. If a flux measurement device is available, the relationship between the stator flux distribution and the field winding current could be further investigated.
2. According to the performance results, the armature speed is varied with different field winding currents, while the armature voltage is kept constant. Therefore, the armature speed can change continuously by proper control of the field winding current. The flux shunt DC motor may therefore have applications to those situations that demand high speed variations or continuously variable transmission. The measured motor parameters are provided in Appendix D for control utilization.
3. The commutator and carbon brush unit equipped in this prototype is selected from those commercially available. There is little literature that has investigated the design of commutators and carbon brushes. It is suggested that the design of commutators and carbon brushes can be further studied.

References

[1] F. Odor and A. Mohr, "Two-component magnets for DC motors," *Magnetics, IEEE Transactions on*, vol. 13, pp. 1161-1162, 1977.

[2] A. H. Isfahani, S. Vaez-Zadeh, and M. A. Rahman, "Using modular poles for shape optimization of flux density distribution in permanent-magnet Machines," *Magnetics, IEEE Transactions on*, vol. 44, pp. 2009-2015, 2008.

[3] K. M. Rahman, N. R. Patel, T. G. Ward, J. M. Nagashima, F. Caricchi, and F. Crescimbini, "Application of direct-drive wheel motor for fuel cell electric and hybrid electric vehicle propulsion system," *Industry Applications, IEEE Transactions on*, vol. 42, pp. 1185-1192, 2006.

[4] Y. P. Yang, Y. P. Luh, and C. H. Cheung, "Design and control of axial-flux brushless DC wheel motors for electric vehicles-part I: multiobjective optimal design and analysis," *Magnetics, IEEE Transactions on*, vol. 40, pp. 1873-1882, 2004.

[5] Y. P. Yang, J. P. Wang, S. W. Wu, and Y. P. Luh, "Design and control of axial-flux brushless DC wheel motors for electric vehicles-part II: optimal current waveforms and performance test," *Magnetics, IEEE Transactions on*, vol. 40, pp. 1883-1891, 2004.

[6] Y. f. Liao, F. Liang, and T. A. Lipo, "A novel permanent magnet motor with doubly salient structure," *Industry Applications, IEEE Transactions on*, vol. 31, pp. 1069-1078, 1995.

[7] H. Wei, C. Ming, Z. Q. Zhu, W. X. Zhao, and X. G. Kong, "Comparison of electromagnetic performance of brushless motors having magnets in stator and rotor," in *Proceedings of the 52nd Annual Conference on Magnetism and Magnetic Materials*, Tampa, Florida (USA), 2008, pp. 07F124-3.

[8] C. Yu, K. T. Chau, X. Liu, and J. Z. Jiang, "A flux-mnemonic permanent magnet brushless motor for electric vehicles," in *Proceedings of the 52nd Annual Conference on Magnetism and Magnetic Materials*, Tampa, Florida (USA), 2008, pp. 07F103-3.

[9] V. Ostovic, "Memory motors-a new class of controllable flux PM machines for a true wide speed operation," in *Industry Applications Conference Thirty-Sixth IAS Annual Meeting. Conference Record of the 2001 IEEE*, vol.4, pp. 2577-2584.

[10] R. P. Deodhar, S. Andersson, I. Boldea, and T. J. E. Miller, "The flux-reversal machine: a new brushless doubly-salient permanent-magnet machine," *Industry Applications, IEEE Transactions on*, vol. 33, pp. 925-934, 1997.

[11] M. Topor, Y.-D. Chun, D.-H. Koo, P.-W. Han, B.-C. Woo, and I. Boldea, "Application of flux reversal principle for axial flux permanent magnet machines," in *Proceedings of the 52nd Annual Conference on Magnetism and Magnetic Materials*, Tampa, Florida (USA), 2008, pp. 07F127-3.

[12] X. G. Luo and T. A. Lipo, "A synchronous/permanent magnet hybrid AC machine," *Energy Conversion, IEEE Transaction on,* vol. 15, pp. 203-210, 2000.

[13] D. Fodorean, A. Djerdir, I. A. Viorel, and A. Miraoui, "A double excited synchronous machine for direct drive application-design and prototype tests," *Energy Conversion, IEEE Transaction on,* vol. 22, pp. 656-665, 2007.

[14] T. Finken and K. Hameyer, "Study of hybrid excited synchronous alternators for automotive applications using coupled FE and circuit simulations," *Magnetics, IEEE Transactions on,* vol. 44, pp. 1598-1601, 2008.

[15] J. Farooq, S. Srairi, A. Djerdir, and A. Miraoui, "Use of permeance network method in the demagnetization phenomenon modeling in a permanent magnet motor," *Magnetics, IEEE Transactions on,* vol. 42, pp. 1295-1298, 2006.

[16] Y. Zhilichev, "Analysis of permanent magnet demagnetization accounting for minor *B-H* curves," *Magnetics, IEEE Transactions on,* vol. 44, pp. 4285-4288, 2008.

[17] S. Ruoho, E. Dlala, and A. Arkkio, "Comparison of demagnetization models for finite-element analysis of permanent-magnet synchronous machines," *Magnetics, IEEE Transactions on,* vol. 43, pp. 3964-3968, 2007.

[18] S. Ruoho and A. Arkkio, "Partial demagnetization of permanent magnets in electrical machines caused by an inclined Field," *Magnetics, IEEE Transactions on,* vol. 44, pp. 1773-1778, 2008.

[19] L. Y. Xu, L. R. Ye, L. Zhen, and A. El-Antably, "A new design concept of permanent magnet machine for flux weakening operation," *Industry Applications, IEEE Transactions on,* vol. 31, pp. 373-378, 1995.

[20] M. Aydin, S. Huang, and T. A. Lipo, "Axial flux permanent magnet disc machines: a review," in *Symposium on Power Electronics, Electrical Drives, Automation, and Motion (SPEEDAM)* Capri, Italy, 2004.

[21] M. Aydin, H. Surong, and T. A. Lipo, "A new axial flux surface mounted permanent magnet machine capable of field control," in *Industry Applications Conference, 2002. 37th IAS Annual Meeting.* vol.2, pp. 1250-1257.

[22] T. H. Yang, "Electric machinery with a conduction winding excited magnetic poles warps PM magnetic pole US20090152956 ", 2009.

[23] T. H. Yang, "Electric machinery with a conduction winding excited magnetic poles sandwiched PM magnetic pole US20090121557", 2009.

[24] P. Campbell, *Permanent magnet materials and their application*: Cambridge [England];New York: Cambridge University Press, 1994.

[25] K. Gyu-Hong, H. Jin, N. Hyuk, H. Jung-Pyo, and K. Gyu-Tak, "Analysis of irreversible magnet demagnetization in line-start motors based on the finite-element method," *Magnetics, IEEE Transactions on*, vol. 39, pp. 1488-1491, 2003.

[26] T. H. Kim, "Effect of magnetization direction on irreversible magnet demagnetization in brushless dc motor," in *Proceedings of the 52nd Annual Conference on Magnetism and Magnetic Materials*, Tampa, Florida (USA), 2008, pp. 07F102-3.

[27] K. Ki-Chan, L. Seung-Bin, K. Dae-Hyun, and L. Ju, "The shape design of permanent magnet for permanent magnet synchronous motor considering partial demagnetization," *Magnetics, IEEE Transactions on*, vol. 42, pp. 3485-3487, 2006.

[28] H. Kikuchi, M. Harada, K. Ara, Y. Kamada, S. Kobayashi, and S. Takahashi, "Development of apparatus for magnetic measurements of Charpy impact test pieces," *Journal of Materials Processing Technology*, vol. 181, pp. 190-193, 2007.

[29] "Magnetic Component Engineering," http://www.mceproducts.com/home/about/?id=5.

[30] D. C. Hanselmann, *Brushless Permanent Magnet Motor Design* Second ed.: New York: McGraw-Hill, 2003.

[31] V. Ostovic, *Computer-aided Analysis of Electric Machines*: New York: Prentice Hall, 1994.

[32] S. Vaez-Zadeh and A. H. Isfahani, "Enhanced modeling of linear permanent-magnet synchronous motors," *Magnetics, IEEE Transactions on*, vol. 43, pp. 33-39, 2007.

[33] E. S. Obe, "Direct computation of ac machine inductances based on winding function theory," *Energy Conversion and Management*, vol. 50, pp. 539-542, 2009.

[34] E. Nipp, "Permanent Magnet Motor Drives with Switched Stator Windings," *Ph.D. Thesis, Royal Institute of Technology*, 1999.

[35] F. Magnussen, "On Design and Analysis of Synchronous Permanent Magnet Machines for Field-weakening Operation in Hybrid Electric Vehicles," *Ph.D. Thesis, Royal Institute of Technology*, 2004.

[36] Y. P. Yang and D. S. Chuang, "Optimal design and control of a wheel motor for electric passenger cars," *IEEE Transactions on Magnetics*, vol. 43, pp. 51-61, 2007.

[37] C. T. Tseng, W. C. Liao, and T. C. Tang, "MOST User's Manual," *in Mechanical Engineering Hsinchu: National Chiao-Tung University,* 1993.

[38] Y. P. Yang and C. C. Tu, "Multiobjective optimization of hard disk suspension assemblies. I. Structure design and sensitivity analysis," in *American Control Conference*. vol. 59, 1996, pp. 757-770.

[39] Y. P. Yang and T. C. Chiao, "Multiobjective optimal design of a high speed brushless DC motor," *Electric Machines and Power Systems,* vol. 28, pp. 13-30, Jan 2000.

[40] A. Charnes and W. W. Cooper, "Management Models and Industrial Applications of Linear Programming," New York: John Wiley and Sons, 1961.

[41] M. Zeleny, "Multi Criteria Decision Making," New York: McGraw Hill, 1982.

[42] P. Turnbull, J. Kuo, R. Schultz, and B. Turner, "Thermal analysis of an electric machine for a hybrid vehicle," *SAE International,* Mar 2004.

[43] "TMC TECHNOLOGY CORP. - Taoyuan Factory," Address:No.726, Sec.2, Jieshou Rd., Bade City, Taoyuan 33447, Taiwan, R.O.C.: TEL:886-3-368-8127, FAX:886-3-368-8782, http://www.tmcint.com/

[44] "DSP6001 Dynamometer Controller," http://www.magtrol.com/motortesting/photos/dsp6001.jpg.

[45] "6530 Power Analyzer," http://www.magtrol.com/motortesting/photos/6530.jpg.

[46] G. R. Slemon, "Achieving a constant power speed range for PM drives," *IEEE Transactions on Industry Applications,* vol. 31, pp. 368-372, 1995.

Appendix A

motorparameter.m

```
clear
V_d = 48; % driving voltage
ia = 10; % armature current
i_f = 10; % field current
o = 0.65 * 0.001; % slot opening
g = 0.5 * 0.001; % air gap length
w_b1 = 0.8 * 0.001; % front permeable material width
w_b2 = 2 * 0.001; % lateral permeable material width
l_b = 5 * 0.001; % front permeable material length
wss = 20*0.001; % half of the stator slot width
R_a = 50 * 0.001; % armature outer radius
L = 100 * 0.001; % motor length
l=L; % motor length
tau_m = 50 * 0.001; % magnet width
l_m = 4 * 0.001; % magnet length
N = 64; % number of turns per armature slot
N_s = 20; % number of slots
N_m = 4; % number of poles
N_s_min = 10; % number of slots in magnet circuit model
N_m_min = 2; % number of poles in magnet circuit model
omega = 3000; % motor speed
B_r = 1.065; % remanence of magnet
H_c = 12800; % coercive force of magnet
Nf = 30; % number of turns per field slot
N_i_f = Nf*i_f; % MMF per field slot
mu_0 = 4*pi*10^-7; % permeability coefficient of air gap
mu_rm = 1.1; % relative permeability of magnet
mu_r = 5000; % relative permeability of permeable material
tau_s = 2 * pi * R_a / N_s; % slot pitch
tau_p = 2 * pi * R_a / N_m; % pole pitch
w_t = tau_s - o; % tooth top width
tau_f = tau_p - tau_m - 2 * l_b; % magnet slot width
np = N_m * N_s * 5; % divided into np point
lp = N_s_min * tau_s / np; % arc length of each point
```

permeance.m

```
motorparameter % load file
% calculation of effective air gap
u = (o/(2*g))+sqrt(1+(o/(2*g))^2);
beta = (1-u)^2/(2*(1+u^2));
gamma = (4/pi)*((o/(2*g))*atan(o/(2*g))-log(sqrt(1+(o/(2*g))^2)));
o_prime = (gamma/beta)*g;
x = 0:lp:o_prime;
g_eff = g./(1-beta.*(1-cos(2.*pi.*x./o_prime)));
w_t_eff = tau_s-o_prime;
N_w_t_eff = round(w_t_eff/lp);
N_g_eff = length(g_eff);
N_tau_s = N_w_t_eff+N_g_eff;
N_up = round(N_g_eff/2);
N_down = (N_g_eff-N_up);
l_temp(1:N_down) = g_eff(N_up+1:N_g_eff);
l_temp(N_down+1:N_down+N_w_t_eff) = g;
l_temp(N_down+N_w_t_eff+1:N_tau_s) = g_eff(1:N_up);
l_g_eff=repmat(l_temp,1,N_s_min);
N_tau_m = round(tau_m/lp);
N_tau_p = round(length(l_g_eff)/(N_m_min));
N_tau_f = N_tau_p-N_tau_m;
% calculation of permeance
P_mm=(mu_0*l*log(1+pi*(g/2*wss)))/pi;
Phi_r=B_r*l*tau_m;
P_m=mu_0*mu_rm*tau_m*l/l_m;
Pb_1=mu_0*mu_r*tau_m*l/w_b1;
Pb_2=mu_0*mu_r*w_b2*l/l_b;
P_eq=2*Pb_2+2+P_m;
gap_mat(1,:)=l_g_eff;
for i=1:(N_m_min-1)
    gap_mat(2,(i-1)*N_tau_p+1:(i-1)*N_tau_p+N_tau_m)=(-1)^(i+1);
    gap_mat(2,(i-1)*N_tau_p+N_tau_m+1:i*N_tau_p)=0;
end
i=i+1;
gap_mat(2,(i-1)*N_tau_p+1:(i-1)*N_tau_p+N_tau_m)=(-1)^(i+1);
gap_mat(2,(i-1)*N_tau_p+N_tau_m+1:length(l_g_eff))=0;
```

```
% calculation of overlapping area
for i=1:N_s_min
    air_g(i,(i-1)*N_tau_s+1:i*N_tau_s)=1;
end
N_gap_mat=length(gap_mat);
for j=1:N_s_min
    for i=1:(N_m_min-1)
         P_g(i+(j-1)*N_m_min,1)=sum(mu_0*(l*abs(gap_mat(2,(i-1)*N_tau_p+1:i*
         N_tau_p)).*air_g(j,(i-1)*N_tau_p+1:i*N_tau_p))./(gap_mat(1,(i-1)*N_tau_p
         +1:i*N_tau_p)))*lp;
    end
    i=i+1;
     P_g(i+(j-1)*N_m_min,1)=sum(mu_0*(l*abs(gap_mat(2,(i-1)*N_tau_p+1:N_gap
     _mat)).*air_g(j,(i-1)*N_tau_p+1:N_gap_mat))./(gap_mat(1,(i-1)*N_tau_p+1:N_
     gap_mat)))*lp;
end
for Ns=1:(N_gap_mat-1)
    gap_move(1:N_gap_mat-Ns)=gap_mat(1,Ns+1:N_gap_mat);
    gap_move(N_gap_mat-Ns+1:N_gap_mat)=gap_mat(1,1:Ns);
    for j=1:N_s_min
        air_g_move(j,1:N_gap_mat-Ns)=air_g(j,Ns+1:N_gap_mat);
        air_g_move(j,N_gap_mat-Ns+1:N_gap_mat)=air_g(j,1:Ns);
        for i=1:N_m_min-1
              P_g(i+(j-1)*N_m_min,Ns+1)=sum(mu_0*(l*abs(gap_mat(2,(i-1)*N_ta
              u_p+1:i*N_tau_p)).*air_g_move(j,(i-1)*N_tau_p+1:i*N_tau_p))./(gap_
              move(1,(i-1)*N_tau_p+1:i*N_tau_p)))*lp;
        end
        i=i+1;
          P_g(i+(j-1)*N_m_min,Ns+1)=sum(mu_0*(l*abs(gap_mat(2,(i-1)*N_tau_p
          +1:N_gap_mat)).*air_g_move(j,(i-1)*N_tau_p+1:N_gap_mat))./(gap_move
          (1,(i-1)*N_tau_p+1:N_gap_mat)))*lp;
    end
end
```

flux.m

```
clear
permeance % load file
for i=1:N_s_min
    P_g1_temp(i,:)=P_g(1+(i-1)*N_m_min,:);
    P_g2_temp(i,:)=P_g(2+(i-1)*N_m_min,:);
end
for j=1:Ns
    P_g1(j)=sum(P_g1_temp(:,j));
    P_g2(j)=sum(P_g2_temp(:,j));
end
% calculation of permeance matrix
for i=1:Ns
    A(1,:)=[-2*P_eq P_eq P_eq 0 0 0 0];
    A(2,:)=[P_eq -(Pb_1+P_eq) 0 P_eq 0 0 0];
    A(3,:)=[P_eq 0 -(Pb_1+P_eq) 0 Pb_1 0 0];
    A(4,:)=[0 Pb_1 0 -Pb_1 0 -(P_g1(i)+P_mm) P_mm];
    A(5,:)=[0 0 Pb_1 0 -Pb_1 P_mm -(P_mm+P_g2(i))];
    A(6,:)=[0 0 0 -1 0 1 0];
    A(7,:)=[0 0 0 0 1 0 -1];
    B(:,1)=[0 -Phi_r Phi_r 0 0 N_i_f N_i_f];
    V=inv(A)*B;
    Phi_g(1,i)=V(6)*P_g(1,i)+V(7)*P_g(2,i);
    Phi_g(2,i)=V(6)*P_g(3,i)+V(7)*P_g(4,i);
    Phi_g(3,i)=V(6)*P_g(5,i)+V(7)*P_g(6,i);
    Phi_g(4,i)=V(6)*P_g(7,i)+V(7)*P_g(8,i);
    Phi_g(5,i)=V(6)*P_g(9,i)+V(7)*P_g(10,i);
    Phi_g(6,i)=V(6)*P_g(11,i)+V(7)*P_g(12,i);
    Phi_g(7,i)=V(6)*P_g(13,i)+V(7)*P_g(14,i);
    Phi_g(8,i)=V(6)*P_g(15,i)+V(7)*P_g(16,i);
    Phi_g(9,i)=V(6)*P_g(17,i)+V(7)*P_g(18,i);
    Phi_g(10,i)=V(6)*P_g(19,i)+V(7)*P_g(20,i);
    clear V
end
% calculation of flux
for i=1:N_s_min
    subplot(N_s_min,1,i)
    plot(0:1/0.999:(Ns-1)/0.999,Phi_g(i,:),'LineWidth',2)
```

```
    ylabel(num2str(i))
    Axis=axis;
    axis([0 360 -0.002 0.002])
    set(gca,'xtick',[0 90 180 270 360],'ytick',[ ])
    if i==1
        title('Flux to Rotor Shift Diagram');
    elseif i==N_s_min
        xlabel('Rotor Shift (electrical   degrees)')
    end
end
% calculation of flux difference
for i=1:Ns-1
    dPhi_g(:,i)=Phi_g(:,i+1)-Phi_g(:,i);
    dPhi_g(:,Ns)=Phi_g(:,1)-Phi_g(:,Ns);
    Phi_g_d=dPhi_g./lp;
end
```

torque.m

```
clear
flux % load file
commutator=(N_m/2)*360/N_s; % one commutator perid
w=(omega/60)*(N_m/2); % one electrical perid
T=0:(N_m_min/2)/w/Ns:(N_m_min/2)/w-(N_m_min/2)/w/Ns; % a perid of minimum magnet circuit
% calculation of current
for i=1:N_s_min
    I(i,:)=ia*sin(2*pi*w*T-((i-1)*commutator)*pi/180);
end
% calculation of torque
for i=1:N_s_min
    T_q(i,:)=-N_s_min*N*(I(i,:).*dPhi_g(i,:));
end
Torque(1,:)=sum(T_q(:,1:Ns));
figure
plot(0:Ns-1,Torque,'LineWidth',2)
xlabel('Rotor Shift (electrical  degrees)')
ylabel('Output Touque (N-m)')
axis([0 360 0 0.9])
```

inductance.m

```
motorparameter % load file
% calculation of inductance
u = (o/(2*g))+sqrt(1+(o/(2*g))^2);
beta = (1-u)^2/(2*(1+u^2));
gamma = (4/pi)*((o/(2*g))*atan(o/(2*g))-log(sqrt(1+(o/(2*g))^2)));
o_prime = (gamma/beta)*g;
x = 0:lp/N_s_min:N_s_min*o_prime;
theta = 0:(2*pi/(length(x)-1)):2*pi;
degree = theta*180/pi;
g_eff = g./(1-beta.*(1-cos(2.*pi.*x./o_prime)));
% calculation of armature inductance
for k=1:3
    N_aa(k,:) = (4*N/pi)*(sin((k*pi*x)./tau_s)).^2;
    L_aa(k,:) = mu_0*l*R_a*N_aa(k,:)./g_eff;
end
L_armature = sum(L_aa(1:3,:));
figure
plot(degree,L_armature,'LineWidth',2)
xlabel('Rotor Shift (electrical   degrees)')
ylabel('Inductance (H)')
axis([0 360 0 0.0025])
% calculation of field inductance
for k=1:4
    N_ff(k,:) = (4*Nf/pi)*(sin((k*pi*x)./(tau_p/5))).^2;
    L_ff(k,:) = mu_0*l*R_a*N_ff(k,:)./g_eff;
end
L_field = sum(L_ff(1:4,:));
figure
plot(degree,L_field,'LineWidth',2)
xlabel('Rotor Shift (electrical   degrees)')
ylabel('Inductance (H)')
axis([0 360 0 0.0012])
% calculation of mutual inductance
for k=1:3
    N_af(k,:) = (4*N/pi)*(4*Nf/pi)*(sin((k*pi*x)./tau_p)).*(sin((k*pi*x)./tau_s));
    L_af(k,:) = mu_0*l*R_a*N_af(k,:)./g_eff;
end
```

```
L_mutual = sum(L_af(1:3,:));
figure
plot(degree,L_mutual,'LineWidth',2)
xlabel('Rotor Shift (electrical   degrees)')
ylabel('Inductance (H)')
axis([0 360 -0.03 0.03])
```

Appendix B

```
#include <iostream.h>
#include <stdio.h>
#include <math.h>
#include "parameter.h"

int main(void)
{
        double var[9];

        int i,j,k;


        FILE *inout;


        inout = fopen("dcm.i","r");

        for (i=0; i<9; i++)

        fscanf(inout, "%lf", &var[i]);

        fclose(inout);

       double
             o = var[0] / 1000,             //Slot opening
             l_m = var[1] / 1000,          //Magnet length
             tau_m = var[2] / 1000,       //Magnet width
             R_a = var[3] / 1000,          //Armature outer radius
              g = var[4] / 1000,             //Air gap length
              L = var[5] / 1000,             //Motor axial length
              N_a = var[6],                  //Number of turns per slot
             ia = var[7],                   //Armature current
             d_w = var[8]/1000;          //Winding diameter

       double
           w_tb = double(w_tb_temp) / 1000,
           R_ri = double(R_ri_temp) / 1000,
```

```
    d_a = double(d_a_temp) / 1000,
    d1 = double(d1_temp) / 1000,
    d3 = double(d3_temp) / 1000;

const int
         va = 48,
        N_s = 20,
         N_m = 4,
        N_ph = 1,
        N_u = 2,
        N_s_min = 10,
        N_m_min = 2,
        np = N_s * N_m *15/20 ,          //number of points
         np360 = np / (N_m_min / 2),     //number of points in one electrical degree
         npslot = np / N_s_min;          //number of points per slot

const double
        pi = 3.14159,
        H_c = 890000,
        mu_0 = 4 * pi * pow(10,-7),
         mu_rm = 1.1,
         omega = 3000 / 60 * (2 * pi);

 const double
        R = R_a,
        tau_s = 2 * pi * R / N_s,
         tau_p = 2 * pi * R / N_m,
        w_t = tau_s - o,
        tau_f = tau_p - (tau_m + (2 * tau_m * cos(10 * pi / 180))),
        A_s = (2 * pi * R) * L / N_s;


const double
        lbp = (2 * pi * R) / N_u / np;        //length between point
 //calculation of effective air gap//
double
        p = o / (2 * g),
        u = p + sqrt(1 + pow(p,2)),
         beta = pow((1-u),2) / (2 * (1 + pow(u,2))),
```

```
          gamma = (4 / pi) * (p * atan(p) - log(sqrt(1 + pow(p,2)))),
          o_prime = (gamma / beta) * g;

    double
          x[np],
          g_eff[np],
          x_temp;

    for (i=0; i<np; i++)
          x[i] = (i + 0.5) * lbp;

    for (i=0; i<np; i++)
     {
        x_temp = x[i];
        while (x_temp > tau_s)
            x_temp = x_temp - tau_s;
          if (x_temp >= 0 && x_temp < 0.5 * o_prime)
               g_eff[i] = g / (1 - beta * (1 - cos(2 * pi * (x_temp + 0.5 * o_prime) /
o_prime)));
          else if (x_temp >= 0.5 * o_prime && x_temp <= (tau_s - 0.5 * o_prime))
               g_eff[i] = g;
          else if (x_temp > (tau_s - 0.5 * o_prime) && x_temp < tau_s)
               g_eff[i] = g / (1 - beta * (1 - cos(2 * pi * (x_temp - (tau_s - 0.5 *
o_prime)) / o_prime)));
          else
              cout << "An error occured in counting the " << i << "th g_eff.\n";
     }

    double
        mag_g_eff[np],
        mag_temp;

    for (i=0; i<np; i++)
    {
           mag_g_eff[i] = l_m;
    }
     //calculation of magnet MMF//
    double
```

```
    F_m[np],
    F_m_temp,
    pole_inverse;

for (i=0; i<np; i++)
{
      F_m_temp = x[i];
      pole_inverse = 0;
      while (F_m_temp > tau_p)
      {
          F_m_temp = F_m_temp - tau_p;
          pole_inverse = pole_inverse + 1;
      }
      if (F_m_temp >=0 && F_m_temp < 0.5 * tau_f)
          F_m[i] = 0;
      else if (F_m_temp >= 0.5 * tau_f && F_m_temp <= (tau_p - tau_f))
          F_m[i] = pow(-1,pole_inverse) * H_c * l_m;
      else if (F_m_temp > (tau_p - tau_f) && F_m_temp <= tau_p)
          F_m[i] = 0;
      else
          cout << "An error occured in counting the " << i << "th F_m.\n";
}
 //calculation of magnet leakage//
double mag_leakage = 1.0;

if (tau_f < g)
    mag_leakage = 1 - (g / tau_p);
 //calculation of armature MMF//
double
    commutation = 108,
    I_phase[np360][N_ph],
    mag_g_eff_move_temp,
    F_m_move_temp,
    g_eff_360deg[np][np360],
    F_m_360deg[np][np360],
    g_eff_tot,
    H_tot,
    F_0,
```

```
        B_temp,
        B[np],
        B_360deg[np][np360],
        B_slot[N_s_min],
        Phi[np360][N_s_min];

    for (j=0; j<np360; j++)
    {
        I_phase[j][0] = ia * 1.414 * sin((N_m / 2 * j * lbp / R) - (commutation * 0) * pi / 180);
        I_phase[j][1] = ia* 1.414 * sin((N_m / 2 * j * lbp / R) - (commutation * 1) * pi / 180);
        I_phase[j][2] = ia * 1.414 * sin((N_m / 2 * j * lbp / R) - (commutation * 2) * pi / 180);
        if (j != 0)
        {
            mag_g_eff_move_temp = mag_g_eff[np-1];
            F_m_move_temp = F_m[np - 1];
            for (i=np-1; i>0; i--)
            {
                mag_g_eff[i] = mag_g_eff[i-1];
                F_m[i] = F_m[i-1];
            }
            mag_g_eff[0] = mag_g_eff_move_temp;
            F_m[0] = F_m_move_temp;
        }

        for (i=0; i<np; i++)
        {
            g_eff_360deg[i][j] = g_eff[i] + mag_g_eff[i];
            F_m_360deg[i][j] = F_m[i];
        }
        g_eff_tot = 0;
        H_tot = 0;

        F_0 = 0;


        for (i=0; i<np; i++)
```

```
    {
        g_eff_tot = g_eff_tot + 1 / (g_eff[i] + mag_g_eff[i]);
        H_tot = H_tot + F_m[i] / (g_eff[i] + mag_g_eff[i]);
    }

    F_0 = (-1 / g_eff_tot) * H_tot;


    for (i=0; i<np; i++)
    {
        B[i] = (F_m[i] + F_0) / (g_eff[i] + mag_g_eff[i]) * mu_0;
        B_360deg[i][j] = B[i];
    }

    for (i=1; i<=N_s_min; i++)
    {
        B_temp = 0;
        for (k=(i-1)*npslot; k<i*npslot-1; k++)
            B_temp = B_temp + B[k];
        B_slot[i-1] = B_temp / npslot;
    }

    for (i=0; i<N_s_min; i++)
        Phi[j][i] = B_slot[i] * A_s * mag_leakage;
}
 //calculation of flux difference//
double
    d_Phi[np360][N_s_min],
    E_b[np360][N_s_min],
    E_b_phase[np360][N_ph];

for (i=0; i<N_s_min; i++)
{

    for (j=0; j<np360; j++)
     {
         k = j + 1;
         if (k == np360)
            k = 0;
```

```
                d_Phi[j][i] = Phi[k][i] - Phi[j][i];
                 E_b[j][i] = -1 * (d_Phi[j][i] / (lbp / R)) * N_a * omega;
            }
    }

    for (j=0; j<np360; j++)
    {
       E_b_phase[j][0] = E_b[j][1] + E_b[j][2] + E_b[j][3] + E_b[j][4] + E_b[j][5] - (E_b[j][7] + E_b[j][8] + E_b[j][9] + E_b[j][10] + E_b[j][11]);
       E_b_phase[j][1] = E_b[j][5] + E_b[j][6] + E_b[j][7] + E_b[j][8] + E_b[j][9] - (E_b[j][11] + E_b[j][12] + E_b[j][1] + E_b[j][2] + E_b[j][3]);
       E_b_phase[j][2] = E_b[j][9] + E_b[j][10] + E_b[j][11] + E_b[j][12] + E_b[j][1] - (E_b[j][3] + E_b[j][4] + E_b[j][5] + E_b[j][6] + E_b[j][7]);
    }
     //calculation of torque//
    double
        T_ph[np360][N_ph],
        Torque[np360];

    for (j=0; j<np360; j++)
    {
        for (i=0; i<N_ph; i++)
         T_ph[j][i] = E_b_phase[j][i] * I_phase[j][i] / omega;
        Torque[j] = (T_ph[j][0] + T_ph[j][1] + T_ph[j][2]) * 2 * N_u;
    }

    double
        T_avg,
        Torque_temp = 0;

    for (i=0; i<np360; i++)
    {
        Torque_temp = Torque_temp + Torque[i];
    }

    T_avg = Torque_temp / np360 / N_s_min ;


     //calculation of speed//
```

```
    const double
        ra = 9.41 * pow(10,-1),
        phi_f = 9.2 * pow(10,-3),
        k_m = 0.05,
        keb = 0.67 * pow(10,-4),
        eb = N_a * ia * va * keb,
        phi_m = 5 * pow(10,-2),
        speed = ((va-(ia*ra)-eb)/(phi_f+(k_m*phi_m)));
     //calculation of weight//
    double
        V_m,
        V_ry,
        V_sy,
        V_teeth,
        V_shoe,
        l_w,
        A_w,
        V_w,
        W_stator,
        W_rotor,
        weight;

    const double
        D_mg = 7450,
        D_st = 7640,
        D_cu = 7820,
        D_fe = 7950;

    V_shoe = ((pow((R_a + l_m + g + d1),2) * pi - pow((R_a + l_m + g),2) * pi) - (o * d1) * N_s) * L;
    V_teeth = w_tb * d3 * L * N_s;
    V_sy = (pow((R_a + l_m + g + d1 + d3 + d_a),2) * pi - pow((R_a + l_m + g + d1 + d3),2) * pi) * L;
    l_w = ((R_a + g + d1 + (d3 / 2)) * 2 * pi / N_s * 2 + L * 2) * N_a * N_s;
    A_w = pow((d_w / 2),2) * pi;
    V_w = l_w * A_w;
    W_rotor = (V_shoe + V_teeth + V_sy) * D_st + V_w * D_cu;
    V_m = tau_m * l_m * L * N_m ;
```

```
    V_ry = (pow(R_a,2) * pi - pow(R_ri,2) * pi) * L - V_m;
    W_stator = V_m * D_mg + V_ry * D_fe;
    weight = (W_stator + W_rotor);

//calculation of efficiency//
    double
        l_w_ph,
        R_ph,
        CopperLossPerPoint[np360][N_ph],
        CopperLoss_temp1, CopperLoss_temp2, CopperLoss_temp3,
        CopperLoss_ph[N_ph],
        CopperLoss_tot,
        CoreLoss,
        output_power,
        eff;

    const double
        Rho_cu = 1.574 * pow(10,-8),
        D_CoreLoss = 1.5;
        l_w_ph = l_w / N_ph;
        R_ph = Rho_cu * l_w_ph / A_w;

    for (i=0; i<np360; i++)
    {
        for (j=0; j<N_ph; j++)
         {
             CopperLossPerPoint[i][j] = I_phase[i][j] * I_phase[i][j] * R_ph;
         }
    }
    CopperLoss_temp1 = 0;
    CopperLoss_temp2 = 0;
    CopperLoss_temp3 = 0;

    for (i=0; i<np360; i++)
    {
        CopperLoss_temp1 = CopperLoss_temp1 + CopperLossPerPoint[i][0];
        CopperLoss_temp2 = CopperLoss_temp2 + CopperLossPerPoint[i][1];
        CopperLoss_temp3 = CopperLoss_temp3 + CopperLossPerPoint[i][2];
```

```
    }
    CopperLoss_ph[0] = CopperLoss_temp1 / np360;
    CopperLoss_ph[1] = CopperLoss_temp2 / np360;
    CopperLoss_ph[2] = CopperLoss_temp3 / np360;
    CopperLoss_tot = CopperLoss_ph[0] + CopperLoss_ph[1] + CopperLoss_ph[2];
    CoreLoss = D_CoreLoss * W_rotor;
    output_power = T_avg * omega;
    eff = output_power / (CopperLoss_tot + CoreLoss);
    //Export Objective functions//
    inout = fopen("dcm.o","w");
    fprintf(inout, "%lf\n", -T_avg);
    fprintf(inout, "%lf\n", speed);
    fprintf(inout, "%lf\n", -eff);
    fprintf(inout, "%lf\n", weight);
    fclose(inout);
     return 0;
}
```

Appendix C

Table C.1 Materials of each component

Component	Material
Armature	AISI M19
Armature winding	Copper 0.75 mm dia.
Field winding	Copper 1.5mm dia.
Permanent magnet	Ferrite magnet C3440
Stator	Carbon steel S15C
Permeable material	

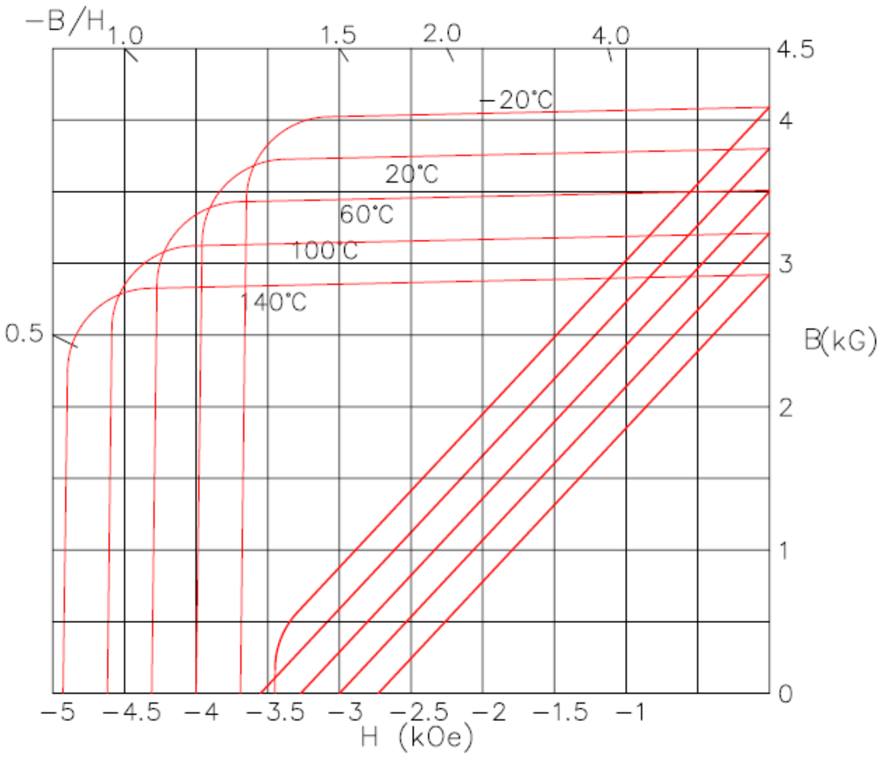

Fig. C.1 The *B-H* curve of ferrite magnet C3440 [29]

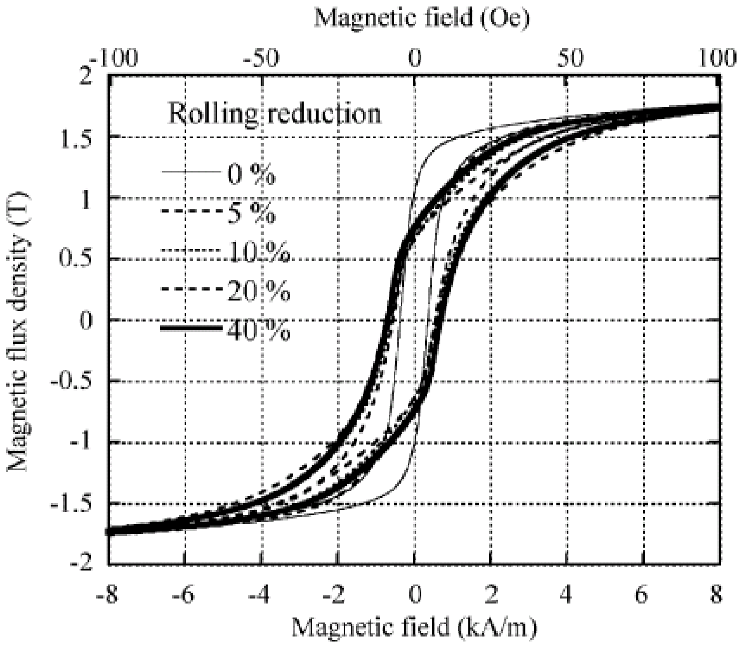

Fig. C.2 The *B-H* curve of carbon steel S15C [28]

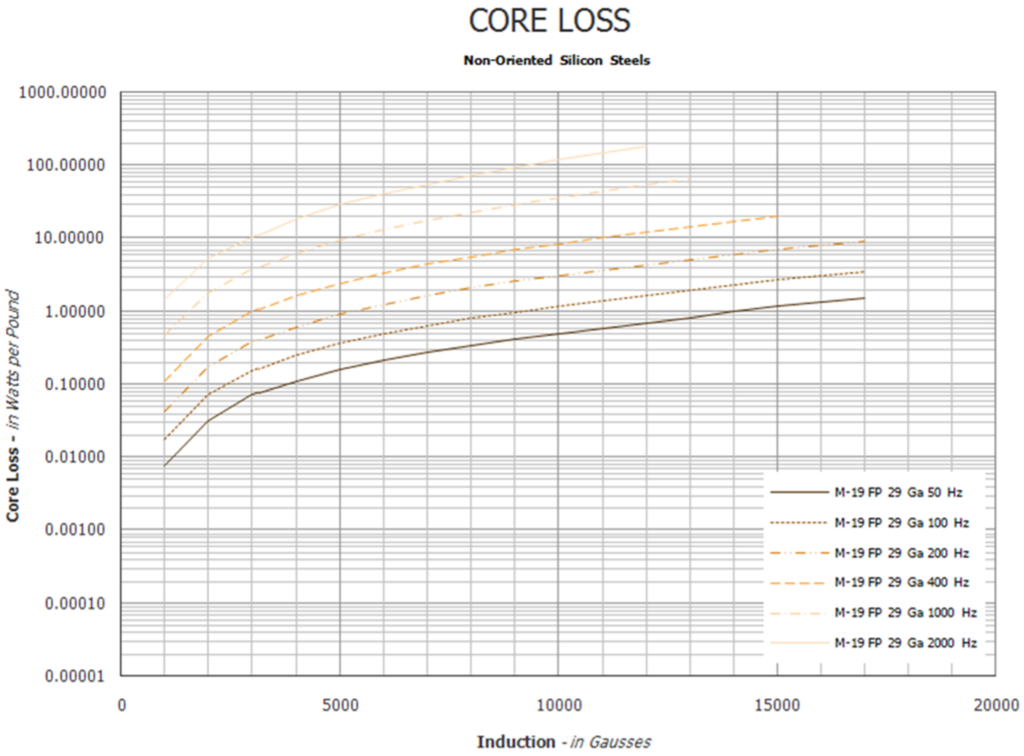

Fig. C.3 AISI M19 core loss chart

Table C.2 American Wire Gauge (AWG)

AWG gauge	Diameter Inches	Diameter mm	Ohms per 1000 ft	Ohms per km	Max. amps
1	0.2893	7.34822	0.1239	0.406392	211
2	0.2576	6.54304	0.1563	0.512664	181
3	0.2294	5.82676	0.197	0.64616	158
4	0.2043	5.18922	0.2485	0.81508	135
5	0.1819	4.62026	0.3133	1.027624	118
6	0.162	4.1148	0.3951	1.295928	101
7	0.1443	3.66522	0.4982	1.634096	89
8	0.1285	3.2639	0.6282	2.060496	73
9	0.1144	2.90576	0.7921	2.598088	64
10	0.1019	2.58826	0.9989	3.276392	55
11	0.0907	2.30378	1.26	4.1328	47
12	0.0808	2.05232	1.588	5.20864	41
13	0.072	1.8288	2.003	6.56984	35
14	0.0641	1.62814	2.525	8.282	32
15	0.0571	1.45034	3.184	10.44352	28
16	0.0508	1.29032	4.016	13.17248	22
17	0.0453	1.15062	5.064	16.60992	19
18	0.0403	1.02362	6.385	20.9428	16
19	0.0359	0.91186	8.051	26.40728	14
20	0.032	0.8128	10.15	33.292	11
21	0.0285	0.7239	12.8	41.984	9
22	0.0254	0.64516	16.14	52.9392	7
23	0.0226	0.57404	20.36	66.7808	4.7
24	0.0201	0.51054	25.67	84.1976	3.5
25	0.0179	0.45466	32.37	106.1736	2.7
26	0.0159	0.40386	40.81	133.8568	2.2
27	0.0142	0.36068	51.47	168.8216	1.7

Appendix D

Table D.1 Motor parameters

Parameter	Value
Armature winding resistance (Ω)	12.66
Field winding resistance (Ω)	0.812
Armature winding inductance (mH)	0.646
Field winding inductance (mH)	0.131
Back EMF constant (mV/rpm)	5.23
Torque constant (N-m/A)	0.045
Rated power (W)	600
Rated voltage (V)	48
Rated current (A)	12.5